Pion Structure from Lattice QCD

Dissertation

zur Erlangung des Doktorgrades
der Naturwissenschaften (Dr. rer. nat.)
der Fakultät für Physisk
der Universität Regensburg

vorgelegt von
Narjes Javadi Motaghi
aus Arak, Iran

im Jahr 2015

Promotionsgesuch eingereicht am: 14.11.2014
Die Arbeit wurde angeleitet von: Prof. Dr. Gunnar Bali

PRÜFUNGSAUSSCHUSS:	Vorsitzender:	Prof. Dr. C. Strunk
	1. Gutachter:	Prof. Dr. G. Bali
	2. Gutachter:	Prof. Dr. V. Braun
	weitere Prüfer:	Prof. Dr. F. Evers

Termin Promotionskolloquium: 12.05.2015

I dedicate this thesis to my beloved parents

Contents

1 Preface **1**

2 Phenomena **7**
2.1 Deep Inelastic Scattering (DIS) . . . 7
2.1.1 Kinematics . . . 8
2.1.2 Parton Model . . . 9
2.1.3 DIS Cross Section . . . 9
2.2 Deeply Virtual Compton Scattering . . . 12
2.2.1 Definition and Properties of GPDs . . . 12
2.3 Moments of GPDs . . . 15
2.4 Generalized Form Factors . . . 16
2.5 Pion Electromagnetic Form factor . . . 18
2.5.1 The pion Charge Radius . . . 18

3 Quantum Chromodynamics on the Lattice **21**
3.1 QCD in the Continuum . . . 21
3.1.1 The Fermion Action . . . 22
3.1.2 The Gauge Field Action . . . 23
3.2 QCD on the Lattice . . . 24
3.2.1 Discretization and Formulation of Lattice Action . . . 24
3.2.2 Lattice Fermion Action . . . 25
3.2.2.1 Gauge Fields on the Lattice . . . 26
3.2.2.2 Lattice Gauge Action . . . 28
3.2.2.3 Fermions on the Lattice . . . 29
3.2.2.4 Wilson Fermions . . . 31
3.2.2.5 Clover–Wilson Fermion . . . 31
3.3 Path Integral . . . 32
3.4 Monte Carlo . . . 33
3.5 Lattice scaling . . . 33

4 Matrix-elements **35**
4.1 Euclidean Correlator . . . 35
4.1.1 Construction of Meson Interpolators . . . 37
4.1.2 Construction of Two-Point Function . . . 39
4.2 Source and Sink Smearing . . . 40
4.2.1 Point Source . . . 40

4.2.2 Overlap Improvement . . . 41
4.2.2.1 Quark Smearing . . . 42
4.2.2.2 Link Smearing . . . 42
4.3 Three-Point Functions . . . 43
4.3.1 Construction of Three-point Function . . . 45
4.3.1.1 Connected Contributions . . . 46
4.3.1.2 Sequential Source Technique . . . 47
4.4 Lattice Operators . . . 48
4.4.1 Renormalization of Operators . . . 49

5 Results for Two-point function **53**
5.1 Two-Point Functions . . . 53
5.1.1 The Calculation of Excited State Energy . . . 54
5.1.2 Effective Mass . . . 55
5.1.3 Smearing . . . 57
5.1.4 Finite Momenta . . . 59
5.1.5 Finite Size Effect . . . 59

6 Pion Parton Distribution Function **63**
6.1 Lattice calculations . . . 63
6.2 Details of the Simulations . . . 64
6.2.1 Excited State Contamination . . . 70
6.3 Forward Limit of GPDs . . . 72
6.3.1 Moments of PDF (Experiments and Modeling) . . . 74
6.3.2 Moments of PDFs (Lattice Results) . . . 75
6.3.3 Finite Size Effect on moments of PDF . . . 75
6.4 Results of PDFs . . . 76

7 Pion Form Factors and Generalized Form Factors **81**
7.1 Form Factor - Experiments and Lattice . . . 81
7.2 Results for Electromagnetic Form Factor . . . 83
7.3 Generalized Form Factor . . . 87

8 Summary **91**

A Notations and conventions **95**
A.1 Parity Transformation . . . 95
A.2 Charge Conjugation . . . 95
A.3 Conventions in Gamma Matrices . . . 96

B Conventions for Our Calculations **97**
B.1 Operators . . . 98
B.2 Pion Electromagnetic Form Factors . . . 98
B.3 Pion Tensor Form Factors . . . 99
B.4 Moments of GPDs . . . 99

C Jackknife Error Estimates **101**

"Physics is a form of insight and as such it's a form of art."

— David Bohm

Chapter 1

Preface

The history of elementary particle physics is around 100 years old. Elementary particle physics was born in 1897 with the discovery of the first elementary particle, the electron, by J.J.Thomson[1]. The electron was and still is considered as an elementary particle which means a point-like particle with no inner structure. In contrast to the electron, atoms have an inner structure which was first shown by Rutherford's gold foil experiment in 1911 [Rut11]. It showed that each atom consists of a nucleus which contains most of the atom's mass and it is surrounded by a cloud of electrons.

Until 1918 the proton was the only other known elementary particle. Later, in the early 30s another particle named neutron was discovered which was slightly heavier than the proton but carried no charge. The nature of the force which keeps the nucleus together was yet missing. Though, it was clear it must be a very strong force, only attractive for protons and neutrons with very short range, and therefore not noticeable in everyday life.

In 1935 a new field was predicted by Hideki Yukawa. He proposed the existence of an exchange particle for the strong force which should have the mass of nearly 300 times that of the electron, but about a sixth lighter than the proton. He called it meson (*middle–weight*) which should be responsible for the exchange of the strong force between protons and neutrons. However, no such particle had been observed in the laboratory before.

At that time a number of cosmic rays studies were in progress, and in 1937 two different groups identified a particle matching Yukawa's description. But the observed cosmic ray particle had a wrong lifetime and interacted very weakly with the atomic nucleus. Moreover, it was significantly lighter than expected from Yukawa's prediction. This puzzle was resolved in 1947 by physicists at Bristol University in England. They discovered the existence of two middle–weight particles in cosmic rays, which are known today as the *pion* π and *muon* μ. The pion was identified as the true Yukawa meson. Simultaneously, the same conclusion on theoretical grounds was reached by Marshak [MB47]. Pions are produced in huge numbers when cosmic rays bombard the earth and collide with atoms in the upper atmosphere. These pions ordinarily decay long before reaching the ground and the Bristol group therefore had to display their photographic emulsions on mountain tops. Later, particle physics experiments showed

[1] We follow the lecture notes of [Fra02] and chapters 1 and 2 [Gri08] and references therein.

the μ does not participate in the strong nuclear interaction and nowadays it classified as a lepton and not a meson.

The existence of pions as charged particles was identified by their double traces on photographic plates. Charged pions decay to a muon and a neutrino (or anti-neutrino)

$$\pi^- \to \mu^- + \bar{\nu}_\mu, \tag{1.0.1}$$
$$\pi^+ \to \mu^+ + \nu_\mu. \tag{1.0.2}$$

The branching ratio[2] says that the probability for the decay $\pi^{+(-)} \to \mu^{+(-)} + \nu_\mu(\bar{\nu}_\mu)$ is larger than that for $\pi^{+(-)} \to \mathrm{e}^{+(-)} + \nu_e(\bar{\nu}_e)$. Besides the charged pions, there is also a chargeless one, the π^0, which does not leave traces in photographic plates. The neutral meson was therefore discovered later in 1950. A π^0 decays as

$$\pi^0 \to e^- + e^+ + \gamma. \tag{1.0.3}$$

The neutral pion has lifetime of about 10^{-16} seconds, whereas the charged ones have longer lifetimes of about 2.6×10^{-8} s. A π^0 is $\pi^0 = 1/\sqrt{2}|u\bar{u} - d\bar{d}\rangle$ and the charged pions are made of a pair of quark anti-quark, each ($\pi^- = |d\bar{u}\rangle$, $\pi^+ = |u\bar{d}\rangle$). The neutral pion is slightly lighter than charged pions, $m_{\pi^\pm} = 139.57$ MeV and $m_{\pi^0} = 134.97$ MeV [B$^+$12, O$^+$14]. The deviation between masses can be due to the electromagnetic self-energy [D$^+$67]. The strong interaction properties of the three pions are identical.

The Nobel Prizes in Physics were awarded to Yukawa in 1949 for his theoretical prediction of the existence of pions, and to Cecil Powell in 1950 for developing and applying the technique of particle detection using photographic emulsions.

Besides pions and muons, many other particles have been discovered in the 40's and 50's by operating the new high energy accelerators, as Willis Lamb humorously pointed out in his Nobel prize acceptance speech: "*When the Nobel prizes were first awarded in 1901, physicists knew something of just two objects which are now called elementary particles: the electron and the proton. A deluge of other elementary particles appeared after 1930; neutron, neutrino, μ meson, π meson, heavier mesons and various hyperons. I have heard it said that the finder of a new elementary particle used to be rewarded by a Nobel Prize, but such a discovery now ought to be punished by a $10,000 fine [Gri08, pn55]*". The *particle zoo* began to fill including elementary particles and also composite ones, like hadrons. However, at that time it was yet unclear which one was elementary and which was not.

A first successful attempt to introduce some structure into the particle zoo was done by Gell-Mann and independently by Zweig in 1964 [GM64, Zwe64]. They introduced that hadrons consist of elementary constituents called *quarks*. In the original quark model, quarks came in three flavors *up*, *down* and *strange*, but later until 1983 other three quarks *charm*, *top* and *bottom* were discovered [Ros81]. Quarks are elementary

[2] There are severals ways for a particle to decay. The probability of its decay to a particular mode is known as its branching ratio for that decay mode.

particles with spin 1/2 and fractional electric charge

flavor			charge
u	c	t	$+\frac{2}{3}e$
d	s	b	$-\frac{1}{3}e$

(1.0.4)

Initially, there had been many doubts on the real existence of quarks as the inner constituents of hadrons. But this was eventually proven by some experiments like deep inelastic scattering (DIS) experiments at the Stanford Linear Accelerator Center (SLAC) in 1968 [B$^+$69].

The quark model was successful in classifying hadrons as bound states of quarks but at the same time another problem appeared: the existence of a hadron consisting of three up quarks with parallel spin Δ^{++} [Bru52]. It showed that quarks have to have a further quantum number, otherwise these states would violate Pauli's exclusion principle. It says that no two particles with half integer spin can occupy the same state. The puzzle was solved by O. W. Greenberg [Gre64]. He proposed that quarks come not only in three flavors but each of them also comes in three color charges commonly named *red*, *green* and *blue*. These color charges have nothing to do with visible colors of light in everyday life. All observed hadrons are colorless.

Nowadays we look at the strong interactions from the point of view of a quantum field theory. The theory describing the strong interactions between the quarks is called *Quantum Chromodynamics*[3] *(QCD)*. It is a non-Abelian gauge theory with the gauge group $SU(3)$ which comes with eight massless vector bosons, called *gluon*s. These gluons are the exchange particles in the strong interaction between quarks and gluons. Since it also features a self-interactions between gluons, it has the very important property of asymptotic freedom.

Asymptotic freedom for non-abelian gauge theories was discovered in 1973 by Wilczek and Gross [GW73b] and independently by Politzer [Pol73], all receiving the Nobel Prize in 2004. For QCD, it implies that at high energies or equivalently short distances, the strong force between quarks becomes zero. This means the coupling constant[4] α_s, tends to be zero and the particles behave as free particles. It indicates that within the hadron, quarks can move without much interacting. Due to this, at high energy region, perturbative treatment of QCD allows us to describe hadronic phenomena.

Conversely, at low energy, the coupling constant increases and it becomes impossible to detach individual quarks and gluons (called partons) from hadrons. This phenomena is called confinement [C$^+$79]. Therefore, at low energy, a perturbative treatment of QCD in an expansion of the coupling constant is not possible. In this regime, hadronic models and effective theories come into play.

One approach to perform non-perturbative QCD calculations is given through *lattice* QCD. The main idea of lattice QCD is to formulate continuum QCD in discretized Euclidean space-time. Lattice QCD can be treated numerically by means of Monte Carlo simulation to estimate path integrals. It is explained in chapter 3.

[3] Since QCD is the theory of color charge, the Greek word "chroma" is applied to its name [Fey85].

[4] The strong coupling constant is a dimensionless number that tells us how strong an interaction is. Analysis of the coupling constant in QCD gives the first order expression of $\alpha_s(E) = \frac{12\pi}{(33-n_f)\ln[E^2/\Lambda^2]}$ with n_f as the number of quark flavors and Λ is a free parameter determined experimentally.

An essential tool to investigate the inner structure of hadrons is the study of (generalized) parton distributions in hadron. In this regard, one can look inside the hadron with good resolution. These probes can be performed by hard experiments like deep inelastic scattering (DIS), semi-inclusive deep inelastic scattering (SIDIS) and deeply virtual Compton scattering (DVCS).

The knowledge of PDFs mostly comes from deep inelastic scattering experiments. By virtue of the factorization theorem[5], the scattering cross section of such a process factorizes into a hard and a soft part.

Th hard part describes the process at short distances (high energy transfer). In this region, the interaction between quarks and gluons are weak, and so this part can be described via perturbation theory. The soft part, in contrast, encodes all information about interaction between quarks and gluons at large distances (low energies) and can not be treated perturbatively. It is the part that is parametrized by hadron structure functions, as for example the PDFs. These structure functions contain all the non-perturbative information about the internal structure of hadron. Along this thesis we are interested in non-perturbative part of process.

In this work, we study moments of parton distribution functions (PDFs) on the lattice. We also look at moments of generalized parton distribution (GPD) [Rad96, Rad97, Ji97, Ji98]. They encode the inner structure of hadrons in terms of the incoming and outgoing quark in the non-perturbative region which are accessible via deeply virtual Compton Scattering (DVCS). GPDs include PDFs and electromagnetic form factor (FF) which can be extracted from electron-proton elastic scattering experiments. Experimentally, measuring GPDs is a big challenge requiring high resolution. Hence, only the very first dedicated experiments have been planned and performed, (e.g. HERMES collaborations [A$^+$01], H1 collaborations [A$^+$05], ZEUS collaborations [C$^+$03] and CLAS collaborations [S$^+$01]). For these, theoretical input for moments of theses PDFs or GPDs are highly welcome.

Outline of this Work

Our goal is to provide theoretical input for pion structure functions from first principles. Pions are the lightest hadrons in the quark model, consisting of a pair of quark and an anti-quark. In chapter 2 we give a brief introduction to DIS and DVCS experiments and present some aspects of parton distribution functions and generalized parton distribution functions. We also mention how to calculate the pion charge radius from electromagnetic form factors. The lattice formulation of QCD is summarized in chapter 3. The tools to calculate observables in lattice QCD using Monte Carlo techniques are explained as well.

In chapter 4 we explain how the expectation values of our observables are computed. These primarily are given through hadronic two- and three-point functions which for the later we use the sequential source techniques. In the final section, we introduce a our regularization scheme which we use to renormalize and convert lattice results into physical numbers.

Chapter 5 is the starting point for our discussion of results for the pion two-point

[5]For a nice explanation look at [Lau14] and [Cou10].

functions. We discuss how to extract the ground state energy and also analyze excited state contributions. In chapter 6 we discuss our data for the second moment of the pion parton distribution functions, in particular, close to the physical quark mass. These have been obtained by performing high-performance computations on Supercomputers. We also evaluate contaminations in our data due to excited states for one ensemble with different values for sink position, t_{sink}. In chapter 7, we analyze the pion electromagnetic form factor and the generalized form factors.

We summarize and conclude in chapter 8 and give points for future studies.

Chapter 2

Phenomena

Between 1967 and 1973 a series of electron-hadron scattering experiments were performed at the Stanford Linear Accelerator Center (SLAC). The findings of those experiments showed that at high energy transfer the hadron is not a fundamental particle but a bound state of point-like constituents, called partons [Fey88]. The distribution of momentum is encoded in the so-called parton distribution functions which can be produced by hard scattering processes like deep inelastic scattering (DIS), deeply virtual Compton scattering (DVCS), and Drell-Yann photo production.

We start this chapter by looking at the kinematics of DIS and DVCS experiments and give a brief introduction to hadron structure functions[1].

2.1 Deep Inelastic Scattering (DIS)

There exists different experiments for the study of hadron structure. These experiments are named with respect to their main focuses. When in a process an initial lepton with very short wavelength probes distances much shorter than the size of the target hadron, it is called *deep* process. When in a scattering process the incident and resultant particles are the same, like Compton scattering (right diagram of Fig. 2.1.1), the process is called *elastic* scattering. While, when the target absorbs some energy and breaks up to many final particles, it is called *inelastic* scattering (left diagram Fig. 2.1.1). So in deep inelastic scattering experiments, a high energy lepton interacts with the target hadron and breaks it to different other final states.

Moreover, if in a scattering process, more than a couple of final states are produced, different instruments are needed to detect the resultant particles. If only the scattered lepton is detected and the rest left unmeasured, it is called *inclusive* DIS. Whereas, when in addition to the scattered lepton, one or two high energy hadrons are detected, it is called *semi-inclusive* one. In the case that all final state particles and their momenta are known, it is called *exclusive* scattering. In the following, we discuss the exclusive DIS experiment and explain how these are used to obtain information about hadron structure functions therefrom.

[1] We follow [BR05] and [BP07], chapters 6 and 8 in [HM84], 2 and 3 in [Bas07], section 2 in [Sch98].

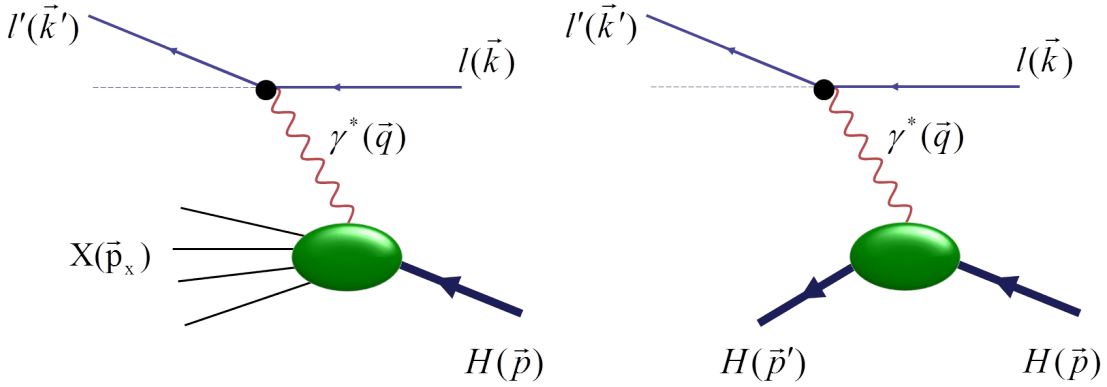

Figure 2.1.1: Left: Basic diagram for deep inelastic lepton-hadron scattering mediated by virtual photon exchange. Right: Elastic scattering, the hadron has exchanged its momentum, unlike the DIS process where hadron has been smashed into other particles.

2.1.1 Kinematics

DIS allows us to investigate the internal structure of hadrons. Most of our knowledge about hadron structures has been derived from lepton-hadron scattering

$$l(k) + H(p) \rightarrow l'(k') + X(p_x). \tag{2.1.1}$$

Here, l labels the initial lepton with 4-momentum k and energy E and l' the outgoing lepton with 4-momentum k' and scattered energy E'. X denotes all the final hadronic states with mass M_X. The kinematic variables describing the DIS process are

- $Q^2 = -q^2 = (k - k')^2 = 4EE' \sin^2(\frac{\theta}{2})$: The squared 4-momentum transfer of the virtual photon.
- θ: Lepton scattering angle.
- $\nu = E - E' = p \cdot q / M_H$: The energy loss of the lepton which can be associated with the energy of the virtual photon γ^*.
- M_H: The mass of target hadron.
- $p = (M, \vec{0})$: The 4-momentum of the fixed target.
- $q = (E - E', \vec{k} - \vec{k}')$: The 4-momentum of the virtual photon.
- $y = \nu / E$: The fractional energy loss of the lepton.
- $x_B = \frac{Q^2}{2M_H \nu} = \frac{Q^2}{2p \cdot q}$: The Bjorken scaling variable.

By increasing Q^2, the spatial resolution increases and the quark structure of the hadron can be seen.

2.1.2 Parton Model

DIS experiment is the key to evaluate parton densities, $q(x)$, and Helicity distributions, $\Delta q(x)$, of hadrons [BP07]. A parton density is the probability of finding a parton with longitudinal momentum fraction x of its parent hadron, regardless of its spin directions. Helicity is the layout of a parton spin parallel or anti-parallel to the direction of the parent momentum. With respect to the positive helicity for parent, the number density of partons with positive helicity minus the negative ones is known as helicity distributions.

The basic idea of the parton model is that at high energy, an initial lepton interacts with one of the partons in the hadron by exchanging a virtual photon. It is shown schematically in Fig. 2.1.2. The structureless feature of partons is symbolized by the point notation in the Figure. To the lowest order, the interacting parton is a quark, since the gluon has no electric charge. All information about the target hadron in inclusive scattering processes are collected in the structure functions. We will see that to leading order at high energy momentum transfer $Q^2 \to \infty$, the hadron structure functions are independent of the dimensional parameter Q^2 but depend on the fixed scaling variable x_B proposed by Bjorken [BP69], which can be obtained from the invariant mass of the hadronic states

$$M_X^2 = (p+q)^2 = M^2 + 2p \cdot q + q^2. \tag{2.1.2}$$

Here, M_X at least must be the same as the mass of the hadron $M_X^2 \geq M^2$. By implementing $q^2 = -Q^2$ in Eq. (2.1.2) we obtain

$$M^2 + 2p \cdot q - Q^2 \geq M^2 \quad \Rightarrow \quad x_B = \frac{Q^2}{2p \cdot q} \leq 1. \tag{2.1.3}$$

It means that the longitudinal momentum fraction x is equal to the Bjorken scaling variable x_B. Since Q^2 and $p \cdot q$ are both positive, it follows that

$$0 \leq x_B \leq 1 \tag{2.1.4}$$

where $x_B = 1$ corresponds to elastic scattering ($M_X^2 = M^2$). Also the lepton energy loss $E - E'$ is between zero (if $E = E'$) and E (if $E' = 0$), so the fractional energy loss of the lepton must be in the interval

$$0 \leq y \leq 1. \tag{2.1.5}$$

2.1.3 DIS Cross Section

Studying the total cross section of a process is the first step towards an understanding the structure of hadrons [Jaf75]. The meaning of a cross section can be illustrated as follows; if an arrow is fired towards a ball, by increasing the radius of the ball the chance of hitting would go up and the cross section area will increase. However, in particle physics it is more complicated than in archery. In an experiment, the target is not a solid ball but a soft one. Moreover, because of different involved interactions,

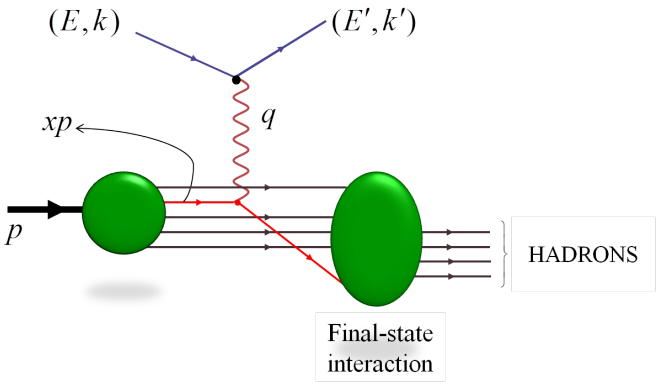

Figure 2.1.2: Kinematics of lepton-hadron scattering in the parton model. The photon interacts with a single quark of the hadron.

the cross section depends on the nature of the fired arrow and the target both. Also, the incident particle can be scattered to different angles. The probability of interaction with particular scattered angle is measured by the differential cross section[2].

The differential cross section for the unpolarized DIS in the laboratory frame can be written as

$$d\sigma = \sum_X \int \frac{d^3k'}{(2\pi)^3 2E'} (2\pi)^4 \delta^4(k + p - k' - Xp) \frac{|\mathcal{M}|^2}{2E\,2M}. \tag{2.1.6}$$

Here, $\mathcal{M}$ is the *scattering amplitude* containing all information about the interaction. The polarization of the final lepton and hadrons have to be summed over. According to the factorization theorem, the spin-averaged $\mathcal{M}$ factorizes into the leptonic tensor also called hard part, $L_{\mu\nu}$, and the hadronic tensor called soft part, $W_{\mu\nu}$, as

$$|\mathcal{M}|^2 \sim L^{\mu\nu} W_{\mu\nu} \tag{2.1.7}$$

where $L_{\mu\nu}$ and $W_{\mu\nu}$ can be calculated perturbatively and non-perturbatively, respectively. The advantage of studying lepton-hadron scattering but not hadron-hadron scattering is that the lepton is a point-like particle. Therefore, the exact expression for $L_{\mu\nu}$ can be written

$$L_{\mu\nu} = \sum_{\text{final states}} \langle k'|J_l^\nu(0)|k, s_l\rangle \langle k, s_l|J_l^\mu(0)|k'\rangle \tag{2.1.8}$$

where J_l is the leptonic current.

The hadronic tensor $W^{\mu\nu}$ (shown in Fig. 2.1.3) contains all information about the hadrons involved in the process. Its calculation is much more complicated. Hadronic tensor can be expressed as the imaginary part of the forward scattering amplitude in deeply virtual Compton scattering

$$W^{\mu\nu} = \frac{1}{2\pi} \text{Im} T^{\mu\nu} \tag{2.1.9}$$

[2]We mostly follow [Gri08, Sch98, Man92] and references therein.

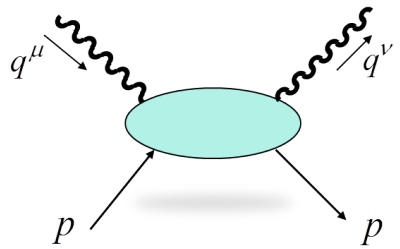

Figure 2.1.3: Hadronic tensor of deep inelastic scattering cross section. It detects the imaginary part of the forward Compton scattering $\gamma^*(q)H(p) \to \gamma^*(q)H(p)$ [BR05].

where

$$T^{\mu\nu} = i \int d^4z\, e^{iq\cdot z} \langle p, \lambda' | \mathcal{T}\{J^\mu(z) J^\nu(0)\} | p, \lambda \rangle. \tag{2.1.10}$$

Here, $\mathcal{T}\{J^\mu(z)J^\nu(0)\}$ is the time-ordered product of the currents $J^\mu(z)$ and $J^\nu(0)$. This relation is known as the optical theorem. So

$$W^{\mu\nu} = \sum_{\lambda,\lambda'} \frac{1}{4\pi} \int d^4z\, e^{iq\cdot z} \langle p, \lambda' | J^\mu(z), J^\nu(0) | p, \lambda \rangle \tag{2.1.11}$$

where $\lambda\,(\lambda')$ is the polarization of the initial (final) hadrons. Fig. 2.1.4 illustrates this relation.

The hadronic tensor $W^{\mu\nu}$ can be written in terms of a spin dependent part which is anti-symmetric and a spin independent one which is symmetric. The polarized lepton and polarized target produce the anti-symmetric leptonic tensor and anti-symmetric hadronic one. The product of these anti-symmetric leptonic and hadronic tensors results in the polarized form factors. In contrast, in unpolarized scattering, one averages over the target polarization and the spin dependent part of $W^{\mu\nu}$ vanishes. Therefore, using an unpolarized lepton beam and an unpolarized hadron target is sufficient to measure unpolarized form factors [Bas07].

The spin independent part of $W^{\mu\nu}$ decompose into two unpolarized structure functions, F_1 and F_2, which depend on two Lorentz invariant quantities

$$W^{\mu\nu} = -F_1(x_B, Q^2)\Big(g^{\mu\nu} - \frac{q^\mu q^\nu}{q^2}\Big) + \frac{F_2(x_B, Q^2)}{p\cdot q}\Big(p^\mu - \frac{p.q}{q^2}q^\mu\Big)\Big(p^\nu - \frac{p.q}{q^2}q^\nu\Big). \tag{2.1.12}$$

Here, $Q^2 = -(p_l - p_{l'})^2 < 0$ is the squared four-momentum transfer by virtual photon. It is known as the scale (resolution) to probe the inner structure of the hadron.

In the Bjorken limit, $Q^2 \to \infty$, structure functions depend only on x_B. These Bjorken scaling functions are related to each other by the Callan-Gross relation [CG69]

$$F_1(x) = \frac{1}{2x} F_2(x) \tag{2.1.13}$$

with

$$F_2(x) = \sum_q e_q^2\, x\, q_q(x) \tag{2.1.14}$$

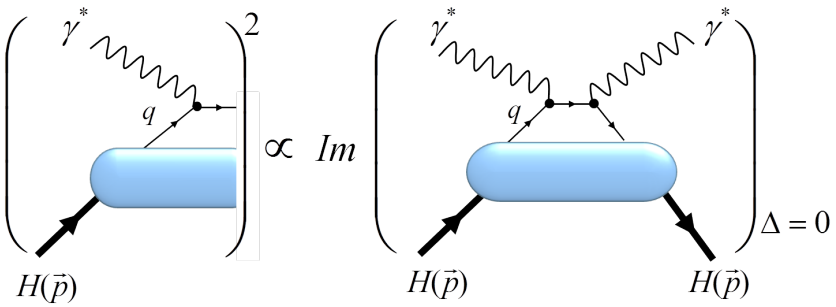

Figure 2.1.4: The optical theorem: the total cross section of the DIS is equal to the imaginary part of the forward Compton scattering. Inspiration for this figure is from [G+13].

where e_q denotes the electric charge of the struck parton. $q(x_B)$ is the probability of finding a parton q with a longitudinal momentum x

$$q(x) = (q_\uparrow + q_\downarrow)(x) + (\bar{q}_\uparrow + \bar{q}_\downarrow)(x) \tag{2.1.15}$$

which is called parton distribution function (PDF). Eq. (2.1.13) is a result of the fact that fermions which are involved partons in DIS are spin 1/2 particles [Pic95].

2.2 Deeply Virtual Compton Scattering

A modern framework to describe the parton structure in hadrons is given by so-called Generalized Parton Distribution functions (GPDs). Experimentally, GPDs can be measured via *Virtual Compton Scattering* which means at least one of the photons involved in the Compton scattering is virtual. VCS amplitude is similar to the hadronic tensor of DIS (see Fig. 2.1.3). Since in the Bjorken limit the momentum transfer is large, in this region virtual Compton scattering is also known as deeply virtual Compton scattering which was proposed by Ji [Ji97] and Radyushkin [Rad96]. DVCS is a hard exclusive process in which the lepton interacts with the hadron via a virtual photon under the emission of another photon. The reaction is represented as

$$l(k) + H(p) \to l'(k') + H(p') + \gamma(q'). \tag{2.2.1}$$

DVCS, schematically is illustrated in Fig. 2.2.1.

2.2.1 Definition and Properties of GPDs

A current can be constructed from combinations of Γ matrices and Dirac fields, $\bar{\psi}\Gamma\psi$. Matrix elements of those currents can be expressed in terms of form factors with covariant normalization $\langle p'|p\rangle = 2p'(2\pi)^3\delta(p'-p)$, where (p^μ) and (p'^μ) are the initial and final momentum, respectively[3].

DIS and DVCS have similar kinematics. DIS involves forward matrix elements of certain operators ($p^\mu = p'^\mu$) which encode the information about parton distribution

[3]For this section we follow [Rad96, Rad97, Die03, BR05, Cou10]

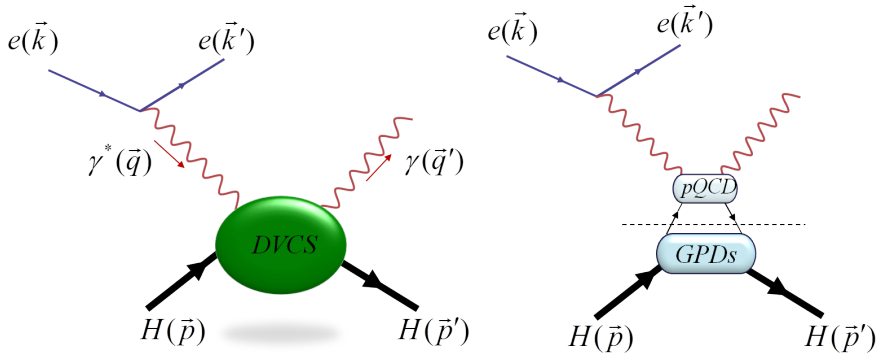

Figure 2.2.1: Left: schematic diagram of DVCS scattering. At least one of two involved photons is virtual. Right: the leading-order handbag diagram. DVCS factorizes into hard parts which is calculable by perturbation theory (pQCD) and the soft parts (GPDs) which can be measured non-perturbatively.

functions (PDFs). DVCS experiments on the other hand include off-forward matrix elements ($p^\mu \neq p'^\mu$) and these matrix elements can be parametrized in terms of generalized parton distributions (GPDs).

PDFs are Q^2-independent but depend on momentum fraction x. However, GPDs are off-forward, so they are functions of Q^2

$$Q^2 = -t = -\Delta^2 = -(p' - p)^2. \tag{2.2.2}$$

Moreover, GPDs require additional variables to describe the initial and final parton states. It is the so-called skewness ξ, which is the longitudinal momentum asymmetry

$$\xi = -\frac{n \cdot \Delta}{2P \cdot n} = \frac{p^+ - p'^+}{p^+ + p'^+}. \tag{2.2.3}$$

Here, n is the light-like four-vector, $n_\pm = (1, 0, 0, \pm 1)/\sqrt{2}$ and $p^+$and p'^+ are used for the pion momenta in light-cone coordinates which is defined by $v^\pm = \frac{1}{\sqrt{2}}(v^0 \pm v^3) = v n_\mp$[4]. Schematics of DIS, DVCS and elastic scattering are illustrated in Fig. 2.2.2. Regarding ξ, one can split momentum fraction x into the three different regions [Die03]:

- $x \in [-1, -\xi]$, both partons have negative momenta $-(x - \xi)$ and $-(x + \xi)$, and this corresponds to the emission and absorption of anti-quarks.
- $-\xi < x < \xi$, one parton has positive momentum while the other one has negative. It corresponds to the emission of a quark and an anti-quark. In this area GPDs behave like meson distribution amplitudes of finding quark and anti-quark pair. However, this kind of information is relatively unknown and can not be accessed in DIS.
- $x \in [\xi, 1]$, both partons have positive momenta $(x - \xi)$ and $(x + \xi)$, which corresponds to the emission of a quark and then absorption of a quark.

[4]For the comprehensive explanation look at [Col97].

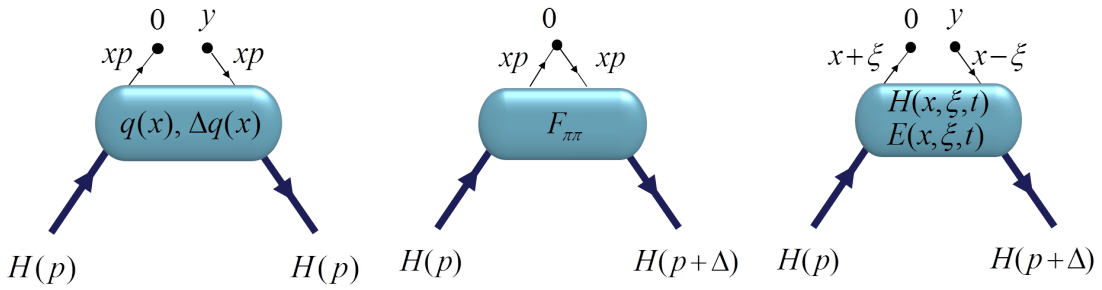

Figure 2.2.2: Left: non-local forward matrix elements $\langle p|\bar{\psi}_q(0)\Gamma\psi_q(y)|p\rangle$ accessed in DIS. Middle: local off-forward matrix elements $\langle p'|\bar{\psi}_q(0)\Gamma\psi_q(0)|p\rangle$ accessed in elastic lepton-hadron scattering. Right: non-local off-forward matrix element $\langle p'|\bar{\psi}_q(0)\Gamma\psi_q(y)|p\rangle$ accessed in DVCS in the region $-\xi < x < \xi$.

Similarly to DIS experiment, the cross section of a DVCS process can be factorized into a hard part which can be calculated perturbatively and a soft part which is a non-perturbative quantity [JO98]. This decomposition is often called a handbag diagram illustrated in Fig. 2.2.1.

GPDs, representing the soft part of the scattering, are defined through a Fourier transform of matrix elements of quark and gluon operators at a light-like separation. The gluon operators will not be considered in our work. The bilocal quark operators are defined as [Hag10]

$$\mathcal{O}^q_\Gamma(x) = \int_{-\infty}^{+\infty} \frac{dz}{2\pi} e^{ixz\cdot n}\, \bar{q}(-\frac{z}{2}\cdot n)\, \Gamma \mathcal{W}_{[-\frac{z}{2}\cdot n, \frac{z}{2}\cdot n]}\, q(\frac{z}{2}\cdot n) \tag{2.2.4}$$

where x is the momentum fraction of the quark and Γ has the Dirac structures $\Gamma = \gamma^\mu$, $\gamma^\mu\gamma^5$, $i\sigma^{\mu\nu}$ to construct the axial, vector and tensor operators. $\mathcal{W}$ is a Wilson line along a light-like path between two quarks to guaranty the gauge invariance of the matrix elements

$$\mathcal{W} = \mathcal{P}\exp\left(ig\int_{\frac{z}{2}}^{-\frac{z}{2}} dx\, n\cdot A(xn)\right). \tag{2.2.5}$$

Here, $\mathcal{P}$ represent a path ordered integral and $n\cdot A$ indicates the light-cone gauge. The pion GPDs for vector and tensor operators are then described by [Die03]

$$\langle \pi(\vec{p}')|\mathcal{O}^\mu_V(x)|\pi(\vec{p})\rangle = 2\bar{p}^\mu H^\pi(x,\xi,t) + \text{higher twist}, \tag{2.2.6}$$

$$\langle \pi(\vec{p}')|\mathcal{O}^{\mu\nu}_T(x)|\pi(\vec{p})\rangle = \frac{\bar{p}^{[\mu}\Delta^{\nu]}}{m_\pi}\, E^\pi_T(x,\xi,t) + \text{higher twist} \tag{2.2.7}$$

with definition of $A^{[\mu}B^{\nu]} = A^\mu B^\nu - A^\nu B^\mu$. $H^\pi(x,\xi,t)$ and $E^\pi_T(x,\xi,t)$ are unpolarized form factors since it is averaged over the quark helicities.

Forward Limit

The matrix elements in Eq. (2.2.6) and (2.2.7) are off-forward because the momenta of the initial and final hadrons are different. In the forward limit, $p = p'$, hence

$\Delta = p - p' = 0$ and $\xi = 0$. It means the fraction of the longitudinal momentum carried by the struck parton is the Bjorken variable $x \to x_B$. As a result, the generalized parton distributions in the forward limit are reduced to ordinary parton distributions calculated in DIS [BP07]

$$H^\pi(x_B, 0, 0) = \begin{cases} q(x_B), & x_B > 0 \\ -\bar{q}(-x_B), & x_B < 0. \end{cases} \tag{2.2.8}$$

Parton distribution functions (PDFs) are the probability to find a parton with momentum fraction $0 \leq x \leq 1$.

2.3 Moments of GPDs

Eq. (2.1.10) indicated that by means of the optical theorem, deep inelastic structure functions can be determined by the commutator of two non-local currents $J^\mu(z)\ J^\nu(0)$, sandwiched between hadronic states. At short distances, around the light-cone $z^2 \to 0$, the currents product can be expanded into a series of local operators [WZ72]

$$\lim_{z^2 \to 0} \mathcal{O}_i(z)\, \mathcal{O}_j(0) = \sum_k c_{ijk}(z)\, \mathcal{O}_k(0) \tag{2.3.1}$$

where c_{ijk} called Wilson coefficients which depend on the separation z. This is called an *operator product expansion* (OPE). Hence, to compute the matrix elements, the operator product can be replaced by the expansion (2.3.1) where the Wilson coefficients are independent of the matrix elements [GW73a]. The same OPE holds for virtual Compton structure functions as well [MV00].

The matrix elements of operators in the hadronic tensor correspond to the Mellin moments of the structure function. The Mellin n–th moment of a function f is defined as [C+72]

$$M_n = \int_0^1 \mathrm{d}x\, x^{n-1}\, f(x), \qquad n = 1, 2, \ldots. \tag{2.3.2}$$

The inverse of all Mellin moments would give us the function f.

Twist-two Operators

By means of the OPE, instead of the light-cone operators, tower of local operators $\mathcal{O}_n^{\mu_1 \cdots \mu_n}$ which are traceless and symmetric in μ_i are used. In DIS kinematics, $0 < x_B = \frac{Q^2}{2M_H \nu} < 1$ and an operator with dimension d and spin n is of order $\mathcal{O}(x_B^{-n})(M_H/Q^2)^{d-n-2}$. It means an operator being controlled by exponent of $d - n - 2$, where $d - n$ is [GT71]

$$\text{twist} = \text{dimension}\,(d) - \text{spin}\,(n). \tag{2.3.3}$$

The minimal twist ($= 2$) has the main contributions which corresponds to maximal spin. A finite amount of twist-two operators are contributing to the structure functions in the deep inelastic limit. The twist-two operators are written in terms of quark fields ψ, gluon fields $F_{\mu\nu}$ and covariant derivatives D^μ. Their spin, dimension and twists are

	ψ	$F_{\mu\nu}$	D^μ
d	$\frac{3}{2}$	2	1
n	$\frac{1}{2}$	1	1
t	1	1	0

Table 2.3.1: Dimension and twist.

listed in Table 2.3.1. Note that adding derivatives to the operator will not change the twist, because spin and dimension both increase by one and according to Eq. (2.3.3), their contributions in changing twist is zero. The twist-two operators for quark and gluon have different forms. The gluonic operators are not discussed here and the general forms of traceless twist-two operators for quarks are written as (see, e.g., [Sch98])

$$\mathcal{O}_{Mq}^{\{\mu_1\cdots\mu_n\}} = i^{n-1}\bar{\psi}^{(f)}\gamma^{\{\mu_1}\overleftrightarrow{D}^{\mu_2}\ldots\overleftrightarrow{D}^{\mu_n\}}\psi^{(f')}, \tag{2.3.4}$$

$$\mathcal{O}_{M\sigma q}^{[\mu_1\{\nu]\cdots\mu_n\}} = i^{n-1}\bar{\psi}^{(f)}i\sigma^{[\mu_1\{\nu]}\overleftrightarrow{D}^{\mu_2}\ldots\overleftrightarrow{D}^{\mu_n\}}\psi^{(f')} \tag{2.3.5}$$

where $\psi^{(f)}$ denotes a quark field with flavor f, $\overleftrightarrow{D}_\mu = \frac{1}{2}(\overrightarrow{D}_\mu - \overleftarrow{D}_\mu)$ is the symmetrized covariant derivative, $\sigma_{\mu\nu} = i/2[\gamma_\mu, \gamma_\nu]$. The notation $\{\mu_1\mu_2\}$ indicates the symmetrization in μ_1 and μ_2 and $[\mu_1\nu]$ anti-symmetrization in μ_1 and ν. We should note that one at first has to symmetrize and then anti-symmetrize the indices, i.e. for example

$$\begin{aligned}\mathcal{O}^{[\mu_1\{\nu]\mu_2\}} =& \frac{1}{2}(\mathcal{O}^{\{\mu_1\nu\}\mu_2} + \mathcal{O}^{\{\mu_1\mu_2\}\nu}) \\ =& \frac{1}{4}(\mathcal{O}^{\mu_1\nu\mu_2} - \mathcal{O}^{\nu\mu_1\mu_2} + \mathcal{O}^{\mu_1\mu_2\nu} - \mathcal{O}^{\mu_2\mu_1\nu}).\end{aligned} \tag{2.3.6}$$

2.4 Generalized Form Factors

The off-forward pion matrix elements of a local vector operator for the first moment ($n = 1$) reads

$$\langle\pi(\vec{p}')|\bar{\psi}_q(0)\gamma^\mu\psi_q(0)|\pi(\vec{p})\rangle = 2\bar{p}^\mu A^\pi_{1,0}(t). \tag{2.4.1}$$

Here, $A^\pi_{1,0}(t)$ corresponds to the single pion form factor $f_{\pi\pi}(t)$, which counts the number of valence quarks of one flavor inside the pion. Similarly, the off-forward pion matrix element of a local tensor operator for $n = 1$ is parametrized by

$$\langle\pi(\vec{p}')|\bar{\psi}_q(0)i\sigma^{\mu\nu}\psi_q(0)|\pi(\vec{p})\rangle = \frac{\bar{p}^{[\mu}\Delta^{\nu]}}{m_\pi}\, B^\pi_{T\,1,0}(t) \tag{2.4.2}$$

where $B^\pi_{T\,1,0}$ denotes the pion tensor form factors. Both $A^\pi_{1,0}(t)$ and $B^\pi_{T\,1,0}(t)$ are functions of momentum transfer t and independent of ξ [Die03]. Comparing Eq. (2.4.1) and (2.4.2) with (2.2.6) and (2.2.7) respectively gives the following sum rules [Ji97]

$$\int_{-1}^{+1} dx\, H^\pi(x,\xi,t) = A^\pi_{1,0}(t), \tag{2.4.3}$$

$$\int_{-1}^{+1} dx\, E^\pi_T(x,\xi,t) = B^\pi_{T\,1,0}(t). \tag{2.4.4}$$

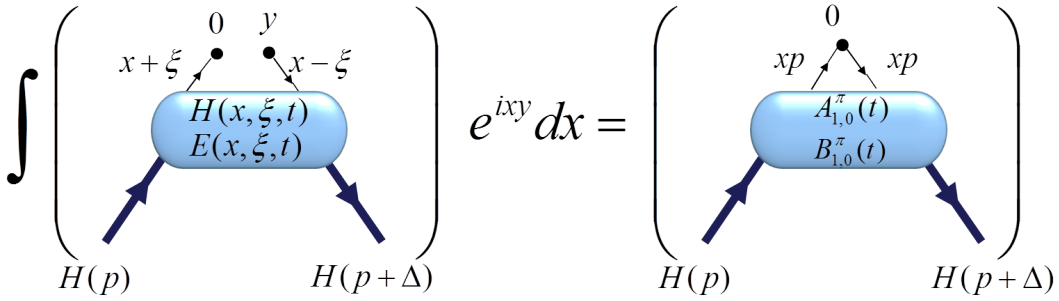

Figure 2.4.1: Sum rules to link the first moment of the GPDs to their GFFs.

Here, the negative x region $-1 < x < 0$ corresponds to an anti-quark distributions. These sum rules are illustrated in Fig. 2.4.1. In order to get the full form factor, we have to sum over all flavors.

The second moment ($n = 2$) of the off-forward pion matrix elements of twist-two vector and tensor operators can be parametrized by generalized form factors (GFFs)

$$\langle \pi(\vec{p}')|\mathcal{O}_V^{\mu\nu}(0)|\pi(\vec{p})\rangle = 2\bar{p}^\mu \bar{p}^\nu A^\pi_{2,0}(t) + 2\Delta^\mu\Delta^\nu C^\pi_{2,0}(t), \tag{2.4.5}$$

$$\langle \pi(\vec{p}')|\mathcal{O}_T^{\mu\nu\rho}(0)|\pi(\vec{p})\rangle = \mathcal{A}_{\mu\nu}\mathcal{S}_{\nu\rho}\frac{\bar{p}^\mu\Delta^\nu}{m_\pi}\ \bar{p}^\rho\ B^\pi_{T\,2,0}(t) \tag{2.4.6}$$

where $A^\pi_{2,0}$, $C^\pi_{2,0}$ and $B^\pi_{T\,2,0}$ represent the pion generalized form factors and $\mathcal{A}$ and $\mathcal{S}$ are functions to anti-smmetrize and symmetrize the indices which were explained in Eq. (2.3.6). The second moments of the pion GPDs are equivalent to GFFs by using Mellin transformation

$$\int_{-1}^{+1} dx\, x\, H^\pi(x,\xi,t) = A^\pi_{2,0}(t) + (-2\xi)^2 C^\pi_{2,0}(t), \tag{2.4.7}$$

$$\int_{-1}^{+1} dx\, x\, E^\pi_T(x,\xi,t) = B^\pi_{T\,2,0}(t). \tag{2.4.8}$$

In the forward limit ($\Delta \to 0$, $\xi \to 0$), $A^\pi_{2,0}(0)$ simplifies to

$$\langle x\rangle^\pi = \int_{-1}^{1} dx\, x\, q^\pi(x) = A^\pi_{2,0}(t=0) \tag{2.4.9}$$

which is interpreted as the momentum fraction carried by partons in the pion.

Now we can write the general form of the matrix elements of the tower of twist-two operators between unequal momentum states. All possible form factors for the vector quark operators arise [Ji98]

$$\langle \pi(\vec{p}')|\mathcal{O}_q^{\{\mu_1\cdots\mu_n\}}|\pi(p)\rangle = \tag{2.4.10}$$

$$2\bar{p}^{\{\mu_1}\bar{p}^{\mu_2}\cdots\bar{p}^{\mu_n\}}A_{n,0}(t) + 2\sum_{\substack{i=0\\ odd}}^{n}\Delta^{\{\mu_1}\Delta^{\mu_2}\cdots\Delta^{\mu_i}P^{\mu_{i+1}}\cdots P^{\mu_n\}}C_{n,i}(t)$$

and for tensor operators

$$\langle\pi(\vec{p}')|\mathcal{O}^{[\mu_1\{\nu]\mu_2\cdots\mu_n\}}_{\sigma q}|\pi(p)\rangle = \frac{1}{m_\pi}\sum_{\substack{i=0\\even}}^{n}\bar{p}^{[\mu_1}\Delta^{\{\nu]}\Delta^{\mu_2}\cdots\Delta^{\mu_i}\bar{p}^{\mu_{i+1}}\cdots\bar{p}^{\mu_n\}}B_{T\,n,i}(t). \tag{2.4.11}$$

Note that for the tensor operator, one has to first symmetrize and then anti-symmetrize [G+99a]. The higher moments of GPDs for twist-two operators are related with GFFs as

$$\int_{-1}^{+1} dx\, x^{n-1}\, H^\pi(x,\xi,t) = A^\pi_{n,0}(t) + \sum_{\substack{i=1\\odd}}^{n}(-2\xi)^{i+1}C^\pi_{n,i+1}(t), \tag{2.4.12}$$

$$\int_{-1}^{+1} dx\, x^{n-1}\, E^\pi(x,\xi,t) = B^\pi_{T\,n,0}(t). \tag{2.4.13}$$

In case that $\xi = 0$, the information from PDFs and form factors are combined and $\mathrm{GPD}(x,0,t)$ can be explained as the probability of finding a quark with longitudinal momentum fraction x at a given transverse distance in the hadron [G+13].

2.5 Pion Electromagnetic Form factor

In elastic processes, soft physics at the long distance are parametrized in terms of form factors. A form factor is a function that gives the information about a certain particles interaction. It is measured experimentally by

$$\frac{d\sigma}{d\Omega} = \left(\frac{d\sigma}{d\Omega}\right)_{\text{point-like}} |f_{\pi\pi}(q^2)|^2 \tag{2.5.1}$$

where $d\Omega$ is the solid angle and $f_{\pi\pi}(q^2)$ denotes the form factor at momentum transfer $q = k' - k$. Since the pion is a spinless particle, the Lorentz decomposition of matrix elements for current J^μ_{em} provides only one electromagnetic form factor (Eq. (2.4.1))

$$\langle\pi(\vec{p}')|J^\mu_{em}(\vec{p}'-\vec{p})|\pi(\vec{p})\rangle = 2\bar{p}^\mu f_{\pi\pi}(t) \qquad \text{with} \quad t \equiv \Delta^2 = (p'-p)^2 \tag{2.5.2}$$

where p and p' are the incoming and outgoing momenta, t is the momentum transfer and $\bar{p}^\mu = (p'+p)/2$. The form factor $f_{\pi\pi}$ describes the charge distribution of a pion, that is the deviation of a pion from being a point-like charge interacting with the electromagnetic field. There have been early measurements of the pion form factors (see, e.g., [B+78, A+86, B+83, H+08b, H+06]).

2.5.1 The pion Charge Radius

We are interested in the cross section for scattering leptons from a point charge to deduce the structure of the target from the form factor. The form factor for a static target can be written as the Fourier transform of the charge distribution [Hof56]

$$f_{\pi\pi}(q^2) = \int \rho(\mathbf{r}')\mathbf{e}^{-\mathbf{i}\mathbf{q}\cdot\mathbf{r}'}\,\mathrm{d}^{\mathbf{3}}\mathbf{r}' \tag{2.5.3}$$

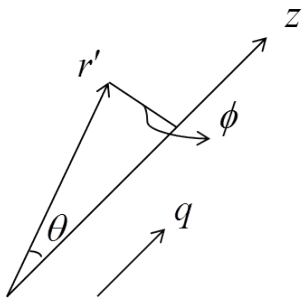

Figure 2.5.1: Spherical coordinates to describe the volume element.

where $\mathrm{d}^3\mathbf{r}'$ is the volume element and $\rho(\mathbf{r}')$ is the charge distribution which is normalized as

$$\int \rho(\mathbf{r}')\,\mathrm{d}^3\mathbf{r}' = \mathbf{1} \tag{2.5.4}$$

where ρ is assumed to be spherically symmetric. Spherical coordinates can be chosen to describe the volume element as shown in Fig. 2.5.1 when q is parallel to z-axis. So, the volume element is driven as $\mathrm{d}^3\mathbf{r}' = r'^2\,\mathrm{d}r'\,\mathrm{d}(\cos\theta)\,\mathrm{d}\phi$. By integrating Eq. (2.5.3) utilized Eq. (2.5.4) one finds

$$f_{\pi\pi}(q^2) = \int\int\int r'^2 \mathrm{d}r'\,\mathrm{d}(\cos\theta)\,\mathrm{d}\phi\,\rho(r')\,e^{-iqr'\cos\theta} \tag{2.5.5}$$

$$= \int_0^{2\pi}\mathrm{d}\phi\int_{r'}\int_{-1}^{1} r'^2\mathrm{d}r'\,\mathrm{d}(\cos\theta)\,\rho(r')\,e^{-iqr'\cos\theta} \tag{2.5.6}$$

$$= \int_{r'} 2\pi[\frac{1}{iqr'}e^{-iqr'\cos\theta}]_{-1}^{1}\,\rho(r')\;r'^2\,\mathrm{d}r'. \tag{2.5.7}$$

With the definition of the sine function with complex arguments we obtain

$$f_{\pi\pi}(q^2) = \int_{r'} 4\pi\frac{\sin(qr')}{qr'}\,\rho(r')\;r'^2\,\mathrm{d}r'. \tag{2.5.8}$$

If the momentum transfer $|\mathbf{q}|$ is not too large, we can Taylor expand $\sin x = x - \frac{x^3}{3!} + \frac{x^5}{5!} + \cdots$ and with Eq. (2.5.4) obtain

$$f_{\pi\pi}(q^2) = 1 + \frac{1}{6}q^2\langle r^2\rangle + \cdots \tag{2.5.9}$$

where $\langle r^2\rangle \equiv \int r'^2\rho(r')\,\mathrm{d}^3r' \equiv 6|\frac{\mathrm{d}f(q^2)}{\mathrm{d}q^2}|_{q^2=0}$ known as a charge radius. By using the normalization condition Eq. (2.5.4), we obtain

$$f_{\pi\pi}(0) \equiv 1. \tag{2.5.10}$$

In the limit $|\mathbf{q}| \to 0$, the exchanged photon has the energy much smaller than the energies of the participating particles in a particular scattering process. However, the wavelength is large enough to resolve only the size of the charge distribution ρ but it is not sensitive to its detailed structures.

Chapter 3

Quantum Chromodynamics on the Lattice

Quantum chromodynamics (QCD) is the theory of the strong force describing the interactions between quarks and gluons. QCD is a quantum field theory with a non-abelian gauge symmetry, given by the group $SU(3)$.

Strong interactions phenomena cover a large range of energies. Their descriptions within the framework of QCD however, requires different techniques. Perturbation theory is perfectly fitted for the high energy range where QCD behaves asymptotically free. At low and intermediate scales, perturbative QCD is not applicable anymore, but there is lattice QCD which enables us to treat many strong interactions phenomena non-perturbatively.

Before giving a brief summary of lattice QCD, we will look at the continuum formulation which will assist us to map the theory onto a four dimensional lattice grid. In continuum calculations, Minkowski space-time is utilized where a space-time point is given by a 4-vector, say x^μ. It is a combination of the three ordinary dimensions of space with $\mu = 1, 2, 3$ for three space directions and a single dimension of time, $\mu = 0$. The explanation of this chapter mainly follows the text books [PS95, Gri08, GL10].

3.1 QCD in the Continuum

The QCD action is defined by the space-time integral over the QCD Lagrange density $\mathcal{L}_{QCD}$

$$\mathcal{S}_{QCD} = \int d^4x \; \mathcal{L}_{QCD} = \mathcal{S}_{ferm} + \mathcal{S}_{gluon}. \tag{3.1.1}$$

It consists of a fermionic[1] part, $\mathcal{S}_{ferm}$ which describes the dynamics of quarks (anti-quarks) and their interactions with the gauge fields and a gluonic[2] part, $\mathcal{S}_{gluon}$ which encodes the dynamics of the gauge fields and their self interactions.

[1] A fermion is a half-integral spin particle and obeying the Pauli exclusion principle.

[2] In particle physics, gluons (or gauge bosons) are the exchange particles for the strong force between quarks.

Quark and anti-quarks are fermions which are represented by a Dirac 4-spinors

$$\psi^f_{\alpha,a}(x), \bar{\psi}^f_{\alpha,a}(x) \tag{3.1.2}$$

at a given space-time position. Here, $\alpha \in [1,2,3,4]$ stands for Dirac index, $a \in [1,2,3]$ color index, i.e. green, red, blue and $f \in [1,\ldots,N_f]$ flavor index. Hence every quark flavor $\psi^f(x)$ comes with 12 independent components.

3.1.1 The Fermion Action

The dynamics of the quarks and gluons is given by the Quantum Chromodynamics Lagrangian. In Euclidean space, the Dirac Lagrangian for a non-interacting quark with flavor f and mass m^f is written as[3]

$$\mathcal{L}_{Dirac} = \bar{\psi}^f(x)(\gamma_\mu \partial_\mu + m^f)\psi^f(x) \tag{3.1.3}$$

where the Euclidean Dirac matrices γ_μ with $\mu = 1,2,3,4$ are defined in Appendix A.3.

We want to have $\mathcal{L}_{Dirac}$ invariant under a symmetry transformation at some space-time points called *local gauge transformation* as

$$\begin{aligned} \psi(x) &\to \psi'(x) = \Lambda(x)\psi(x), \\ \bar{\psi}(x) &\to \bar{\psi}'(x) = \bar{\psi}(x)\Lambda^{-1}(x) \end{aligned} \tag{3.1.4}$$

where $\Lambda \in \mathbb{R}$ is defined as

$$\Lambda(x) = e^{i\theta(x)} = e^{i\omega^a(x)T^a}. \tag{3.1.5}$$

Here, $\omega^a(x) \in \mathbb{R}$ parametrize the group and they are space-dependent. T^a are generators of the $SU(N)$ group (in QCD, $N = 3$, they called *Gell-Mann matrices* which are traceless and Hermitian[4] [Geo99]). The normalization of the generators is fixed by imposing $tr(T^aT^b) = \delta^{ab}/2$. The property of $tr(T^a) = 0$ and $T^a = T^{\dagger a}$ satisfy the commutator relationship

$$[T^a, T^b] = i \sum_{c=1}^{N^2-1} f^{abc} T^c \tag{3.1.6}$$

where f^{abc} are real numbers called *anti-symmetric structure constants*.

But the above Lagrangian, Eq. (3.1.3), is not invariant under this local gauge transformation since we pick up an extra term from the derivative of the $\theta(x)$ in Eq. (3.1.5). To guarantee the local gauge invariance of the Lagrangian, every usual derivative is replaced by the covariant derivative $D_\mu(x)$ as

$$\begin{aligned} D_\mu(x) = \partial_\mu + iA_\mu(x), \quad \text{with} \quad \partial_\mu &= \partial/\partial x^\mu, \\ A_\mu(x) = \sum_{a=1}^{8} A^a_\mu(x) T^a, \quad A^a_\mu(x) &\in \mathbb{R}. \end{aligned} \tag{3.1.7}$$

[3] The Dirac Lagrangian in Minkowski space is $\mathcal{L}_{Dirac} = \bar{\psi}^f(x)(i\gamma^\mu\partial_\mu - m^f)\psi$.

[4] Hermitian operator is an operator coincident with its adjoint.

$A_\mu(x)$ is the four-vector potential. It is necessary to know the transformation for the gauge field in order to preserve the gauge invariance

$$\mathcal{L}[\psi(x), \bar{\psi}(x), A_\mu(x)] = \mathcal{L}[\psi'(x), \bar{\psi}'(x), A'_\mu(x)]. \tag{3.1.8}$$

By inserting Eq. (3.1.4) on the right hand side of Eq. (3.1.8) we obtain

$$\mathcal{L}[\psi(x), \bar{\psi}(x), A_\mu(x)] \stackrel{!}{=} \bar{\psi}(x)\Lambda^{-1}(x)\big(\gamma_\mu(\partial_\mu + iA'_\mu(x)) + m\big)\Lambda(x)\psi(x). \tag{3.1.9}$$

The mass term cancels out and the rest is

$$\begin{aligned}\bar{\psi}(x)\big(\partial_\mu + iA_\mu(x)\big)\psi(x) \stackrel{!}{=}& \\ &\bar{\psi}(x)\Lambda^{-1}(x)\big(\partial_\mu + iA'_\mu(x)\big)\Lambda(x)\psi(x).\end{aligned} \tag{3.1.10}$$

Using the product rule for ∂_μ in the right hand side produces an additional term

$$\begin{aligned}\bar{\psi}(x)\big(\partial_\mu + iA_\mu(x)\big)\psi(x) \stackrel{!}{=}&\bar{\psi}(x)\partial_\mu\psi(x) + \bar{\psi}(x)\Lambda^{-1}(x)(\partial_\mu\Lambda(x))\psi(x) \\ &+ i\bar{\psi}(x)\Lambda^{-1}(x)A'_\mu(x)\Lambda(x)\psi(x).\end{aligned} \tag{3.1.11}$$

It should be denoted that $\Lambda(x)$ commutes with the γ_μ matrices since γ_μ acts in Dirac space but $\Lambda(x)$ acts in color space. Considering $\Lambda^\dagger(x) = \Lambda^{-1}(x)$ and solving for $A'_\mu(x)$ gives us the transformation law for the gauge fields

$$A_\mu \to A'_\mu(x) = \Lambda(x)A_\mu(x)\Lambda^{-1}(x) + i(\partial_\mu\Lambda(x))\Lambda^{-1}(x). \tag{3.1.12}$$

Now we can write the fermionic part of QCD

$$\mathcal{S}_{ferm}[\psi, \bar{\psi}, A] = \sum_{f=1}^{n_f} \int d^4x\, \bar{\psi}^f(x)(\gamma_\mu D_\mu + m^f)\psi^f(x). \tag{3.1.13}$$

3.1.2 The Gauge Field Action

In QCD, gluons mediate the strong interactions of quarks, and they carry color/anti-color charges. They are massless particles, so their Lagrangian contains only the mass term. The field strength tensor $F_{\mu\nu}(x)$ is defined as the commutator of the covariant derivatives

$$\begin{aligned}F_{\mu\nu}(x) &= -i[D_\mu(x), D_\nu(x)] = \partial_\mu A_\nu(x) - \partial_\nu A_\mu(x) + i[A_\mu(x), A_\nu(x)] \\ &= \sum_{a=1}^{8}\Big[\partial_\mu A^a_\nu(x) - \partial_\nu A^a_\mu(x) - f^{abc}A^b_\mu(x)A^c_\nu(x)\Big]T^a \\ &= \sum_{a=1}^{8} F^a_{\mu\nu}(x)T^a.\end{aligned} \tag{3.1.14}$$

Note that in QCD, the commutator $[A_\mu(x), A_\nu(x)]$ does not vanish and in the second line relation (3.1.6) was used. If the field has a local transformation law, its covariant

derivative holds the same law and the commutator of the covariant derivatives as well. Therefore, it is clear that $F_{\mu\nu}(x)$ under the Eq. (3.1.12) transforms as

$$F_{\mu\nu}(x) \to F'_{\mu\nu}(x) = \Lambda(x) F_{\mu\nu} \Lambda^{-1}(x). \tag{3.1.15}$$

Two field strength tensors contract to maintain Lorentz symmetry and take the trace to preserve the gauge symmetry. The gauge action then is given by

$$\mathcal{S}_G(x) = -\frac{1}{2g^2} \int d^4x \ \mathrm{tr}[F_{\mu\nu}(x) F_{\mu\nu}(x)] = -\frac{1}{4g^2} \sum_{a=1}^{8} F^a_{\mu\nu}(x) F^a_{\mu\nu}(x). \tag{3.1.16}$$

3.2 QCD on the Lattice

Lattice gauge theory was introduced by K. Wilson in 1974 [Wil74]. On a hypercubic grid with spacing $a = a_s = a_T$, quark fields are placed on sites and gauge fields on the links between sites. So fermion and gluon fields, derivatives, integrals and so on have to be replaced by discretized expressions. For the lattice QCD, we switch from Minkowski to Euclidean space. This allows us to estimate path integrals by means of Monte Carlo integrations. These simulations are used to calculate correlation functions on the lattice. A D-dimensional Minkowski field theory ($D-1$ spatial dimensions and one time dimension) is connected to a D-dimensional Euclidean field theory by using Wick rotation

$$x^0_M \equiv t \to -i x_4 \equiv -i\tau, \qquad x^j_M \equiv x^E_j \tag{3.2.1}$$

$$p^0_M \equiv E \to i p_4, \qquad p^j_M \equiv p^E_j. \tag{3.2.2}$$

There are different ways in which the QCD action can be discretized and all must give consistent results in the continuum limit. The purpose of this introduction is to provide an outline about the results that are presented in other sections for correlation functions, effective masses and calculation of matrix elements. For a comprehensive explanation of lattice QCD we found the following books [GL10, TC06, L$^+$11, Fle88] and reviews of [Gup97, Het12, Gut12] really helpful.

3.2.1 Discretization and Formulation of Lattice Action

First of all we have to introduce the number of nodes in 4-dimensional space-time

$$x = a \begin{pmatrix} x_1 \\ x_2 \\ x_3 \\ x_4 \end{pmatrix} \text{ with } \quad x_1, x_2, x_3 \in \{0, 1, \cdots, N_L - 1\}, \quad x_4 \in \{0, 1, \cdots, N_T - 1\}. \tag{3.2.3}$$

Here, points in space-time are separated by lattice constant a, $x_{cont} = a x_{lat}$, and quarks are placed at the lattice points

$$\psi(x) = \psi_{a x_{lat}}. \tag{3.2.4}$$

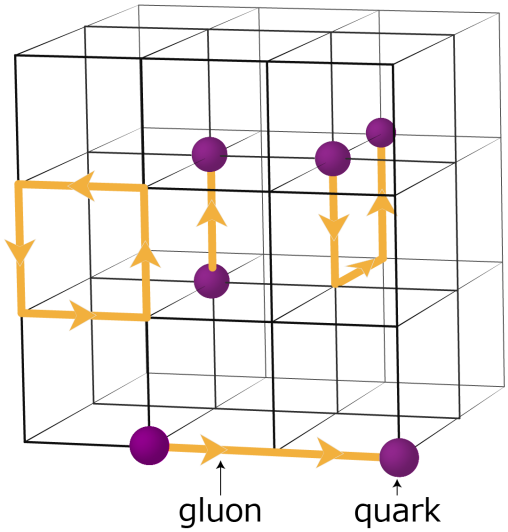

Figure 3.2.1: Schematic diagram of a hypercubic 3-dimensional lattice. Fermion fields sit on the lattice sites and gauge fields on the links between them. Taken from [Cos].

In lattice QCD, we simulate a finite box. In order to maintain translational invariant, boundary conditions are imposed. For fermions, in order to preserve the translation symmetry, all space directions ($\hat{\mu} = 1, 2, 3$) in the lattice theory are set up with periodic boundary conditions [LS11]

$$\begin{aligned} \psi(aL_1 + x_1, x_2, x_3, x_4) &= \psi(x_1, x_2, x_3, x_4), \\ \psi(x_1, aL_2 + x_2, x_3, x_4) &= \psi(x_1, x_2, x_3, x_4), \\ \psi(x_1, x_2, aL_3 + x_3, x_4) &= \psi(x_1, x_2, x_3, x_4). \end{aligned} \tag{3.2.5}$$

For the time direction ($\hat{\mu} = 4$), for reconstruction of Hilbert space from the Euclidean space, the anti-periodic boundary condition is used [GL10]

$$\psi(x_1, x_2, x_3, aL_4 + x_4) = -\psi(x_1, x_2, x_3, x_4). \tag{3.2.6}$$

Whereas, the gluon fields are periodic in all four directions

$$U_{\mu,x+L_j} = U_{\mu,x}, \quad \text{with} \quad j = 1, 2, 3, 4. \tag{3.2.7}$$

Fig. 3.2.1 illustrates the hypercubic lattice in 3 dimensions.

3.2.2 Lattice Fermion Action

When the action is discretized, the fermion field $\psi(x)$ sits only on lattice sites x and the integral over space-time becomes a sum over these lattice points $\int d^4x \to a^4 \sum_x$. Also the derivative is replaced by a discretized one. To derive the discretized derivative, one starts with a Taylor expansion of a function $f(x)$. At the neighboring lattice sites,

$x + a$ and $x - a$, it reads

$$f(x+a) = f(x) + af'(x) + \frac{a^2}{2}f''(x) + \frac{a^3}{6}f'''(x) + \cdots, \tag{3.2.8}$$

$$f(x-a) = f(x) - af'(x) + \frac{a^2}{2}f''(x) - \frac{a^3}{6}f'''(x) + \cdots. \tag{3.2.9}$$

In order to get $f'(x)$, one way is to subtract Eq. (3.2.8) from (3.2.9)

$$f'(x) = \frac{f(x+a) - f(x-a)}{2a} + O(a^2). \tag{3.2.10}$$

Another possible way is solving the linear part of Eq. (3.2.8) for $f'(x)$ and get $f'(x)$ from $f'(x) = \frac{f(x+a)-f(x)}{2a} + O(a)$. But the later expression differs to Eq (3.2.10) in the order of the correction term. Eq (3.2.10) has the correction term of order $O(a^2)$, i.e. the errors are smaller. Therefore, we stick to Eq. (3.2.10) as expression for the derivative. Using the $\hat{\mu}$ direction, it is written as

$$\partial_\mu \psi(x) \to \frac{[\psi(x + a\hat{\mu}) - \psi(x - a\hat{\mu})]}{2a}. \tag{3.2.11}$$

These lead us to the naive fermion action on the lattice

$$S_{ferm}[\psi_x, \bar{\psi}_x] = a^4 \sum_{x \in V} \bar{\psi}_x \Big(\sum_{\mu=1}^{4} \gamma_\mu \frac{\psi_{x+a\hat{\mu}} - \psi_{x-a\hat{\mu}}}{2a} + m\mathbb{1}\psi_x \Big) \tag{3.2.12}$$

where we sum over all lattice sites of volume V. Note that this discretization is of order $O(a^2)$ but it also introduces the famous fermion doubling problem. This will be explained further below.

3.2.2.1 Gauge Fields on the Lattice

An important feature of a lattice formulation of QCD is the preservation of gauge invariance. Above we introduced a gauge field $A_\mu(x)$ to have gauge invariance for fermions in the continuum Lagrangian. On the lattice the invariance under local gauge transformation $SU(3)$ will provide us with the corresponding gauge field. The fermion field on the lattice transforms similar as in the continuum

$$\begin{aligned} \psi_x &\to \Lambda_x \psi_x, \\ \bar{\psi}_x &\to \bar{\psi}_x \Lambda_x^{-1}. \end{aligned} \tag{3.2.13}$$

If the above transformation is applied to the fermion action in the continuum, Eq. (3.1.13), the mass term there stays invariant under this transformation. In contrast, the transformation behavior of the discretized derivative

$$\begin{aligned} \bar{\psi}_x \ \psi_{x+a\hat{\mu}} &\to \bar{\psi}'_x \ \psi'_{x+a\hat{\mu}} \\ &= \bar{\psi}_x \Lambda_x^{-1} \ \Lambda_{x+a\hat{\mu}} \ \psi_{x+a\hat{\mu}} \end{aligned} \tag{3.2.14}$$

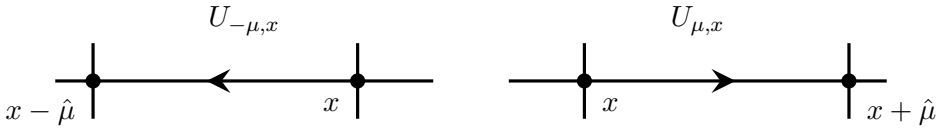

Figure 3.2.2: Link variables. The black dots represent the lattice sites and the arrows indicate the direction of the gauge field (taken from [Gut12]).

is apparently not gauge invariant. In order to maintain gauge invariance the color matrix part has to be removed. Thus, one introduces a new field $U_{\mu,x}$ which under the local gauge transformation transforms as [HH85]

$$U_{\mu,x} \to U'_{\mu,x} = \Lambda_x \; U_{\mu,x} \; \Lambda^{\dagger}_{x+a\hat{\mu}}. \tag{3.2.15}$$

Hence, the gauge transformation matrices Λ cancel in terms like $\bar{\psi}_x U_{\mu,x} \psi_{x+a\hat{\mu}}$ and the expression remains invariant under gauge transformation. The matrix fields $U_{\mu,x}$ live on the links between neighboring lattice sites x and $x + a\hat{\mu}$ (see Fig. 3.2.2), which are called *link variables* or *gauge link*s. $U_{\mu,x}$ denotes the matrix on the link starting from the site x in the direction $\hat{\mu}$ where ($\mu = x$, $\mu = y$, $\mu = z$ or $\mu = t$) and in negative directions $U_{-\mu,x}$, from x to $x - \hat{\mu}$. Link variables in the negative directions are related to those in positive directions by

$$U_{-\mu,x} = U^{\dagger}_{\mu,x-a\hat{\mu}}. \tag{3.2.16}$$

By using these, the discretized naive fermion action is

$$S_{ferm}[\psi_x, \bar{\psi}_x, U] = a^4 \sum_{x \in V} \bar{\psi}_x \Big(\sum_{\mu=1}^{4} \gamma_\mu \frac{U_{\mu,x} \; \psi_{x+a\hat{\mu}} - U_{-\mu,x} \; \psi_{x-a\hat{\mu}}}{2a} + m \mathbb{1} \psi_x \Big). \tag{3.2.17}$$

By implementing Eq. (3.2.13) and (3.2.15) in Eq. (3.2.17), gauge invariance of the fermion action $S_{ferm}[\psi_x, \bar{\psi}_x, U] = S_{ferm}[\psi'_x, \bar{\psi}'_x, U']$, can be seen.

In the continuum, the path-ordered exponential of gauge fields is called *gauge transporter*. It transforms in the same way as the link variables do and connects the points x and y in continuum as

$$G(x, y) = P\exp\Big\{ i \int_x^y A \cdot ds \Big\}. \tag{3.2.18}$$

The gauge transporter transforms as

$$G(x, y) = \Lambda_x G'(x, y) \Lambda^{\dagger}_y. \tag{3.2.19}$$

On the lattice, the shortest path starts at $x = a x_{lat}$ and ends at $y = a(x_{lat} + \hat{\mu})$, and under transformation behaves the same as given in Eq. (3.2.19). Therefore, the link variable $U_{\mu,x}$ is interpreted as a lattice version of the gauge transporter in continuum. To leading order approximation we have

$$U_{\mu,x} = \exp\Big\{ i a A_{\mu,x} \Big\} \tag{3.2.20}$$

where $A_{\mu,x}$ is the lattice gauge field on the link between x and $x+\hat{\mu}$. The path-ordered integral in Eq. (3.2.18) is thus approximated by $aA_{\mu,x}$ along the path from x to $x+a\hat{\mu}$. Negative link variables read

$$U_{-\mu,x} = \exp\Big\{ -iaA_{\mu,x-a\hat{\mu}} \Big\}. \tag{3.2.21}$$

3.2.2.2 Lattice Gauge Action

On the lattice, a path is given by a sequence of lattice points $x_0, x_1, \ldots, x_n$ and can be written as

$$P[U] = U_{\mu_0,x_0}\; U_{\mu_1,x_1} \ldots U_{\mu_{k-1},x_{k-1}} \tag{3.2.22}$$

where k is the number of lattice sites. To check the behavior of the path under the local gauge transformation, we assume a path of two links: $P[U] = U_{\mu_0,x_0}\; U_{\mu_1,x_1}$ where $x_1 = x_0 + a\hat{\mu}$. By applying a gauge transformation, Eq. (3.2.15), we have

$$\begin{aligned} P[U] \to P[U'] &= \Lambda_{x_0} U_{\mu_0,x_0}\; \Lambda^\dagger_{x_0+a\hat{\mu}_0}\; \Lambda_{x_1}\; U_{\mu_1,x_1}\; \Lambda^\dagger_{x_1+a\hat{\mu}_1} \\ &= \Lambda_{x_0} U_{\mu_0,x_0}\; \Lambda^\dagger_{x_0+a\hat{\mu}_0}\; \Lambda_{x_0+a\hat{\mu}}\; U_{\mu_1,x_1}\; \Lambda^\dagger_{x_0+a\hat{\mu}+a\hat{\mu}_1} \\ &= \Lambda_{x_0} U_{\mu_0,x_0}\;\; U_{\mu_1,x_1}\; \Lambda^\dagger_{x_0+a\hat{\mu}+a\hat{\mu}_1} \\ &= \Lambda_{x_0} P[U]\; \Lambda^\dagger_{x_0+a\hat{\mu}+a\hat{\mu}_1}. \end{aligned} \tag{3.2.23}$$

As we can see, only the gauge transformation matrices at the first and the last link remain. Now we switch to the smallest closed loops which are squares of length a, so-called plaquettes. It is illustrated in Fig. 3.2.3. A plaquette $U_{\mu\nu,x}$ is a 1×1 loop product of four links

$$\begin{aligned} U_{\mu\nu,x} &= U_{\mu,x}\, U_{\nu,x+a\hat{\mu}}\, U_{-\mu,x+a\hat{\mu}+a\hat{\nu}}\, U_{-\nu,x+a\hat{\nu}} \\ &= U_{\mu,x}\, U_{\nu,x+a\hat{\mu}}\, U^\dagger_{\mu,x+a\hat{\nu}}\, U^\dagger_{\nu,x} \end{aligned} \tag{3.2.24}$$

where in the second line Eq. (3.2.16) is utilized. This transformation property of the gauge links implies that the trace of the product of gauge links along the closed loop is gauge invariant. In order to get the continuum limit of this plaquette, one uses the Taylor expansion ($A_\nu(x+a\hat{\mu}) = A_\nu(x) + a\hat{\mu}\partial_\mu A_\nu(a) + \mathcal{O}(a^2)$) of Eq. (3.2.20) and (3.2.21) and the Baker-Hausdorff relation ($e^A e^B = e^{A+B+\frac{1}{2}[A,B]+\cdots}$) in Eq. (3.2.24) and obtains

$$\begin{aligned} U_{\mu\nu,x} &\sim e^{iaA_{\mu,x}} e^{ia(A_{\nu,x}+a\partial_\mu A_{\nu,x})} e^{-ia(A_{\mu,x}+a\partial_\nu A_{\mu,x})} e^{-iaA_{\nu,x}} \\ &\sim e^{ia(A_{\mu,x}+A_{\nu,x}+a\partial_\mu A_{\nu,x}+\frac{1}{2}ia[A_\mu,A_\nu])} e^{-ia(A_{\mu,x}+a\partial_\nu A_{\mu,x}+A_{\nu,x}-\frac{1}{2}ia[A_\mu,A_\nu])} \\ &\sim e^{ia^2(\partial_\mu A_{\nu,x}-\partial_\nu A_{\mu,x}+i[A_\mu,A_\nu])} = e^{ia^2 F_{\mu\nu}} \end{aligned} \tag{3.2.25}$$

where in the second line Eq. (3.1.14) is used. The simplest gauge action which is also known as plaquette action proposed by Wilson [Wil74] is given by the product of gauge links around an elementary plaquette

$$\mathcal{S}_g[U] = \beta \sum_x \sum_{1\le\mu<\nu\le 4} \mathrm{tr}\Big(1 - \frac{1}{N}\mathrm{Re}\; U_{\mu\nu,x}\Big). \tag{3.2.26}$$

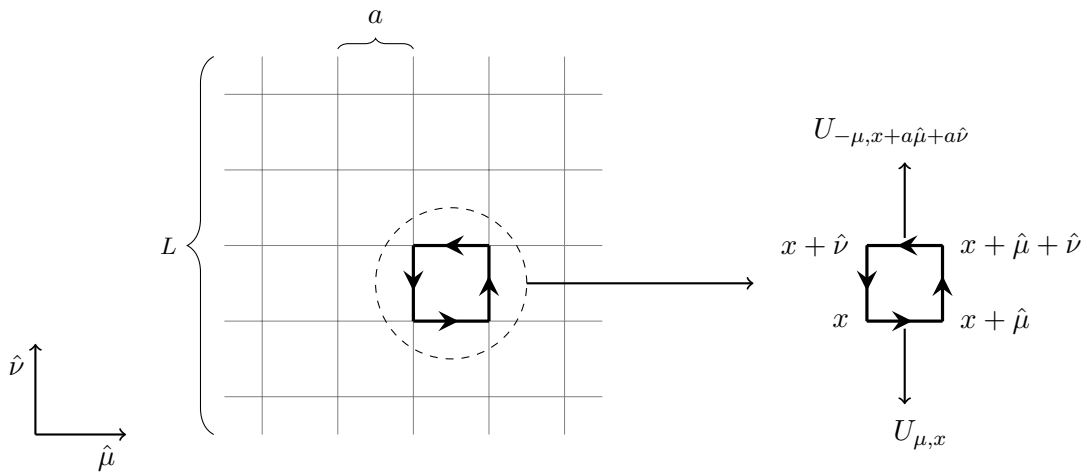

Figure 3.2.3: Plaquette on the lattice in the $\mu - \nu$ plane.

Here, the parameter $\beta = 2N/g^2$ controls the lattice spacing a and is related to the bare strong coupling. The sum is over all possible 1×1 plaquettes and the trace is over color indices. In the limit of small a, we can replace the sum by an integral and use the expansion of $U_{\mu\nu,x} = e^{ia^2 F_{\mu\nu}}$ for small a at leading order. By inserting this expression into the trace of Eq. (3.2.26), one gets in the continuum

$$\frac{1}{4g^2} \int d^4x \, [F^c_{\mu\nu}(x) F^c_{\mu\nu}(x)]. \tag{3.2.27}$$

3.2.2.3 Fermions on the Lattice

The fermion action, Eq. (3.2.17), can be written in the following form[5]

$$S_{ferm}[\psi_x, \bar{\psi}_x, U] = a^4 \sum_x \sum_{\mu=1}^{4} \bar{\psi}(x)_{a\alpha} D(x|y)_{a\alpha,b\beta} \psi(y)_{b\beta} \tag{3.2.28}$$

with the definition of the naive lattice Dirac operator

$$D(x|y)^{\alpha\beta}_{ab} = \sum_{\mu=1}^{4} (\gamma_\mu)_{\alpha\beta} \frac{U_\mu(x)_{ab} \delta_{x+a\hat{\mu},y} - U_{-\mu}(x)_{ab} \delta_{x-a\hat{\mu},y}}{2a} + m\delta_{x,y}\delta_{a,b}\delta_{\alpha,\beta}. \tag{3.2.29}$$

In order to compute correlation functions from which one extracts a hadron mass, the inverse of the Dirac operator is necessary. In case $U_\mu(x) = \mathbb{1}$, fermions are non-interacting and the Fourier transformation[6] of the Dirac operator for two space-time x

[5] Here, we use the notation $\psi(x)$ and $U(x)$ instead of ψ_x and U_x to avoid confusion in the indices.

[6] The Fourier transformation on the lattice is written as $\tilde{f}(p) = \frac{1}{|\Lambda|} \sum_{x\in\Lambda} f(x) e^{-ip\cdot ax}$, $f(x) = \frac{1}{|\Lambda|} \sum_{p\in\tilde{\Lambda}} \tilde{f}(p) e^{ip\cdot ax}$ where $|\Lambda|$ is the volume of the lattice.

and y is written as [GL10]

$$\tilde{D}(p|q) = \frac{1}{|\Lambda|}\sum_{x,y\in\Lambda} e^{-ip\cdot ax} D(x|y) e^{iq\cdot ay} \tag{3.2.30}$$

$$= \frac{1}{|\Lambda|}\sum_{x\in\Lambda} e^{-i(p-q)\cdot ax}\Big(\sum_{\mu=1}^{4}\gamma_\mu \frac{e^{iq_\mu a} - e^{-iq_\mu a}}{2a} + m\mathbb{1}\Big)$$

$$= \delta(p-q)\tilde{D}(p) \tag{3.2.31}$$

Because of the Kronecker-delta, $\tilde{D}(p|q)$ is diagonal. The Fourier transformation of the lattice Dirac operator is defined as

$$\tilde{D}(p) = \frac{i}{a}\sum_{\mu=1}^{4}\gamma_\mu \sin(p_\mu a) + m\mathbb{1} \tag{3.2.32}$$

and its inversion gives

$$\tilde{D}(p_\mu)^{-1} = \frac{m\mathbb{1} - ia^{-1}\sum_\mu \gamma_\mu \sin(p_\mu a)}{m^2 + a^{-2}\sum_\mu \gamma_\mu \sin^2(p_\mu a)}. \tag{3.2.33}$$

Using the Fourier transformation gives us

$$D(x|y)^{-1} = \frac{1}{|\Lambda|}\sum_{p\in\tilde{\Lambda}} \tilde{D}^{-1}(p) e^{ip\cdot a(x-y)} \tag{3.2.34}$$

where $D(x|y)^{-1}$ is the free quark propagator. In case of massless fermions, $m = 0$,

$$\tilde{D}(p_\mu)^{-1}\Big|_{m=0} = \frac{-ia^{-1}\sum_\mu \gamma_\mu \sin(p_\mu a)}{a^{-2}\sum_\mu \gamma_\mu \sin^2(p_\mu a)} \xrightarrow{a\to 0} \frac{-i\sum_\mu \gamma_\mu p_\mu}{p^2}. \tag{3.2.35}$$

Inversions of the Dirac operators are often needed to calculate expectation values. Therefore, we have to compute the Fourier transform of the Dirac operators. With periodic boundary conditions the discrete momenta on the lattice are

$$p_j = 2\pi\frac{n_j}{N_s} \quad for \quad j = 1,2,3 \quad \text{and} \quad p_4 = iE. \tag{3.2.36}$$

Here, the n_j are integers such that the momenta p_j are inside the interval $[-\pi/a, \pi/a]$ known as the Brillouin zone. The lattice dispersion relation can be written as $p^2 \to a^{-2}\sin^2(ap)$ [B+96]. In the continuum, in case of a free massless theory ($m = 0$), the massless propagator has one pole at $p = (0,0,0,0)$ corresponding to a fermion defined by the continuum Dirac operator [Leh54], while a finite lattice spacing gives rise to 15 additional poles at each corner of the Brillouin zone

$$p_j = (\frac{\pi}{a},0,0,0), (0,\frac{\pi}{a},0,0), \cdots, (\frac{\pi}{a},\frac{\pi}{a},\frac{\pi}{a},\frac{\pi}{a}). \tag{3.2.37}$$

These 15 unwanted poles, so-called *doublers* are unphysical lattice artifacts.

3.2.2.4 Wilson Fermions

Again Wilson [Wil75] proposed a solution for the doubling problems with pros and cons. He suggested to add a term $(-\frac{a}{2}\partial_\mu\partial_\mu)$ to the fermion action which gives the doublers the mass $m + \frac{2l}{a}$. In the continuum limit ($a \to 0$), it gives an infinite mass to the doublers. As a result, they decouple and get removed from the action. The Wilson Dirac operator is then

$$D_W(x|y)^{\alpha\beta}_{ab} = (m + \frac{4}{a})\delta_{\alpha\beta}\delta_{ab}\delta_{xy} - \frac{1}{2a}\sum_{\mu=\pm1}^{\pm4}(\mathbb{1} - \gamma_\mu)_{\alpha\beta}U_\mu(x)_{ab}\delta_{x+\hat{\mu},y} \tag{3.2.38}$$

with $\gamma_{-\mu} \equiv -\gamma_\mu$. Then the fermion action reads

$$S_W[\psi,\bar{\psi},U] = \sum_{f=1}^{N_f} a^4 \sum_{x,y\in\Lambda}\sum_{a,b,\alpha,\beta}\bar{\psi}^{(f)}(x)_{a\alpha}D_W(x|y)^{\alpha\beta}_{ab}\psi^{(f)}(y)_{b\beta}. \tag{3.2.39}$$

The disadvantage of this additional term is chiral symmetry breaking. Nielsen-Ninomiya theorem [NN81] summarized that the following conditions can not hold simultaneously: locality of Dirac operators, chiral symmetry and no doublers.

3.2.2.5 Clover–Wilson Fermion

On the lattice, rotational invariance is broken down to a discrete symmetry described by the hypercubic group $H(4)$. For any finite lattice spacing results differ from their continuum limit values, by so-called discretization errors. For Wilson fermions, the discretization errors are of order $\mathcal{O}(a)$. In order to make the errors smaller, we have to decrease the lattice spacing and increase the number of lattice points, which is numerically expensive. The best is to improve the action to reduce the order of the discretization errors from $\mathcal{O}(a)$ to $\mathcal{O}(a^2)$. Symanzik suggested to add local $\mathcal{O}(a)$ correction terms to the action and correlation functions in order to faster converge to the continuum limit [Sym83]. According to Sheikholeslami and Wohlert [SW85], such an improvement for the fermion action can be derived by adding a so-called clover term

$$S_{ferm} = S_W + c_{SW}\frac{i}{4}a^5\sum_x \bar{\psi}(x)\sigma_{\mu\nu}F_{\mu\nu}\psi(x) \tag{3.2.40}$$

where the coefficient c_{SW} can be calculated non-perturbatively and $F_{\mu\nu}$ is the field strength tensor

$$F_{\mu\nu}(x) = -\frac{i}{8a^2}[Q_{\mu\nu}(x) - Q_{\nu\mu}(x)] \tag{3.2.41}$$

with (see [SW85])

$$\begin{aligned} Q_{\mu\nu}(x) &= U_\mu(x)U_\nu(x+a\hat{\mu})U_{-\mu}(x+a\hat{\mu}+a\hat{\nu})U_{-\nu}(x+a\hat{\nu}) \\ &+ U_\mu(x)U_{-\nu}(x+a\hat{\mu})U_{-\mu}(x+a\hat{\mu}-a\hat{\nu})U_\nu(x-a\hat{\nu}) \\ &+ U_{-\mu}(x)U_{-\nu}(x-a\hat{\mu})U_\mu(x-a\hat{\mu}-a\hat{\nu})U_\nu(x-a\hat{\nu}) \\ &+ U_{-\mu}(x)U_\nu(x-a\hat{\mu})U_\mu(x-a\hat{\mu}+a\hat{\nu})U_{-\nu}(x+a\hat{\nu}) \\ &= U_{\mu\nu,x} + U_{\nu-\mu,x} + U_{-\mu-\nu,x} + U_{-\nu\mu,x}. \end{aligned} \tag{3.2.42}$$

This action is what we will use for the fermions in our study.

3.3 Path Integral

To evaluate expectation values of an operator $\mathcal{O}$, on the lattice one uses the so-called *Feynman's path integral*. In this formalism we have to integrate over all degrees of freedom (quarks, anti-quarks and gluons which on the lattice are replaced by the link variables). The expectation value is then

$$\langle \mathcal{O}[\psi, \bar{\psi}, U] \rangle = \frac{1}{Z} \int [d\psi][d\bar{\psi}][dU] \; \mathcal{O}[\psi, \bar{\psi}, U] \; e^{-S_{QCD}} \tag{3.3.1}$$

where

$$[d\psi][d\bar{\psi}][dU] = \prod_{x} \prod_{i=1}^{N} \prod_{\mu=1}^{4} \; d\psi_{x,i} \; d\bar{\psi}_{x,i} \; dU_{\mu,x} \tag{3.3.2}$$

with N the number of fermion fields. In the denominator, the partition function is defined as

$$Z = \int [d\psi][d\bar{\psi}][dU] e^{-S_{QCD}}. \tag{3.3.3}$$

The path integral has to be computed for each field configuration. The fermions obey the Fermi–Dirac statistics[7] and are anti-commuting variables, so-called *Grassmann numbers*[8]. Therefore, one splits the path integral into part containing only gauge links and a part which depends on fermion and the gauge fields

$$\langle O[\psi, \bar{\psi}, U] \rangle = \frac{\int [dU] e^{-S_G[U]} \big(\int [d\psi][d\bar{\psi}] \; \mathcal{O}[\psi, \bar{\psi}, U] \; e^{-S_F[\psi, \bar{\psi}, U]} \big)}{\int [dU] e^{-S_G[U]} \big(\int [d\psi][d\bar{\psi}] \; e^{-S_F[\psi, \bar{\psi}, U]} \big)}. \tag{3.3.4}$$

The fermion part

$$I_f = \int [d\psi][d\bar{\psi}] \mathcal{O}[\psi, \bar{\psi}, U] e^{-S_F[\psi, \bar{\psi}, U]}. \tag{3.3.5}$$

is integrated exactly by using the basic rules for Grassmann integration. It gives

$$I_f = \det \mathrm{D}[U] \, \mathcal{O}[D^{-1}, U]. \tag{3.3.6}$$

The $\det D[U]$ is called the fermion determinant and $\mathcal{O}[D_f^{-1}, U]$ is a function of quark propagators and link variables.

[7] The Fermi–Dirac applies to identical particles with half-integer spin with the condition that no two of these particles can occupy the same state.

[8] Grassmann numbers also called anti-commuting numbers are independent numbers which anti-commute with each other $\theta_i \theta_j = -\theta_j \theta_i$ but commute with ordinary numbers $\theta_i x = x \theta_i$. Also $(\theta_i)^2 = 0$. Their master formulas and derivations can be found in any introduction on Grassmann numbers like [PS95].

3.4 Monte Carlo

Our observables are given by integrals over the gauge fields (see Eq. (3.3.4)). Since the number of integration variables is huge, complete numerical integration is impractical. One feasible way is to use Monte Carlo method. The starting point of any lattice QCD computation is to generate the gauge field configurations [Wei00]. Here, configuration means a set of link variables on the lattice. Once a small subset of gauge field configurations U_i is generated, expectation values $\langle \mathcal{O}[\psi, \bar{\psi}, U] \rangle$ is given by averaging measurements of $\mathcal{O}$ over those configurations. The configurations can be used repeatedly for many different calculations. If the number of configurations, N, is increased, the error decreases as $1/\sqrt{N}$. The most challenging part of the generation of gauge configurations is the need to include the fermion determinant containing the sea quarks.

In pure lattice gauge theory, the full Lagrangian description is not included. It means that the sea quark mass is infinite so all quark loops are neglected. In other words, the fermion determinant is set to $\det(D_f[U]) = 1$. This approach is also named quenched approximation.

Although the quenched approximation works well, it does not account for the influence of dynamical fermions. The inclusion of fermions, namely the fermion determinant in the Monte-Carlo updating process of the gauge links, is numerically expensive but feasible. In dynamical simulations, one usually neglects the contributions of the heaviest quark flavors (b,t) and considers two degenerate light quark flavors, up and down (for $N_f = 2$), and a heavier strange quark (for $N_f = 2 + 1$) and possibly also a charm quark (for $N_f = 2 + 1 + 1$) as well. We will concentrate on the simplest of theses cases, $N_f = 2$, but for rather small (almost physical) quark masses nonetheless.

3.5 Lattice scaling

Since Lattice QCD is performed numerically, all numbers we obtain are naturally dimensionless. To get the correct dimension, a measured quantity in units of the lattice spacing has to be converted to the physical ones. This procedure is called scale setting.

In order to set the scale of the lattice gauge theory, we need to define the physical value for the lattice spacing a. We use a method introduced by Sommer [Som94]. The *Sommer parameter* r_0, is a certain distance related to the shape of the static potentials. The Sommer scale does not directly depend on the potential but on the force between two static quarks

$$F(r) = -\frac{d}{dr}V(r) = \frac{d}{dr}(A + \frac{B}{r} + \sigma r) = -\frac{B}{r^2} + \sigma. \tag{3.5.1}$$

Here, the constant A is an irrelevant normalization of the energy, the second term, B/r is the Coulomb part of the potential with strength B and the last term is a linearly rising term with a constant so-called *string tension* which all can be calculated numerically. The Sommer parameter can be then defined as [Som94]

$$r^2 F(r)|_{r_0} = -B + \sigma r^2|_{r_0} = 1.65 \tag{3.5.2}$$

which corresponds to the physical value $r_0 = \sqrt{(1.65 + B)/\sigma} \approx 0.5\,\text{fm}$.

In the lattice simulations one can determine the dimensionless number r_0/a and express everything in the unit of r_0. A determination of r_0, e.g., over the nucleon mass [B$^+$13] then allows us to to express all quantities in physical units.

Chapter 4

Matrix-elements

In this chapter we summarize lattice techniques for the calculation of matrix elements. In order to understand the details of our analysis described in the next chapters, we will start with two-point functions. We will explain how to get the desired quantum number of the two-point function via appropriate interpolating fields. Afterwards, we explain the smearing method which helps to get a better overlap with physical states. Later, three-point functions are introduced[1].

4.1 Euclidean Correlator

In Euclidean space, the correlation function of two gauge invariant operators $\mathcal{O}(t_1)$ and $\mathcal{O}(t_2)$[2] is defined as

$$\langle \mathcal{O}_1(t_1)\mathcal{O}_2(t_2)\rangle = \frac{1}{Z_T}\mathrm{tr}\{e^{-(T-t_1)\hat{H}}\hat{\mathcal{O}}_1 e^{-(t_1-t_2)\hat{H}}\hat{\mathcal{O}}_2 e^{-t_2\hat{H}}\}, \quad t_2 < t_1. \tag{4.1.1}$$

Here, $\hat{H}$ labels the Hamiltonian operator which generates the time evolution of a quantum state and measures the energy of the system. Euclidean time $t_1 = an_{1t}$ and $t_2 = an_{2t}$ are real time distances and $T = aL_t$ denotes the extension of the lattice in time direction. $\hat{\mathcal{O}}_1$ and $\hat{\mathcal{O}}_1$ are the operators in the Hilbert space. $Z_T = \mathrm{tr}[e^{-T\hat{H}}]$ is the partition function and the vacuum energy (vacuum state $|n\rangle = |0\rangle$) is normalized to $E_0 = 0$

To compute correlation functions we need two relations: one is the completeness relation

$$\mathbb{1} = \sum_n |e_n\rangle\langle e_n| \tag{4.1.2}$$

for a discrete orthonormal basis and the other is the definition of the trace of an operator

$$\mathrm{tr}[\hat{\mathcal{O}}] = \sum_n \langle e_n|\hat{\mathcal{O}}|e_n\rangle. \tag{4.1.3}$$

[1] We follow [GL10, Hor00] and chapter 4 [Brö07].

[2] According to the Heisenberg picture, a time dependent operator can be written in the form of $\hat{O}(t) = e^{it\hat{H}}\hat{O}e^{-it\hat{H}}$ where $\hat{H}$ is the Hamiltonian.

To calculate (4.1.1), we need to sandwich the operators between the basis of eigenstates $|n\rangle$ of the Hamiltonian $\hat{H}$

$$e^{-T\hat{H}}|n\rangle = e^{-TE_n}|n\rangle. \tag{4.1.4}$$

The state $|0\rangle$ is the vacuum state ($E_0 = 0$) and the energies E_n are assumed in ascending orders $E_0 \leq E_1 \leq E_2 \leq \dots$. The partition function Z_T by means of Eq. (4.1.3) becomes

$$Z_T = \sum_n \langle n|e^{-T\hat{H}}|n\rangle = \sum_n e^{-TE_n} \tag{4.1.5}$$

where the sum is over the exponentials of all energy eigenstates. The result is independent of any choice of basis.

The Euclidean correlation function Eq. (4.1.1) can be evaluated using Eq. (4.1.2) and using Eq. (4.1.3)

$$\begin{aligned}\langle \mathcal{O}_1(t_1)\mathcal{O}_2(t_2)\rangle_T &= \frac{\sum_{m,n}\langle n|e^{-(T-t_1)\hat{H}}\hat{\mathcal{O}}_1|m\rangle\langle m|e^{-(t_1-t_2)\hat{H}}\hat{\mathcal{O}}_2|m\rangle\langle m|e^{-t_2\hat{H}}|n\rangle}{\sum_n\langle n|e^{-T\hat{H}}|n\rangle} \\ &= \frac{\sum_{m,n} e^{-(T-t_1)E_n}\langle n|\hat{\mathcal{O}}_1|m\rangle e^{-(t_1-t_2)E_m}\langle m|\hat{\mathcal{O}}_2|n\rangle e^{-t_2E_n}}{\sum_n e^{-TE_n}}.\end{aligned} \tag{4.1.6}$$

Here, also Eq. (4.1.4) has been used in the second line. By defining $\Delta t = t_1 - t_2$ the above equation reduces to

$$= \frac{\sum_{m,n} e^{-(T-\Delta t)E_n}\langle n|\hat{\mathcal{O}}_1|m\rangle e^{-\Delta tE_m}\langle m|\hat{\mathcal{O}}_2|n\rangle}{\sum_n e^{-TE_n}}. \tag{4.1.7}$$

We can see that the correlation function depends only on the separation time Δt and we can therefore, set $t_2 = 0$ and $\Delta t = t$. In the limit of $T \to \infty$ we obtain

$$\lim_{T\to\infty}\langle \mathcal{O}_1(t)\mathcal{O}_2(0)\rangle_T = \sum_m \langle 0|\hat{\mathcal{O}}_1|m\rangle\langle m|\hat{\mathcal{O}}_2|0\rangle e^{-tE_m}. \tag{4.1.8}$$

Here, the sum is over all energy eigenstates and the summands are products of amplitudes and exponential functions of t times the energy level. The expectation values in Eq. (4.1.8) are taken between the vacuum $|0\rangle$ and the physical state $|m\rangle$.

For a specific particle p, we define $\hat{\mathcal{O}}_1 = \hat{\mathcal{O}}_p^\dagger$ as a creation operator and $\hat{\mathcal{O}}_2 = \hat{\mathcal{O}}_p$ as the annihilator. Consequently all expectation values for states $|m\rangle$ which do not have the desired quantum number of the meson will vanish. $\langle m| = \langle p|$ is the state describing the meson in the ground state and $\langle p'|$, $\langle p''|$ and $\dots$ denote contributions from excited states. Therefore,

$$\lim_{T\to\infty}\langle \mathcal{O}_p(t)\mathcal{O}_p^\dagger(0)\rangle_T = |\langle p|\hat{\mathcal{O}}_p^\dagger|0\rangle|^2\, e^{-tE_p} + |\langle p'|\hat{\mathcal{O}}_p^\dagger|0\rangle|^2\, e^{-tE_{p'}+} + \cdots \tag{4.1.9}$$

where the definition of the adjoint operator $\hat{O}^\dagger$ is

$$\langle u|\hat{O}|v\rangle = \langle v|\hat{O}^\dagger|u\rangle^*. \tag{4.1.10}$$

In chapter 5 we will see that at sufficient large t, excited state energies are exponentially suppressed so we can truncate the expansion after the first or second state.

	$\mathcal{P}$	$\mathcal{C}$	$\mathcal{T}$
$U_4(\boldsymbol{x},\tau)$	$U_4(-\boldsymbol{x},\tau)$	$U_4^*(\boldsymbol{x},\tau)$	$U_{-4}(\boldsymbol{x},-\tau)$
$U_i(\boldsymbol{x},\tau)$	$U_{-i}(-\boldsymbol{x},\tau)$	$U_i^*(\boldsymbol{x},\tau)$	$U_i(\boldsymbol{x},-\tau)$
$\psi(\boldsymbol{x},\tau)$	$\gamma_4\psi(-\boldsymbol{x},\tau)$	$\mathcal{C}\bar{\psi}^T(\boldsymbol{x},\tau)$	$\gamma_4\gamma_5\psi(\boldsymbol{x},-\tau)$
$\bar{\psi}(\boldsymbol{x},\tau)$	$\bar{\psi}(-\boldsymbol{x},\tau)\gamma_4$	$-\psi^T(\boldsymbol{x},\tau)\mathcal{C}^{-1}$	$\bar{\psi}(\boldsymbol{x},-\tau)\gamma_5\gamma_4$

Table 4.1.1: The behavior of quark fields and link variables under the parity, charge-conjugation, and time reversal. Superscript $*$ stands for the complex conjugate and T for transpose. The parity transformation gives a factor γ_4 from the quark and a factor γ_4^T from the anti-quark (look at Appendix A.1 and A.2).

4.1.1 Construction of Meson Interpolators

Interpolators are constructed of quark fields such that they have the desired quantum numbers of the physical state. On the lattice, discretization breaks many symmetries valid in the continuum. Discrete symmetries like Charge conjugation $\mathcal{C}$ and parity $\mathcal{P}$ are important to construct the hadron interpolators.

Charge conjugation transforms particles into anti-particles which generally carry opposite electric charge. Charge conjugation transformation depends on the chosen $\gamma-$matrices representations. We have [B+97]

$$\mathcal{C}\gamma_\mu\mathcal{C}^{-1} = -\gamma_\mu^T, \quad \mu \in [1,2,3,4] \tag{4.1.11}$$

$$\mathcal{C}\gamma_5\mathcal{C}^{-1} = \gamma_5^T = \gamma_5, \tag{4.1.12}$$

$$\mathcal{C}^\dagger = -\mathcal{C}, \quad \mathcal{C}^T = -\mathcal{C}, \quad \mathcal{C}^{-1} = -\mathcal{C}, \tag{4.1.13}$$

$$\mathcal{C}\,D^{-1}(x,y;U)\,\mathcal{C}^{-1} = D^{-1}(x,y;U^*)^T. \tag{4.1.14}$$

The behavior of link variables and fermion fields under the charge conjugate transformation and parity is given in Table 4.1.1.

In order to construct the meson interpolators the following degrees of freedom of particles are considered [Gri08]:

1. $SU(3)$ color symmetry; to have colorless physical particles, mesons must consist of a quark and an anti-quark with a color and anti-color combination. So the proper color structure is

$$\delta_{ab} \tag{4.1.15}$$

   where $a\,(b)$ is the color (anti-color) of the quark (anti-quark).

2. $SU(2)$ flavors; for two particles with identical interactions, i.e. any linear combination of these two particles give the same physics.

3. $SU(2)$ spin; the singlet state $\big(|0,0\rangle = \frac{1}{\sqrt{2}}(\uparrow\downarrow - \downarrow\uparrow)\big)$ of two particles with spin $1/2$ which total spin is 0. Quark and anti-quark combine with either $\mathbb{1}$ or γ_5.

particle	Isospin	J^{PC}	Γ	Operator	mass(MeV)
π^-	$I=1,\, I_z=-1$	0^-	γ_5	$\bar{u}\gamma_5 d$	139.6
π^0	$I=1,\, I_z=0$	0^{-+}	γ_5	$\frac{1}{\sqrt{2}}(\bar{u}\gamma_5 u - \bar{d}\gamma_5 d)$	134.9
π^+	$I=1, I_z=+1$	0^-	γ_5	$\bar{d}\gamma_5 u$	139.6

Table 4.1.2: Quantum numbers of π mesons. Masses are from [B+12].

4. Parity; considering a pseudoscalar meson, a parity transformation $\mathcal{P}$ acts on it as

$$M(\vec{x},t) \quad \xrightarrow{\mathcal{P}} \quad M(-\vec{x},t). \tag{4.1.16}$$

Since we sum over all spatial vectors, parity transformations are irrelevant for interpolators.

By considering all mentioned symmetries, meson interpolators can be written as follows

$$O_M = \delta_{ab}\bar{\psi}^{(f_1)}_{a\alpha}(\vec{x},t)\,\Gamma_{\alpha\beta}(\vec{x},\vec{y})\,F^{ab}\psi^{(f_2)}_{b\beta}(\vec{y},t) \tag{4.1.17}$$

where α,β stand for Dirac indices, a,b for color, f_1, f_2 for flavor and F^{ab} is the so-called the *flavor matrix*. The quark field ψ for $N_f = 2$ is defined as

$$\psi^{(u)}_{a\alpha}, \quad \psi^{(d)}_{a\alpha}. \tag{4.1.18}$$

The matrix Γ is a gauge invariant product of gamma matrices and link variables. The form of Γ allows us to have different possibilities for quark and anti-quark positions. One is to place quark and anti-quark on different lattice sites. The other one is to place them on the same site to have a point-like interpolator and then extend it by means of the smearing function which is explained in section 4.2. In point-like interpolators, the Γ is defined like $\Gamma^{\alpha\beta}_{ab}(x,y) = \delta_{x,y}\delta_{ab}\mathcal{M}_{\alpha\beta}$, where $\mathcal{M}_{\alpha\beta}$ is a product of γ_μ matrices.

Pions are made from pairs of valence up and down quarks. An up quark u has isospin $I = \frac{1}{2}$, $I_z = +\frac{1}{2}$ and charge $Q = \frac{2}{3}e$ and for down-quark d we have $I = \frac{1}{2}$, $I_z = -\frac{1}{2}$ and $Q = -\frac{1}{3}e$. The charge of an electron is $-e$. In order to get the correct charge and isospin regarding the up and down quarks properties, π^+ has to be made by $\bar{d} - u$ and π^- has combination of $\bar{u} - d$. The quantum numbers of π mesons are brought in Table 4.1.2.

By using the behavior of quark fields under parity transformation shown in Table 4.1.1 and $\gamma_4\gamma_5\gamma_4 = -\gamma_5$, we will see that pions are parity eigenstates with negative eigenvalue, $\hat{P}|\pi^+\rangle = -|\pi^+\rangle$, $\hat{P}|\pi^0\rangle = -|\pi^0\rangle$. Also charge conjugation transformation gives

$$\begin{aligned}\hat{\mathcal{C}}|\pi^+\rangle &= \hat{\mathcal{C}}|\bar{d}(x,t)\gamma_5 u(x,t)\rangle = |-d(x,t)^T\,\mathcal{C}^{-1}\gamma_5\mathcal{C}\,\bar{u}(x,t)^T\rangle \\ &= |-d^T(x,t)\,\gamma_5^T\,\bar{u}(x,t)^T\rangle = |\bar{u}(x,t)\,\gamma_5\,d(x,t)\rangle = |\pi^-\rangle\end{aligned} \tag{4.1.19}$$

and similarly

$$\hat{\mathcal{C}}|\pi^0\rangle = +|\pi^0\rangle \tag{4.1.20}$$

where we used Eq. (4.1.12). In the last step we get a minus sign from interchange of the Grassmann variables (explained in section 3.3). For a complete explanation also see [Per82].

4.1.2 Construction of Two-Point Function

Now we define the correlation function of two meson interpolators with the use of Eq. (4.1.17)

$$\begin{aligned}&\langle \mathcal{O}_1(n)\, \mathcal{O}_2(m)\rangle \\ &= \langle \bar{\psi}_{a\alpha}(n)\, \Gamma_{\alpha\beta} F_{ab} \psi_{b\beta}(n)\, \bar{\psi}_{a'\alpha'}(m)\, \Gamma'_{\alpha'\beta'} F'_{a'b'}\, \psi_{b'\beta'}(m)\rangle \end{aligned} \tag{4.1.21}$$

where $\alpha, \beta, \alpha', \beta'$ are Dirac and a, b, a', b' flavor. We then can write

$$\begin{aligned}&= F_{ab}\, F'_{a'b'}\, \Gamma_{\alpha\beta}\, \Gamma'_{\alpha'\beta'} \langle \bar{\psi}_{a\alpha}(n)\, \psi_{b\beta}(n)\, \bar{\psi}_{a'\alpha'}(m)\, \psi_{b'\beta'}(m)\rangle \\ &= F_{ab}\, F'_{a'b'}\, \Gamma_{\alpha\beta}\, \Gamma'_{\alpha'\beta'} \langle \psi \overbrace{{}_{b\beta}(n)\, \bar{\psi}_{a\alpha}}(n)\rangle \langle \psi \overbrace{{}_{b'\beta'}(m)\, \bar{\psi}_{a'\alpha'}}(m)\rangle \\ &\quad - \langle \psi \overbrace{{}_{b\beta}(n) \bar{\psi}_{a'\alpha'}}(m)\rangle \langle \psi \overbrace{{}_{b'\beta'}(m) \bar{\psi}_{a\alpha}}(n)\rangle \\ &= F_{ab}\, F'_{a'b'}\, \Gamma_{\alpha\beta}\, \Gamma'_{\alpha'\beta'} \Big(\delta_{ba} \langle G_{\beta\alpha}(n|n)\rangle \delta_{b'a'} \langle G_{\beta'\alpha'}(m|m)\rangle \\ &\quad - \delta_{ba'} \langle G_{\beta\alpha'}(n|m)\rangle \delta_{b'a} \langle G_{\beta'\alpha}(m|n)\rangle \Big) \end{aligned} \tag{4.1.22}$$

where the Kronecker delta expresses that just the contractions of quarks with the same flavor are non-zero and the rest vanish. In Eq. (4.1.22) we used the definition of the quark propagator

$$\langle \psi(n)_{\substack{\alpha \\ a}} \bar{\psi}(m)_{\substack{\beta \\ b}} \rangle = D^{-1}(n|m)_{\substack{\alpha\beta \\ ab}}. \tag{4.1.23}$$

Then we get

$$\begin{aligned}&= (\mathrm{tr}F')(\mathrm{tr}F)\mathrm{tr}_{DC}(\Gamma D^{-1}(n|n)\Gamma' D^{-1}(m|m)) \\ &\qquad - \mathrm{tr}(FF')\mathrm{tr}_{DC}(\Gamma D^{-1}(n|m)\Gamma' D^{-1}(m|n)). \end{aligned} \tag{4.1.24}$$

In the last step, trace was over the Dirac indices

$$F_{ab}\delta_{ba} F'_{a'b'}\delta_{b'a'} = \mathrm{tr}(F)\mathrm{tr}(F'), \tag{4.1.25}$$

$$F_{ab}\delta_{ba'} F'_{a'b'}\delta_{b'a} = \mathrm{tr}(FF'). \tag{4.1.26}$$

$D^{-1}(n|m)$ is the quark propagator from space-time point m to point n and $D^{-1}(m|n)$ in the opposite direction. The contributions in (4.1.26) are so-called *connected contributions*. The quark propagator $D^{-1}(n|n)$ from a space-time point n back to the same point n contributes to the so-called *disconnected contributions*

$$(\mathrm{tr}F')(\mathrm{tr}F)\mathrm{tr}_{DC}(\Gamma D^{-1}(n|n)\Gamma' D^{-1}(m|m)). \tag{4.1.27}$$

Connected and Disconnected parts are schematically shown in Fig. 4.1.1.

Using the charge conjugation $\mathcal{C}$ Eq. (4.1.11)-(4.1.14) we see that because the configurations are complex conjugate, disconnected contributions change the sign while the

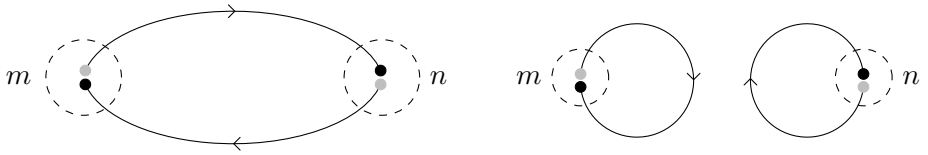

Figure 4.1.1: Connected (l.h.r) and disconnected (r.h.s) terms of a meson correlator

gauge action Eq. (3.2.26) is invariant under the transformation. So by averaging over all ensembles the disconnected contributions vanish. More detailed are in [D+89].

For π^+, the interpolating fields for sink and source are represented as follows

$$\begin{aligned} h_1(\vec{x}_1,t) &= \bar{d}_{a\alpha}(\vec{x}_1,t)\,\Gamma_{\alpha\beta}u_{a\beta}(\vec{x}_1,t), \\ h_1^\dagger(\vec{x}_1,t) &= \Big(\bar{d}_{a\alpha}(\vec{x}_1,t)\,\Gamma_{\alpha\beta}u_{a\beta}(\vec{x}_1,t)\Big)^\dagger \\ &= -\bar{u}_{a\beta}(\vec{x}_1,t)\Gamma_{\alpha\beta}d_{a\alpha}(\vec{x}_1,t) \end{aligned} \tag{4.1.28}$$

In these equations the position of space-time points are arbitrary but in the next section we will discuss how to place the quark and anti-quark and expand them to get the better overlap with the ground system.

4.2 Source and Sink Smearing

For the calculation of a simple two-point function, the computation of the quark propagator (inverse of the Dirac operator) is necessary. The lattice Dirac operator acts on the tensor product of three vector spaces: the spin space (N_s), the color space (N_c) and the lattice space (N_v) of dimension N (the number of lattice sites). The lattice space itself is a tensor product of spatial and temporal spaces

$$N = L_x L_y L_z L_t. \tag{4.2.1}$$

where L_i ($\hat{i} = x, y, z, t$) means length of the lattice in the direction $\hat{i}$. The Dirac operator is therefore a $12N \times 12N$ matrix in the full vector space

$$D(a,\alpha,x,y,z,t;b,\beta,x',y',z',t'). \tag{4.2.2}$$

4.2.1 Point Source

The quark propagator describes a quark propagating from one source point $n = (a,\alpha,x,y,z,t)$ to a sink point $m = (b,\beta,x',y',z',t')$ with link $U_\mu(n)$ starting from site n in direction $\hat{\mu}$ ($\hat{x}$, $\hat{y}$, $\hat{z}$ or t). Points n and m run over the whole lattice and U_μ are matrices which change from link to link and many times during the runs. An *All-to-all* propagator is for a quark traveling form every point of lattice to every other point.

Inverting the full D requires large amounts of both time and computer power. The substituting solution so-called *point-to-all* propagator is to consider a quark traveling from a fixed lattice site m_0 with a fixed color and Dirac index (a_0,α_0) to any other

site of the lattice n. Multiplying the full propagator $D^{-1}(n|m)$ by a matrix $S_0(m|m_0)$ so-called *point-source*, gives us the point-to-all propagator

$$D^{-1}(n|m_0)_{\substack{\beta\alpha_0\\ba_0}} = \sum_{m,\alpha,a} D^{-1}(n|m)_{\substack{\beta\alpha\\ba}} S_0(m|m_0)_{\substack{\alpha\alpha_0\\aa_0}}. \tag{4.2.3}$$

Here, the point source $S_0(m|m_0)_{\substack{\alpha\alpha_0\\aa_0}} = \delta_{mm_0}\delta_{\alpha\alpha_0}\delta_{aa_0}$ picks out one column of all-to-all propagator $D^{-1}(n|m)$. In order to calculate a correlation function, the quark propagator in the inverse direction $D^{-1}(m_0|m)$ is necessary. The Wilson-Dirac operator in Euclidean space-time is γ_5-hermitic. Therefore, for D we have

$$\gamma_5 D(m|m_0)\gamma_5 = D^\dagger(m_0|m). \tag{4.2.4}$$

So we get $D^{-1}(m_0|m)$ from applying γ_5–matrices to $D^{-1}(m|m_0)$. Point-to-all method does not require massive computing power. However, it throws away a large portion of the information contained in the gauge configurations. By omitting Dirac and color indices and defining $D^{-1}(n|m_0) = G(n|m_0)$, we can rewrite (4.2.3) as

$$G(n|m_0) = \sum_m D^{-1}(n|m)S_0(m|m_0). \tag{4.2.5}$$

Multiplying the above equation with the Dirac operator from the left provides

$$\sum_n D(m|n)G(n|m_0) = S_0(m|m_0). \tag{4.2.6}$$

The Dirac operator $D(m|n)$ is a sparse matrix which means most of its elements are zero. This sparse linear system (4.2.6) can be solved by different iterative methods where $D(m|n)$ and $S_0(m|m_0)$ are known and $G(n|m_0)$ is the unknown solution to Eq. (4.2.6). Popular solvers employ Krylov subspace method [Saa]. Conjugate gradient algorithm (CG) [Fle88] is a prototype of a Krylov space solver which has stable convergence but it is slow. Another one is the Bi-Conjugate gradient stabilized algorithm (BiCGStab) [vdV92] which is faster than CG but sometimes it does not converge. Other solvers that recently are used are Multigrid method which is a very effective iterative method [F+12] and domain decomposition [Lus07]. For a comprehensive overview we refer to [Lus10].

4.2.2 Overlap Improvement

Using a point source S_0 means that a quark and anti-quark sit on the same lattice site. Since hadrons are not point-like objects, using point sources makes the overlap with the physical state small. To have a more realistic spatial positioning, an extended source, so-called *smeared source*, is used. In this method, quarks are placed on different spatial points but on the same time-slice.

There are different ways to implement gauge invariant smearing, two popular methods are *Jacobi smearing* [A+93] and *Wuppertal smearing* (also called Gaussian smearing) [Gus90].

4.2.2.1 Quark Smearing

For Jacobi smearing, one acts with a smearing operator $M(n|m')$ with (i) times of smearing steps on the point source quark field $\psi(m)^{(0)}$ [A+93]

$$\psi(n)^{(i)} = \sum_m M^{(i)}(n,m)\,\psi(m)^{(0)}. \tag{4.2.7}$$

The smearing operator M is defined as

$$M^{(i)}(n,m) = \sum_{i=0}^{N_{smear}} \kappa^i H(n,m)^i, \tag{4.2.8}$$

where $H(n,m) = \sum_{j=1}^{3} \left(U_j(n)\delta_{n+\hat{j},m} + U_j^\dagger(n-\hat{j})\delta_{n-\hat{j},m}\right)$ and j is used for spatial directions only. In Eq. (4.2.8), κ controls the amplitude of the iteration to get the best practicable overlap with the physical state.

For Wuppertal smearing, the smeared field ψ is defines as [Gus90]

$$\psi^{(i+1)}(n) = \frac{1}{1+2d\alpha}\Big[\psi^{(i)}(n) + \alpha \sum_{j=\pm1}^{\pm3} U_j(n)\psi^{(i)}(n+a\hat{j})\Big] \tag{4.2.9}$$

where i indicates the number of iterations, α the smearing parameter, $d = 3$ is spatial dimension and U_j the corresponding smeared link variable.

Wuppertal and Jacobi smearing are gauge covariant and translational invariant in space, so they can be applied in the inverse direction. The γ_5-hermiticity relation $\gamma_5 G(m_0|m)\gamma_5 = G^\dagger(m|m_0)$ is applicable for them as they are spin-diagonal. The extended source depends on the gauge link $U_j(n)$ which separates the quarks in spatial directions. The source smear propagator

$$G^s(n|m_0) = \sum_m D^{-1}(m|n)S^s(m|m_0) \tag{4.2.10}$$

can be solved via Eq. (4.2.6).

Moreover, the smearing can be applied on both sink and source and one can define source-sink-smeared propagator G^{ss}

$$\begin{aligned} G^{ss}(n|m_0) &= \sum_{m,n'} S(n|m)D^{-1}(m|n')S(n'|m_0) \\ &= \sum_m S(n|m)G^s(m|m_0) \end{aligned} \tag{4.2.11}$$

where the solution of Eq. (4.2.5) G^s was inserted into the second line.

4.2.2.2 Link Smearing

There are also some techniques called link smearing to improve the correlation signal which transforms the links to suppress short distance fluctuations (see e.g. [MP04, A+87, HK01]). This smearing process is achieved by locally averaging over link variables

along the specified paths which attached to the same endpoints of the link. Every link variable $U_\mu(n)$ is replaced by $U'_\mu(n)$ which is a weighted average of the link $U_\mu(n)$ and a sum of neighboring links $C^{(k)}_{ji}(n)$. In order to perform link smearing, one way is APE smearing which was proposed by APE Collaboration [A+87]. The linear combination is written as

$$U_j'^{(k+1)}(n) = (1-\alpha)U_j^{(k)}(n) + \frac{\alpha}{6}\sum_{|i|\neq j}^{\pm 3} C_{ji}^{(k)}(n), \tag{4.2.12}$$

where $U^{(k)}$ is the old link and staples are defined as

$$\begin{aligned} C_{ji}^{(k)}(n) =& U_i^{(k)}(n)U_j^{(k)}(n+\hat{i})U_i^{\dagger(k)}(n+\hat{j}) + \\ & U_i^{\dagger(k)}(n-\hat{i})U_j^{(k)}(n-\hat{i})U_i^{(k)}(n-\hat{i}+\hat{j}). \end{aligned} \tag{4.2.13}$$

Here, α denotes the smearing parameter and is chosen at which value the fluctuations are reduced most. Since APE smearing leaves the SU(3) group, it is necessary to project the new link variable back to SU(3)

$$\mathrm{Proj}_{SU(3)}(U'_j(n)) = \max\{\mathrm{Re}\,\mathrm{tr}(U_j(n)U'_j(n)^\dagger)\}. \tag{4.2.14}$$

4.3 Three-Point Functions

So far we discussed two-point function but for the matrix elements we also have to look at three-point functions. A matrix element has the form as

$$\langle X(p')|\hat{\mathcal{O}}|X(p)\rangle \tag{4.3.1}$$

where p and p' denote the momenta of the initial and final hadron states, respectively. The calculation is performed similar to the two-point function with an inserted current.

The general form of the current can be written as (see, e.g., [B+97])

$$\mathcal{O}(\tau) = \sum_{x,z,z'} e^{iq\cdot x} F_{ff'} \bar{\psi}^f_{\beta,b}(z) J^{bb'}_{\beta,\beta'}(z,z';x) \psi^{f'}_{\beta',b'}(z'). \tag{4.3.2}$$

For pions, ψ is either u or d and the current $J^{bb'}_{\beta,\beta'}(z,z';x)$ is a matrix which represents the flavor, Dirac and derivative structure of the operators. z and z' indicate J contains discretized derivatives. The interaction takes place at x ($x_4 = \tau$). Since the current J is diagonal in color, one can sum over color indices (b,b'). In this work we neglect the change of flavors in the current, therefore $f = f'$.

The general form of the three-point function describing a pion probed by an operator $\mathcal{O}(\tau,z)$ at insertion time τ is given by [Hag10]

$$C^{\mathcal{O}}_{3pt}(\tau,p',p) = \langle h(p',t_{sink})\mathcal{O}(q,\tau)h^\dagger(p,0)\rangle. \tag{4.3.3}$$

Here, $h^\dagger(p,0)$ and $h(p',t_{sink})$ (see Eq. (4.1.28)) are interpolating fields at source ($t=0$) and sink ($t' = t_{sink}$) respectively. Similar to two-point functions, by inserting a complete

set of eigenstates of Hamiltonian basis vectors and time evolution operator, Eq. (4.3.3) can be written as

$$C^{\mathcal{O}}_{3pt}(\tau,p',p) = \begin{cases} \langle e^{-(T-t_{sink})\hat{H}} h(\vec{p}\,') e^{-(t_{sink}-\tau)\hat{H}} \mathcal{O}(\vec{q}) e^{-\tau\hat{H}} h^{\dagger}(p)\rangle, & 0 \le \tau \le t_{sink} \\ \langle e^{-(T-\tau)\hat{H}} \mathcal{O}(\vec{q}) e^{-(\tau-t_{sink})\hat{H}} h(\vec{p}\,') e^{-t_{sink}\hat{H}} h^{\dagger}(p)\rangle, & t_{sink} \le \tau \le T \end{cases} \tag{4.3.4}$$

$$C^{\mathcal{O}}_{3pt}(\tau,p',p) = \langle 0|h(\vec{p}\,')|\pi(p')\rangle\langle\pi(p')|\mathcal{O}(\vec{q})|\pi(p)\rangle\langle\pi(p)|h^{\dagger}(p)|0\rangle \times \begin{cases} e^{-(t_{sink}-\tau)E(p')-\tau E(p)} + \cdots, & 0 \le \tau \le t_{sink} \\ (-1)^{n_4+n_5} e^{-(\tau-t_{sink})E(p')-(T-\tau)E(p)} + \cdots, & t_{sink} \le \tau \le T \end{cases} \tag{4.3.5}$$

with momentum transfer $q = \big(i(E_{\vec{p}\,'} - E_{\vec{p}}), \vec{p}\,' - \vec{p}\big)$. In Eq. (4.3.5) we assume that h and $h^{\dagger}$ have the correct symmetry properties. The Hilbert space operator h creates the proper wanted particle from the vacuum with non-zero amplitude [B+97]

$$\langle 0|h(p)|\pi(p)\rangle = \sqrt{Z_{\pi}(p)}. \tag{4.3.6}$$

We have to keep in mind that two- and three-point functions have to be multiplied with an additional factor

$$\frac{C_{2pt}(t,\vec{p})}{2E_{\pi}(\vec{p})}, \tag{4.3.7}$$

$$\frac{C_{3pt}(t,\tau,\vec{p},\vec{p}\,')}{4E_{\pi}(\vec{p})E_{\pi}(\vec{p}\,')} \tag{4.3.8}$$

to get physical matrix elements.

We should note that the matrix elements on a Euclidean lattice and continuum Minkowski-space have different normalization

$$\langle\pi(\vec{p})|\pi(\vec{p}\,')\rangle_{lat} = \delta_{\vec{p},\vec{p}\,'}, \tag{4.3.9}$$

$$\langle\pi(\vec{p})|\pi(\vec{p}\,')\rangle_{cont} = (2\pi)^3 2E(\vec{p})\delta(\vec{p}-\vec{p}\,'). \tag{4.3.10}$$

They are related with each other via the expression

$$\langle\pi(\vec{p})|\mathcal{O}^{latt}(\tau,p',p)|\pi(\vec{p}\,')\rangle = \frac{\langle\pi(\vec{p})|\mathcal{O}(\tau,p',p)^{cont}|\pi(\vec{p}\,')\rangle}{4E(\vec{p})E(\vec{p}\,')}. \tag{4.3.11}$$

The result is

$$C^{\mathcal{O}}_{3pt}(\tau,p',p) = \frac{\sqrt{Z_{\pi}(p')Z_{\pi}(p)}}{4E(\vec{p})E(\vec{p}\,')} \langle\pi(p')|\mathcal{O}(\vec{q})|\pi(p)\rangle \times \Big(e^{-(t_{sink}-\tau)E(p')-\tau E(p)} + (-1)^{n_4+n_5} e^{-(\tau-t_{sink})E(p')-(T-\tau)E(p)}\Big) + \cdots. \tag{4.3.12}$$

Here, n_4 and n_5 are the number of γ_4 and γ_5 matrices and $\cdots$ refers to contributions from excited states which are suppressed in the limit $t_{sink}-\tau \gg 1/(E'-E)$ or $\tau - t_{src} \gg 1/(E'-E)$. The pion source is set at 0, so $t' = 0$.

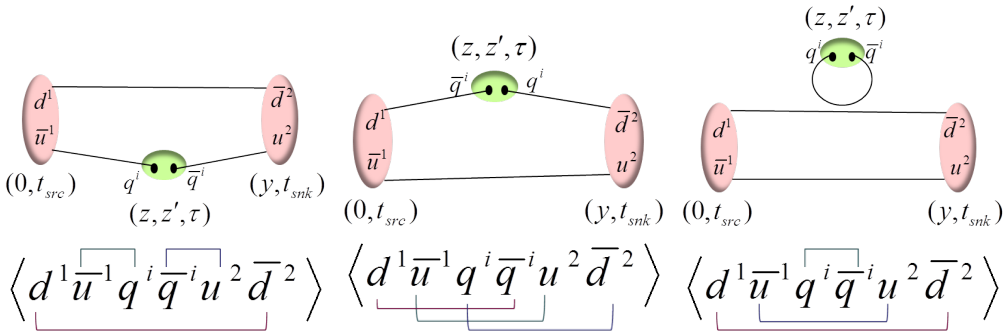

Figure 4.3.1: The three-point quark correlation function for a pion. The left and middle diagrams represent the quark connected part while the right picture is the quark disconnected part.

4.3.1 Construction of Three-point Function

For simplicity, we set the pion source at $\mathbf{0}$. By using the operators defined in Eq. (4.3.2) and the π^+ interpolators in Eq.(4.1.28) three-point function can be written in Fourier space as

$$\langle h_{\pi^+}(p',t)\mathcal{O}(\tau)h^\dagger_{\pi^+}(p,0)\rangle = \sum_y \sum_{z,z'} e^{-ip'\cdot y} e^{iq\cdot x} F_{ff'} \times$$
$$\langle \bar{d}_{\alpha,a}(y)\Gamma_{\alpha,\alpha'} u_{\alpha',a}(y)\, \bar{\psi}^f_{\beta,b}(z) J^{b,b'}_{\beta,\beta'}(x;z,z')\psi^{f'}_{\beta',b'}(z')\, \bar{u}_{\gamma,c}(0)\Gamma'_{\gamma,\gamma'} d_{\gamma',c}(0)\rangle. \quad (4.3.13)$$

By reordering the Grassmann variables and applying Wick's theorem [GL10], we obtain

$$\begin{aligned}\langle h_{\pi^+}(p',t)\mathcal{O}(\tau)h^\dagger_{\pi^+}(p,0)\rangle = \sum_y \sum_{x,z,z'} & e^{-ip'\cdot y}\, e^{iq\cdot x} F_{ff'}\Gamma_{\alpha,\alpha'} J^{b,b'}_{\beta,\beta'}(x;z,z')\Gamma'_{\gamma,\gamma'}\{ \\ & - \langle u_{\alpha',a}(y)\bar{\psi}^f_{\beta,b}(z)\rangle\langle \psi^{f'}_{\beta',b'}(z')\bar{u}_{\gamma,c}(0)\rangle\langle d_{\gamma',c}(0)\bar{d}_{\alpha,a}(y)\rangle \\ & + \langle u_{\alpha',a}(y)\bar{u}_{\gamma,c}(0)\rangle\langle d_{\gamma',c}(0)\bar{d}_{\alpha,a}(y)\rangle\langle \psi^{f'}_{\beta',b'}(z')\bar{\psi}^f_{\beta,b}(z)\rangle \\ & - \langle u_{\alpha',a}(y)\bar{d}_{\alpha,a}(y)\rangle\langle \psi^{f'}_{\beta',b'}(z')\bar{\psi}^f_{\beta,b}(z)\rangle\langle d_{\gamma',c}(0)\bar{u}_{\gamma,c}(0)\rangle \\ & - \langle \psi^{f'}_{\beta',b'}(z')\bar{d}_{\alpha,a}(y)\rangle\langle u_{\alpha',a}(y)\bar{u}_{\gamma,c}(0)\rangle\langle d_{\gamma',c}(0)\bar{\psi}^f_{\beta,b}(z)\rangle \\ & - \langle u_{\alpha',a}(y)\bar{d}_{\alpha,a}(y)\rangle\langle \psi^{f'}_{\beta',b'}(z')\bar{u}_{\gamma,c}(0)\rangle\langle d_{\gamma',c}(0)\bar{\psi}^f_{\beta,b}(z)\rangle\}. \end{aligned} \quad (4.3.14)$$

Wick's theorem says that only diagonal elements of F contribute, so the contractions in the third and fifth lines are zero. Using the definition of Eq.(4.1.23) we get

$$\begin{aligned} = \sum_y \sum_{x,z,z'} & e^{-ip'\cdot y} e^{iq\cdot x}\langle -F_{uu}\Gamma_{\alpha\alpha'} \underset{ab}{D^{-1}_{\alpha'\beta}}(y|z) J^{bb'}_{\beta,\beta'}(x;z,z') \underset{b'c}{D^{-1}_{\beta'\gamma}}(z'|0)\Gamma'_{\gamma\gamma'} \underset{ca}{D^{-1}_{\gamma',\alpha}}(0|y) \\ & + (F_{dd}+F_{uu})\Gamma_{\alpha\alpha'} \underset{ac}{D^{-1}_{\alpha'\gamma}}(y|0)\Gamma'_{\gamma\gamma'} \underset{ca}{D^{-1}_{\gamma'\alpha}}(0,y) J^{bb'}_{\beta\beta'}(x;z,z') \underset{b'b}{D^{-1}_{\beta'\beta}}(z',z) \\ & - F_{dd} \underset{b'a}{D^{-1}_{\beta'\alpha}}(z'|y)\Gamma_{\alpha\alpha'} \underset{ac}{D^{-1}_{\alpha'\gamma}}(y,0)\Gamma'_{\gamma\gamma'} \underset{cb}{D^{-1}_{\gamma'\beta}}(0,z) J^{bb'}_{\beta\beta'}(x;z,z')\rangle \end{aligned} \quad (4.3.15)$$

$$= \sum_y \sum_{x,z,z'} e^{-ip'\cdot y} e^{iq\cdot x} \langle -F_{uu} \mathrm{tr}[\Gamma D^{-1}(y|z) J(x;z,z') D^{-1}(z'|0) \Gamma' D^{-1}(0|y)]$$
$$+ (F_{dd} + F_{uu}) \,\mathrm{tr}[\Gamma D^{-1}(y|0) \Gamma' D^{-1}(0|y)] \,\mathrm{tr}[J(x;z,z') D^{-1}(z'|z)]$$
$$- F_{dd} \,\mathrm{tr}[D^{-1}(z'|y) \Gamma D^{-1}(y|0) \Gamma' D^{-1}(0|z) J(x;z,z')] \rangle \tag{4.3.16}$$

where for pions $\Gamma = \Gamma' = \gamma_5$. The first and third lines denote the fermion connected contributions shown in Fig. 4.3.1 (left and middle), and the second line the fermion disconnected part (right in Fig. 4.3.1).

4.3.1.1 Connected Contributions

The quark line connected part of the three-point function in the path integral is represented diagrammatically in Fig. 4.3.1. We see that the hadron interpolating quark fields contract with the quark fields of the current so that the quark lines flow continuously from $t = 0$ at the source to $t = t$ at the sink. The two fermion-line connected terms are related by using γ_5-hermiticity [B+97]

$$\gamma_5 \Gamma = s \Gamma^\dagger \gamma_5 \tag{4.3.17}$$
$$\gamma_5 \Gamma' = s' \Gamma'^\dagger \gamma_5 \tag{4.3.18}$$
$$\gamma_5 J(x;z,z')^\dagger \gamma_5 = s_j J(x;z,z') \tag{4.3.19}$$
$$G(x,y)^\dagger = \gamma_5 G(y,x) \gamma_5. \tag{4.3.20}$$

Eq. (4.3.19) assumes that J is symmetric in its space-time indices with symmetrization factors $s, s', s_j = \pm 1$. In Eq. (4.3.20) G is a fermion propagator. For the pion, $\Gamma = \Gamma' = \gamma_5$, hence $s = s' = 1$. Then the three-point correlation function for the connected part in Eq. (4.3.16) becomes

$$- \sum_y \sum_x x e^{-ip'\cdot y} e^{iq\cdot x} (F_{uu} M(x,y) + s s' s_j F_{dd} M(x,y)^*) \tag{4.3.21}$$

where $M(x,y)$ is

$$M(x,y) = \sum_{z,z'} \langle \mathrm{tr}[\Gamma D^{-1}(y|z) J(x;z,z') D^{-1}(z'|0) \Gamma' D^{-1}(0|y)] \rangle. \tag{4.3.22}$$

Now we want to check the behavior of the connected contribution under charge conjugation. We follow the notation of [B+97]. Using the definition of the charge conjugation matrix

$$\gamma_\mu^T = -C^{-1} \gamma_\mu C \tag{4.3.23}$$

and the relations

$$C \Gamma^T C^{-1} = \sigma \Gamma \tag{4.3.24}$$
$$C \Gamma'^T C^{-1} = \sigma' \Gamma' \tag{4.3.25}$$
$$C J(U^*|x;z,z') C^{-1} = \sigma_J J(U|x;z,z') \tag{4.3.26}$$
$$G(U|0,y) = C G(U^*|y,0)^T C^{-1} \tag{4.3.27}$$

we can write

$$M(x,y)^* = \sigma\sigma'\sigma_J s s' s_J M(x,y) \tag{4.3.28}$$

where the current J is explicitly dependent on the gauge link U with the definition of $\sigma, \sigma', \sigma_J = \pm 1$. We finally arrive at an expression which relates $M(x,y)$ to the appropriate three-point function

$$\langle h_{\pi^+}(p',t)\mathcal{O}(\tau)h^\dagger_{\pi^+}(p,0)\rangle = -V_3 \sum_{x,y} e^{-i\vec{p}'\cdot\vec{y}} e^{i\vec{p}\cdot\vec{x}} (F_{uu} + \sigma_J F_{dd}) M(x,y). \tag{4.3.29}$$

Here σ_J is $(-1)^{n+n_5+1}$, where n is the number of covariant derivatives in operator. If the operator contains a γ_5 matrix, $n_5 = 1$ and otherwise it is 0.

4.3.1.2 Sequential Source Technique

We have to compute the expectation values of different quark propagators to evaluate the desired matrix elements. In order to calculate the connected contributions, it is necessary to calculate the inverse of the Dirac operator D^{-1} of all lattice points to all other lattice points

$$\mathrm{tr}\Big[\sum_z e^{iq\cdot z} D^{-1}(0|z) J(z) \sum_y e^{-iq\cdot y} D^{-1}(z|y)\gamma_5 D^{-1}(y|0)\Big]. \tag{4.3.30}$$

This calculation is quite expensive. To reduce the number of propagator calculations, we use the so-called sequential source method [B+86].

This method is as follows[3]: instead of using all-to-all propagators we calculate the quark propagators from point source $(0,0)$ to all other points of the lattice (y,t), as well as (using γ_5–hermiticity) from all other points (z,τ) to the source $(0,0)$. The remaining part is a propagator from all (y,t) to all (z,τ). The matrix element is written as

$$\mathrm{tr}\Big[\sum_{z,z_0=\tau} e^{iq\cdot z} D^{-1}(0|z) J(z) \Sigma(z|0)\gamma_5\Big]. \tag{4.3.31}$$

Here, $\Sigma(z,0)$ is sequential propagator which contains the quark propagator from all (y,t) to all (z,τ) and source $(0,0)$ to all (y,t). This propagator together with γ_5 and some phase factor use as a source

$$\Sigma(z|0) = \sum_{y,y_0=t} D^{-1}(z|y)\gamma_5 e^{-ip\cdot y} D^{-1}(y|0) \tag{4.3.32}$$

where $\gamma_5 e^{-ip\cdot y} D^{-1}(y|0)$ is called the sequential source. The advantage of this method is that with the same set of propagators, Σ and D, any current can be inserted at (z,τ) and any meson operators can be contracted at $(0,0)$ with no additional quark propagator calculations. But the disadvantage of this method is that by changing the properties of the sink, particularly p', the entire set of sequential propagators must be recomputed. One often sets the sink at one value of the final momentum.

[3] We follow the notation of [GL10]

4.4 Lattice Operators

Moments of pion structure functions are related to matrix elements of local operators. The operator product expansion (2.3.1) by means of Mellin moments (2.3.2) reads [G+96b]

$$2\int_0^1 dx\, x^n\, F_1(x,Q^2) = \sum_f c_{1,n}^{(f)}(\mu^2/Q^2, g(\mu)) v_n^{(f)}(\mu) + \cdots . \tag{4.4.1}$$

Here, $F_1(x,Q^2)$ are the unpolarized hadron structure functions. The superscript f denotes the different operators with Wilson coefficients $c_{1,n}^{(f)}$ which are calculable in short range pertubrbative regime. $v_n^{(f)}$ are the reduced forward matrix elements of the twist-two operators. They are non-perturbative quantities accessible on the lattice and are interpreted as the n-th moments of the momentum fraction carried by quarks (2.4.9)

$$\langle \vec{P}|\mathcal{O}^{(f)}_{\{\mu_1\cdots\mu_n\}} - \text{traces}|\vec{P}\rangle = 2v_n^{(f)}(\mu)[p_{\mu_1}\cdots p_{\mu_n} - \text{traces}]. \tag{4.4.2}$$

For a pion, v_n depends on only the momentum vector p since it is spin-0 particle. Due to isospin invariance, pion matrix elements are simplified by an isospin rotation $u \leftrightarrow d$. We should keep in mind that in Eq. (4.4.1) higher order terms are of order of $1/Q^2$, which in the limit $Q^2 \to \infty$ are negligible.

In the continuum, operators are categorized based on their behavior under the Lorentz transformations and charge conjugation. In Euclidean space-time, the Lorentz group is replaced by the orthogonal group $O(4)$, which on the lattice, because of the discretization of the space-time, reduces to the hypercubic group, $H(4) \subset O(4)$. Hence, lattice operators are classified according to $H(4)$ and charge conjugation. Since $H(4)$ is a finite group, the restriction due to the symmetry are less than in the continuum and possibilities of mixing the operators are increased.

We introduce the continuum operators in chapter 2 (Eq. (2.3.4)). To write down the lattice version of the above operators, one has to replace the continuum covariant derivative by the lattice covariant one [G+96b]

$$\begin{aligned}
\overrightarrow{D}_\mu \psi_x &= \frac{1}{2a}\Big(U_{x,\mu}\psi_{x+\hat{\mu}} - U^\dagger_{x-\hat{\mu},\mu}\psi_{x-\hat{\mu}}\Big), \\
\bar{\psi}_x \overleftarrow{D}_\mu &= \frac{1}{2a}\Big(\bar{\psi}_{x+\hat{\mu}}U^\dagger_{x,\mu} - \bar{\psi}_{x-\hat{\mu}}U^\dagger_{x-\hat{\mu},\mu}\Big)
\end{aligned} \tag{4.4.3}$$

with lattice spacing a and link matrix $U_{x,\mu}$ which were explained in chapter 3. On the lattice operators are not irreducible[4], which allows them to mix with lower-dimensional operators under renormalization. Under charge conjugation, the lattice operators transform as

$$\mathcal{O}_{\mu_1\mu_2\cdots\mu_n} \xrightarrow{\mathcal{C}} (-1)^n \mathcal{O}_{\mu_1\mu_n\mu_{n-1}\cdots\mu_2} \tag{4.4.4}$$

In the OPE in Eq. (4.4.1), $\mathcal{C} = +$ operators contribute [G+96b]. To compare the Euclidean $(1,1,1,1)$ metric with the Minkowski metric $(1,-1,-1,-1)$ and using the

[4] On Hilbert space $\mathcal{H}$, an irreducible operator is an operator with no reducing subspace except $\{0\}$ and $\mathcal{H}$.

Rank	Notation	Operator $\mathcal{O}$	Repr.	$\langle\mathcal{O}\rangle$	C
1	$\mathcal{O}^V_\mu$	$\bar{\psi}\gamma_\mu\psi$	$\tau_1^{(4)}$	$\mathcal{O}^V_1, \mathcal{O}^V_2, \mathcal{O}^V_3, \mathcal{O}^V_4$	-
2	$\mathcal{O}^T_{\mu\nu}$	$\bar{\psi}\sigma_{\mu\nu}\psi$	$\tau_1^{(6)}$	$\mathcal{O}^T_{12}, \mathcal{O}^T_{13}, \mathcal{O}^T_{14}, \mathcal{O}^T_{23}, \mathcal{O}^T_{24}, \mathcal{O}^T_{34}$	-
2	$\mathcal{O}_{\mu\nu} \to \mathcal{O}^{v_{2,a}}$	$\bar{\psi}\gamma_\mu \overleftrightarrow{D}_\nu \psi$	$\tau_3^{(6)}$	$\mathcal{O}_{\{12\}}, \mathcal{O}_{\{13\}}, \mathcal{O}_{\{14\}}, \mathcal{O}_{\{23\}}, \mathcal{O}_{\{24\}}, \mathcal{O}_{\{34\}}$	+
2	$\mathcal{O}_{\mu\nu} \to \mathcal{O}^{v_{2,b}}$	$\bar{\psi}\gamma_\mu \overleftrightarrow{D}_\nu \psi$	$\tau_1^{(3)}$	$\frac{1}{2}(\mathcal{O}_{11}+\mathcal{O}_{22}-\mathcal{O}_{33}-\mathcal{O}_{44})$, $\frac{1}{\sqrt{2}}(\mathcal{O}_{33}-\mathcal{O}_{44})$, $\frac{1}{\sqrt{2}}(\mathcal{O}_{11}-\mathcal{O}_{22})$	+

Table 4.4.1: Operators and their charge conjugation.

Wick rotation at time component, the relation between lattice and continuum operators can be written as

$$\mathcal{O}_M^{\mu_1\mu_2\cdots\mu_n} \to (-1)^{n_4+n_5+1}(-i)^{n_{123}}\mathcal{O}^E_{\mu_1\mu_2\cdots\mu_n} \tag{4.4.5}$$

$$\mathcal{O}_{MT}^{\mu\nu\mu_1\mu_2\cdots\mu_n} \to (-1)^{n_4+n_5+1}(-i)^{n_{123}+1}\mathcal{O}^{ET}_{\mu\nu\mu_1\mu_2\cdots\mu_n} \tag{4.4.6}$$

For a complete explanation of the lattice operators see e.g. [G+96a], [G+96b]. The general form of the first moment operator is

$$\mathcal{O}_{\mu\nu}, \quad 1 \le \mu < \nu \le 4. \tag{4.4.7}$$

All operators which we used in our calculations are listed in Table 4.4.1. Operators are labeled according to the moments of structure functions that they determined. Despite the operators $\mathcal{O}_{v_{2,a}}$ and $\mathcal{O}_{v_{2,b}}$ belong to the same irreducible representation of $O(4)$, they transform according to non-equivalent representations of $H(4)$. Therefore, their lattice renormalization factors are different.

4.4.1 Renormalization of Operators

In discretized space-time, the lattice spacing a provides an ultraviolet cut-off, which corresponds to maximal energy. Therefore, the lattice regularization[5] provides a momentum cut-off $|p| < \Lambda = \frac{\pi}{a}$ to avoid infinities. This cut-off means the momentum integrals are carried out only up to $\mathbf{p}^2 = \Lambda^2$ [KSF01]. By removing the cut-off ($a \to 0$ and so cut-off $\to \infty$) a technique called *renormalization* is used to get the finite results for the physical quantities[6]. We have to renormalize operators and convert them to the scheme of Wilson coefficients, $\overline{\text{MS}}$ scheme.

A renormalized continuum operator can be written as

$$\mathcal{O}_{R,\mu} = Z_{\mathcal{O}}(a\mu, g(a))\mathcal{O}(a) \tag{4.4.8}$$

where $\mathcal{O}(a)$ denotes the bare lattice operator. The renormalization factor $Z_{\mathcal{O}}$ depends on the renormalization scale μ and the coupling constant $g(a)$ which is the one used

[5] Regularization is a method to introduce a regulator to deal with expressions with no physical meanings. The correct physical results is obtained in the limit of (regulator) $\to 0$.

[6] We follow [G+99b] and section 6.6 in [Hor00]

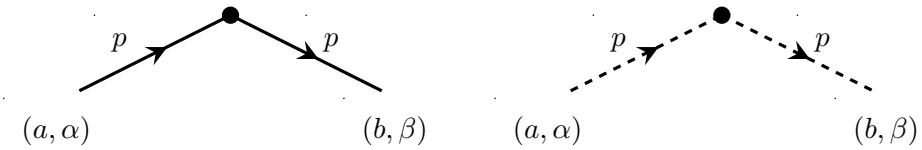

Figure 4.4.1: Left: The Green's function, Eq. (4.4.9). Right: The amputated Green's function, Eq. (4.4.10). Taken from [Hor00].

in the gauge action. The structure functions are independent of any renormalization procedures. Therefore, the μ dependence of operators and Wilson coefficient have to be canceled.

There are different ways to calculate the renormalization constant. For example using the Schrödinger functional (see, e.g., [L+92]). In QCD, because of the asymptotic freedom, the coupling constant is small at high energies and the coefficient functions can be also calculated perturbatively [LM93]. We use a non-perturbative method the so-called the RI-MOM scheme[7] proposed by Martinelli et al. [M+95].

The RI-MOM method works as follows: we start from the non-amputated quark Green function with one operator insertion $\mathcal{O}$ at zero momentum is written as

$$G^{ab}_{\alpha,\beta}(p) = \frac{1}{V}\sum_{x,y,z} e^{-ip.(x-y)}\langle q^a_\alpha(x)\mathcal{O}(z)\bar{q}^b_\beta(y)\rangle \tag{4.4.9}$$

with lattice spacing a and lattice volume V. $G_{\alpha,\beta}$ is a matrix in color and Dirac space. The vertex function (amputated Green function) i.e. removing the external legs is then defined as

$$\Gamma_{\mathcal{O}}(ap, g_0(a)) = S^{-1}(p)G_{\mathcal{O}}(p)S^{-1}(p) \tag{4.4.10}$$

where S is the Fourier transform of the quark propagator in the momentum space after averaging over all configurations $S^{ab}_{\alpha\beta}(p) = 1/V\sum_{x,y} e^{-ip.(x-y)}\langle q^a_\alpha(x)\bar{q}^b_\beta(y)\rangle$. Then the renormalized vertex function can be written as

$$\Gamma_{R,\mathcal{O}}(p) = Z_q^{-1}Z_{\mathcal{O}}\Gamma_{\mathcal{O}}(p). \tag{4.4.11}$$

The renormalization constant $Z_{\mathcal{O}}$ is fixed by imposing the renormalization condition

$$\frac{1}{12}\mathrm{tr}\big(\Gamma_{R,\mathcal{O}}(p)\Gamma_{Born}(p)^{-1}\big)\Big|_{p^2=\mu^2} = 1. \tag{4.4.12}$$

By implementing (4.4.11) we can calculate $Z_{\mathcal{O}}$

$$\frac{1}{12}Z_q^{-1}Z_{\mathcal{O}}\mathrm{tr}\big(\Gamma_{\mathcal{O}}(p)\Gamma_{Born}(p)^{-1}\big) = 1. \tag{4.4.13}$$

[7] RI means this method is regularization independent and MOM stands for momentum subtraction. This renormalization condition is imposed in momentum space and follows the formulation in continuum calculations.

Here, the $\Gamma_{Born}(p)$ is the Born term, the tree level expression of the operator on the lattice. The quark field renormalization constant $q_R(x) = \sqrt{Z_q}q(x)$ is obtained form the quark propagator directly [Sch98]

$$Z_q(ap, g_0(a)) = \left.\frac{\mathrm{tr}(-i\sum_\lambda \gamma_\lambda \sin(ap_\lambda) a S^{-1}(p))}{12\sum_\lambda \sin^2(ap_\lambda)}\right|_{p^2=\mu^2}. \tag{4.4.14}$$

Our renormalization constants are defined at the scale $\mu^2 = p^2$. In the above equations, the trace means that Z depends on the index structure of the operators $(\mu_1, \cdots, \mu_n)$ and on the direction of the chosen scale p_μ. The renormalization scale μ has to be low enough to have small lattice effects but also large enough to have no non-perturbative effects

$$\frac{1}{L^2} \ll \Lambda^2_{QCD} \ll \mu^2 \ll \frac{1}{a^2} \tag{4.4.15}$$

where $L = N/a$ is the extent of the lattice. In order to compare lattice results with phenomenology values our data in the RI-MOM scheme at scale μ has to be translated to the $\overline{\mathsf{MS}}$ scheme at the reference scale. For this we use the corresponding perturbative Z-factors that relate the operators in the RI-MOM scheme to the $\overline{\mathsf{MS}}$ scheme.

In practice we first translate RI-MOM scheme to renormalization group invariant scheme, RGI, which depends on the coupling and is independent of scale and then to the $\overline{\mathsf{MS}}$ scheme at scale μ [G$^+$10]

$$\mathcal{O}_R^{\overline{MS}}(\mu) = Z^{RGI\to\overline{MS}}(\mu, \mathcal{O})\, Z^{RGI}(g, \mathcal{O})\, \mathcal{O}_{bare}. \tag{4.4.16}$$

The conversion factors to the $\overline{\mathsf{MS}}$ scheme used in this work are taken from [Göc13].

Chapter 5

Results for Two-point function

In this chapter we report our results for the pion two-point functions using the meson operators introduced in chapter 4. Since the pion mass is required for almost all lattice simulations we will start with a discussion of meson correlation functions and how to extract the energy, respective the mass of the pion.

5.1 Two-Point Functions

We explained how to calculate the pion two-point functions using the pion interpolating fields in Eq (4.1.28). In general, meson correlators can be

$$C(t) = \sum_n Z_n e^{-E_n t}. \tag{5.1.1}$$

The steepness of the exponential fall-off is given by the energies E_n of the different states n with the amplitudes Z_n. Since mesons propagate forward in time and anti-mesons move backward, and both have the same mass and energy, Eq. (5.1.1) changes to

$$C(t) = Z_0(e^{-E_0 t} \pm e^{-E_0(T-t)}) + Z_1(e^{-E_1 t} \pm e^{-E_1(T-t)}) + \cdots \tag{5.1.2}$$

where $\pm$ denotes the choice of the source and sink operators, and T is the lattice extent in time direction. It is obvious that for large t, higher states are exponentially suppressed. However, for small t, the mixing of ground and excited states are not negligible.

When only the ground state is considered, the two-point function is a single cosh function. It can be written as

$$Z_0(e^{-E_0 t} + e^{-E_0(T-t)}) = 2Z_0\, e^{-TE_0/2} \cosh((T/2 - t)E_0). \tag{5.1.3}$$

Fig 5.1.1 shows as an example of lattice data for $C(t)$ as a function of time at a fixed lattice spacing $a = 0.0714$ fm. The data is from three different Monte Carlo simulations with hopping parameters $\kappa = 0.13640$, 0.13632 and 0.13620 which indicate three different pion masses. For the y–axis, we have used a logarithmic scale to better illustrate that, in fact, the leading behavior is due to the single exponential behavior

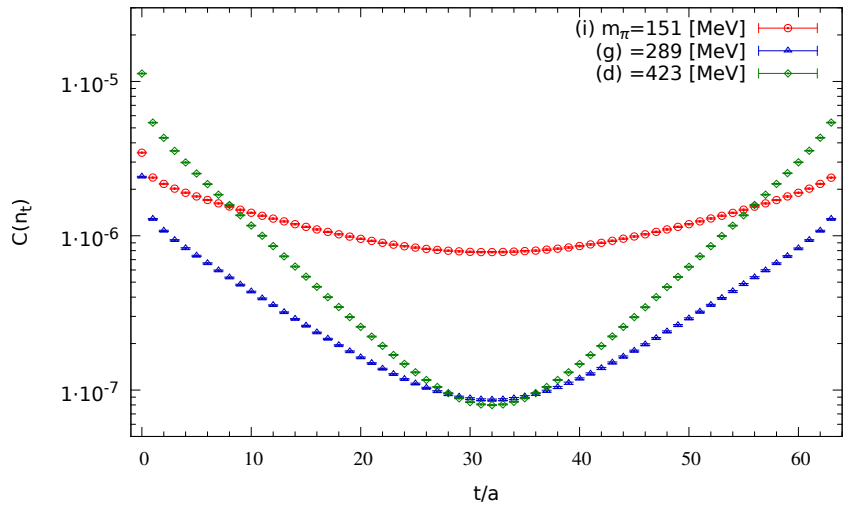

Figure 5.1.1: Pion two point functions at vanishing momentum $p = 0$ at fixed lattice spacing $a = 0.0714$ fm for sets $(d), (g)$ and (i) (Table 6.2.1). Pion masses are increased from 151 MeV to 427 MeV.

of the ground state (see the almost linear dependence at large t). One nicely sees that larger slopes of $C_{2pt}(t)$ indicate the larger pion mass values, and the y-intercepts which give the amplitudes (Z). The statistical errors are determined via the jackknife method (see Appendix C).

From Eq. (5.1.2) it is clear that two-point functions are symmetric around $T/2$. We utilize that by applying the folding method which is averaging over elements from the forward propagator and the backward propagator. Note that we apply anti-periodic boundary condition in time direction. Therefore, the data at time slice 0 is consistent with that at the lattice time extent T. This method is shown schematically in Fig. 5.1.2. Note that we start the counting from 0. It is illustrated which points are averaged and arrows show the propagating directions.

For the calculation of the pion mass, Eq. (5.1.3) is used as a general starting point. We will come back to this in section 5.1.2.

5.1.1 The Calculation of Excited State Energy

The energy-momentum relation of (relativistic) particles is given by the dispersion relation

$$E^2 = \vec{p}^2 + m^2. \tag{5.1.4}$$

At zero momentum, where $\vec{p}^2 = 0$ and hence $E^2 = m^2$, the correlation function for a forward propagating pion can be parametrized as

$$C_{2pt} = Z_0 e^{-m_0 t} + Z_1 e^{-m_1 t} + \cdots \tag{5.1.5}$$

where $m_1 = m_0 + \Delta m$ and Δm is the mass gap between the ground state and the first excited state. A similar expression can be written for the backward propagating pion.

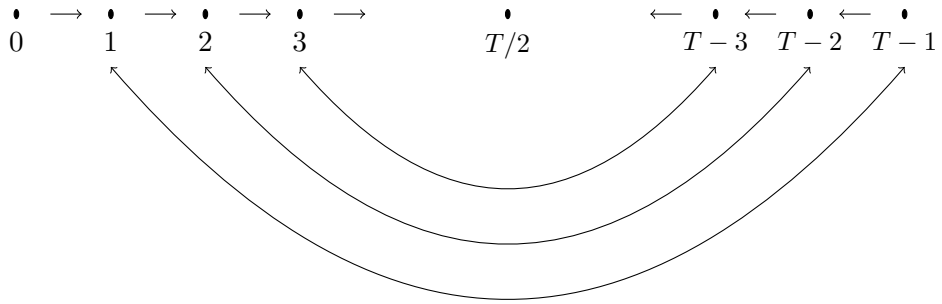

Figure 5.1.2: Schematic description of the folding method.

We saw in Fig. 5.1.1 the leading behavior of $C_{2pt}(t)$ is given by the ground state, but at small time slices there are discrepancies to this single exponential behavior. Thus fitting the data to the following analytic function

$$C_{2pt} = e^{-m_0 t}(Z_0 + Z_1 e^{-\Delta m t}) + e^{-m_0(T-t)}(Z_0 + Z_1 e^{-\Delta m(T-t)}) \tag{5.1.6}$$

give us Δm. This ansatz will result in a much better fit to the data.

To demonstrate this, we fit our folded data twice; one without considering the contribution from the first excited state. Second time, we consider the first excited state contaminations and use the combined fit. The upper frames of Fig. 5.1.3 show two such fit examples, left frame for the ensembles $\beta = 5.29,\ \kappa = 0.13632$, with volume $40^3 \times 64$ and right $\beta = 5.40,\ \kappa = 0.13640$, with volume $32^3 \times 64$. The symbols denote our data for C_{2pt}, the red line is a fit to the ground state, Eq. (5.1.3) and blue line denotes the fit to the ground-plus-first-excited state, Eq. (5.1.6).

The lower frames of Fig. 5.1.3 show the deviation of the ground state energy from ground-plus-first-excited state. The red squares show C_{2pt} divided by a fit to ground state and the blue circles are data divided by ground and first excited state. When there was no excited state contaminations, one should have 1 for $C_{2pt/fit}$. However, at small t/a there exists a discrepancy between the data and the fit to the ground state and also to our fit of the ground-plus-first-excited state. Our combined fit results are listed in Table 5.1.1.

5.1.2 Effective Mass

The effective mass is a popular method to extract the mass of a particle. This method is given by the steepness of a correlator as a numerical derivative and is defined at each distance t/a as

$$am_{eff}(t/a + \frac{1}{2}) = \log\Big[\frac{C(t/a)}{C(t/a+1)}\Big]. \tag{5.1.7}$$

When the ground state energy dominates, the effective mass m_{eff} shows a plateau. The starting point and length of the plateau depend on the interpolating fields. The

	β	κ	volume	$a\,[fm]$	m_0	m_1	$\frac{Z_0}{Z_1}$
(e)	5.29	0.13632	$32^3 \times 64$	0.0714	0.10683 (10)	0.86316 (1378)	2.870
(f)			$40^3 \times 64$		0.10468 (2)	0.7078 (124)	3.429
(g)			$64^3 \times 64$		0.10457 (7)	0.6284 (410)	4.296
(i)	5.29	0.13640	$64^3 \times 64$		0.05426 (3)	0.7845 (917)	4.120
(j)	5.40	0.13640	$32^3 \times 64$	0.0604	0.15048 (5)	0.6537 (470)	3.175

Table 5.1.1: Parameters of combined fits of the two-point functions data using Eq. (5.1.3) and (5.1.6) as fitting function.

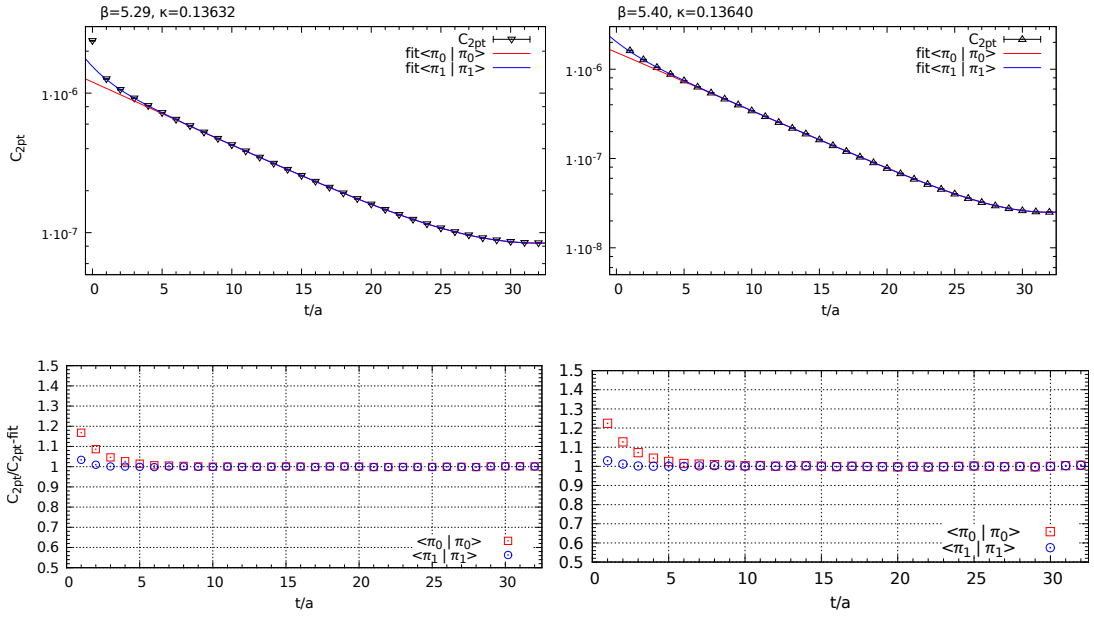

Figure 5.1.3: Top: Symbols are two-point function data after folding. The red line is a fit of C_{2pt} ignoring excited states. The blue line is a fit of ground and first excited state to the data from simulations (e) (left) and (j) (right) from Table 6.2.1. Bottom: same data and fit but shown as ratio $C_{2pt/fit}$. Again, the red squares are for a fit to the ground state and the blue circles are for a fit to ground and first excited state.

hadron mass is then extracted from a fit to the correlation data Eq. (5.1.1) in the plateau area. There exists no a priori rules to choose a proper fit range but there are some guidelines. The best is to consider a fixed point $T/4$ in forward propagating and $3T/4$ in backward. Then verify the neighboring data points around it to get the fit stabilized at one state. To the respect of periodicity in t/a regarding Eq. (5.1.3) for symmetric correlators, one sets

$$\frac{C(t/a)}{C(t/a+1)} = \frac{\cosh\left(m_{eff}(t-T/2)\right)}{\cosh\left(m_{eff}(t+a-T/2)\right)} \tag{5.1.8}$$

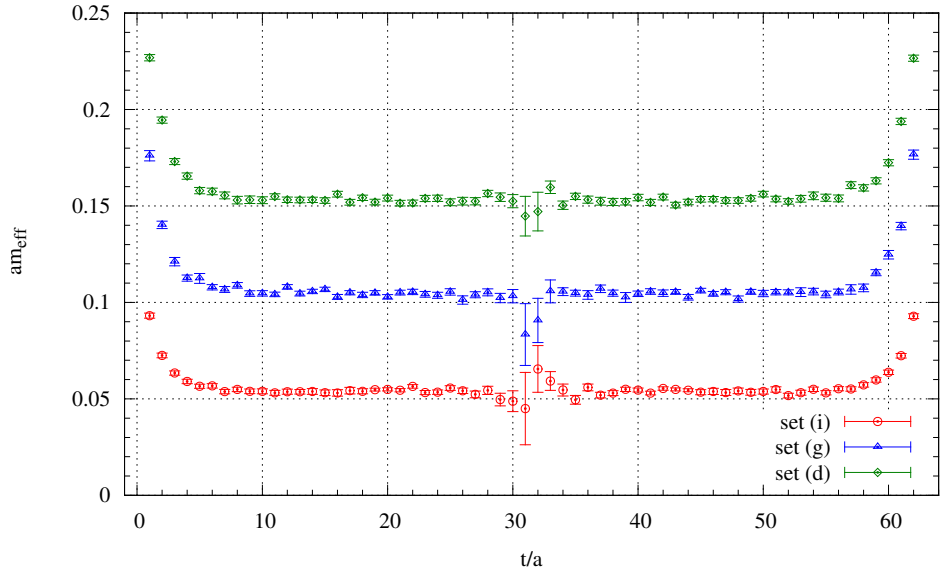

Figure 5.1.4: Effective masses derived from Eq. (5.1.8) correspond to the same different sets shown in Fig. 5.1.1.

and solves the equation with respect to m_{eff} at each time slice. Fig. 5.1.4 shows the result of this symmetrization applied to the same sets of correlations shown in Fig. 5.1.1. It illustrates that at time slices $t/a < 6$ (and equivalently $t/a > 59$) excited states contribute to the energy. The plateau is noticeable for region $8 < t/a < 24$ and $40 < t/a < 52$ for forward and backward propagating, respectively, where contributions of excited states energy are almost absent. For a suitable interval, the energy can be read from the m_{eff} where $p^2 = 0$. Thus two fitting parameters Z_0 and E_0 in Eq. (5.1.1) are extracted from fit to the data.

5.1.3 Smearing

In section 4.2 we mentioned that in order to smooth out the ultraviolet fluctuations, a smearing method is used. This method is employed on the quark fields of the interpolating operators to have a better overlap with the physical ground state. We examined different types of quark smearing (Wuppertal and Jacobi). Comparison of different smearing recipes for one simulation with $\beta = 5.40$ and $\kappa = 0.13640$ with lattice volume $32^3 \times 64$ is shown in Fig. 5.1.5. It is interesting to note that the correlation function with APE smeared gauge links shows a significantly better slope to extract the mass than without the link smearing (the dotted red line). We verified the number of smearing sweeps of the quark smearing to achieve the best signal. The dependence of the number is more remarkable between the dashed navy line (75 sweeps) and the dashed-dotted green line (225 sweeps).

Also we have varied Wuppertal steps smearing for quark smearing with APE smearing gauge link. We chose #161 configurations for one set of simulation, with $\beta = 5.29$, $\kappa = 0.13640$ with lattice volume $64^3 \times 64$, corresponding to the pion mass of $m_\pi =$

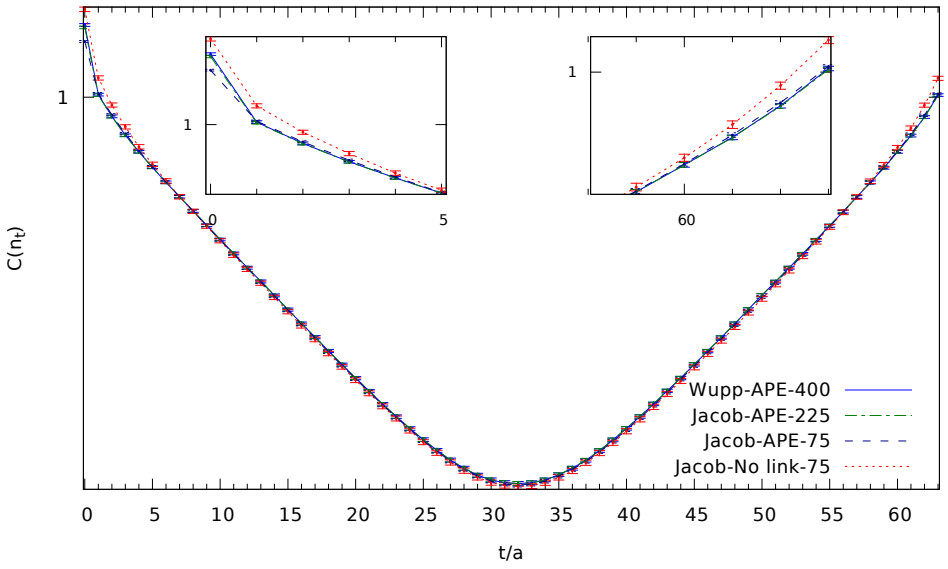

Figure 5.1.5: Two-point function for different types of smearing but same lattice parameters for simulation (j)(Table 6.2.1).

151 MeV. The left frame of Fig. 5.1.6 shows two-point functions and the right frame shows the corresponding effective masses. Comparing the effective mass uncertainties leads us to choose the number of smearing steps to equal #400. Note that too much smearing may destroy the short range physics [Dur07].

Consequently for our calculations, we used the Wuppertal smearing procedure with 400 smearing steps and APE smeared links.

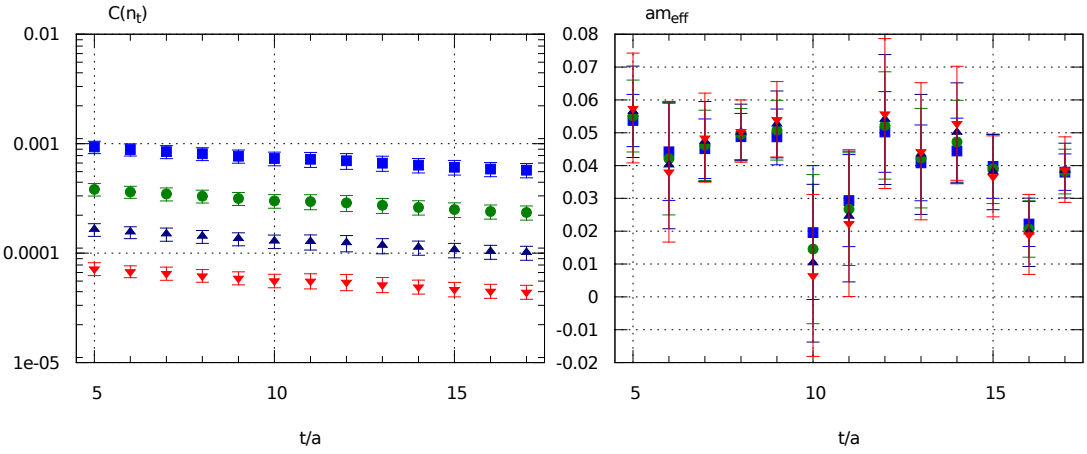

Figure 5.1.6: Left: C_{2pt} for #300 (blue square), #400 (green circle), #500 (navy triangle up) and #600 (red triangle down) sweeps of Wuppertal smearing. Left: Corresponding effective masses.

5.1.4 Finite Momenta

Extracting the pion energy $E_\pi(\vec{p})$ proceeds the same way as extracting meson masses for $(ap)^2 = 0$. In order to extract the energy, we can average over all possible permutation of momenta in different directions but with the same magnitude $|\vec{p}|$. On the lattice with periodic boundary conditions in spatial directions, a momentum $\vec{p} = (p_x, p_y, p_z)$ is quantized in the unit of $2\pi a/L$. They take the following values

$$\begin{aligned}
(ap)^2 &= 0 \quad (0,0,0) \\
(ap)^2 &= 1 \quad (\pm1,0,0),(0,\pm1,0),(0,0,\pm1) \\
(ap)^2 &= 2 \quad (\pm1,\pm1,0),(\pm1,0,\pm1),(0,\pm1,\pm1) \\
(ap)^2 &= 3 \quad (\pm1,\pm1,\pm1) \\
(ap)^2 &= 4 \quad (\pm2,0,0),\ldots \\
(ap)^2 &= 5 \quad (\pm2,\pm1,0),\ldots \\
(ap)^2 &= 6 \quad (\pm2,\pm1,\pm1),\ldots .
\end{aligned} \tag{5.1.9}$$

In order to extract the energy from the lattice data, one fits the cosh-ansatz in Eq. (5.1.8) to data at different momenta. The left frame of Fig. 5.1.7 shows two-point function for one ensemble with $\beta = 5.29$, $\kappa = 0.13632$, and volume $40^3 \times 64$. It illustrates that by increasing the momenta (top to bottom) the statistical noise increases in the middle of the lattice and fitting to the effective mass (right frame of Fig. 5.1.7) does not provide a good result. The energies extracted from the data can not be used in our analysis and we use the energies calculated from the dispersion relation

$$E_\pi^2 = \vec{p}^2 + m_\pi^2 \tag{5.1.10}$$

to compute the matrix element Eq. (4.1.9).

Fig. 5.1.8 shows the discrepancy between the energies from dispersion relation and fitting data for two samples $\beta = 5.20$, $am_\pi = 0.11528$, $a = 0.0813\,\text{fm}$ (left frame) and $\beta = 5.29$, $am_\pi = 0.10475$, $a = 0.0714\,\text{fm}$ (right frame). Symbols for the squared energies are extracted from fitting the lattice data versus the momentum squared $|p|^2$ while for the dashed lines the corresponding energies are calculated from continuum dispersion relation Eq. (5.1.10). The samples are chosen for two different lattice spacing. As it is illustrated, discrepancies between the energies for bigger lattice spacing is larger. The results of fitting lattice data for momenta up to $(ap)^2 = 4$ are shown in Table 5.1.2.

5.1.5 Finite Size Effect

On the lattice, besides excited state contaminations, the finite lattice spacing a and the finite volume $(L^3 \times T)$ are another source of systematic errors to compute hadron masses. In most studies, the time direction is sufficiently larger than the spatial directions, so the excited state contributions in correlation function $C(t) = \sum_n Z_n e^{-E_n t}$ are small. Therefore, the leading finite size effects are due to the spatial volume.

The Fig. 5.1.9 shows a comparison of $C_{2pt}(t)$ data for the same lattice spacing $a = 0.0714\,\text{fm}$, with $\beta = 5.29$ and $\kappa = 0.13632$ but different lattice volumes $32^3 \times 64$, $40^3 \times 64$ and $64^3 \times 64$. We see the deviation around $T/2$ due to the finite volume effect.

(f) $\beta = 5.29$, $\kappa = 0.13632$, volume $= 40^3 \times 64$, $a = 0.0714$ [fm]

$\langle\pi(p')\|\pi_(p)\rangle_{(ap)^2=0}$	$E_0 = 0.10468\,(2)$
$\langle\pi(p')\|\pi_(p)\rangle_{(ap)^2=1}$	$E_0' = 0.18912\,(88)$
$\langle\pi(p')\|\pi_(p)\rangle_{(ap)^2=2}$	$E_0'' = 0.23989\,(170)$
$\langle\pi(p')\|\pi_(p)\rangle_{(ap)^2=3}$	$E_0''' = 0.30303\,(240)$
$\langle\pi(p')\|\pi_(p)\rangle_{(ap)^2=4}$	$E_0'''' = 0.32332\,(803)$

(a) $\beta = 5.20$, $\kappa = 0.13596$, volume $= 32^3 \times 64$, $a = 0.0813$ [fm]

$\langle\pi(p')\|\pi_(p)\rangle_{(ap)^2=0}$	$E_0 = 0.11549\,(8)$
$\langle\pi(p')\|\pi_(p)\rangle_{(ap)^2=1}$	$E_0' = 0.22700\,(85)$
$\langle\pi(p')\|\pi_(p)\rangle_{(ap)^2=2}$	$E_0'' = 0.30089\,(423)$
$\langle\pi(p')\|\pi_(p)\rangle_{(ap)^2=3}$	$E_0''' = 0.34709\,(920)$
$\langle\pi(p')\|\pi_(p)\rangle_{(ap)^2=4}$	$E_0'''' = 0.39959\,(1908)$

Table 5.1.2: The energies from fitting $C_{2pt}(t)$ in zero and higher momentum transfer up to $(ap)^2 = 4$.

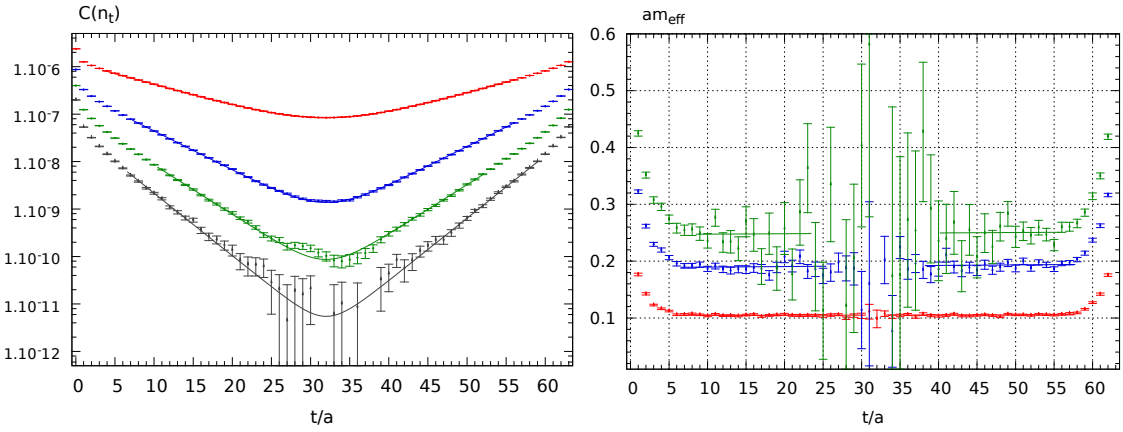

Figure 5.1.7: Left: $C_{2pt}(t)$ for vanishing and non-vanishing momentum transfer for set (f)(Table 6.2.1). From the top to the bottom $p^2 = 0$, $p^2 = 1$, $p^2 = 2$, $p^2 = 3$. Right: compatible effective mass for same data sets. Since the correlation function at $p^2 = 3$ is noisy, the corresponding effective mass has not been shown.

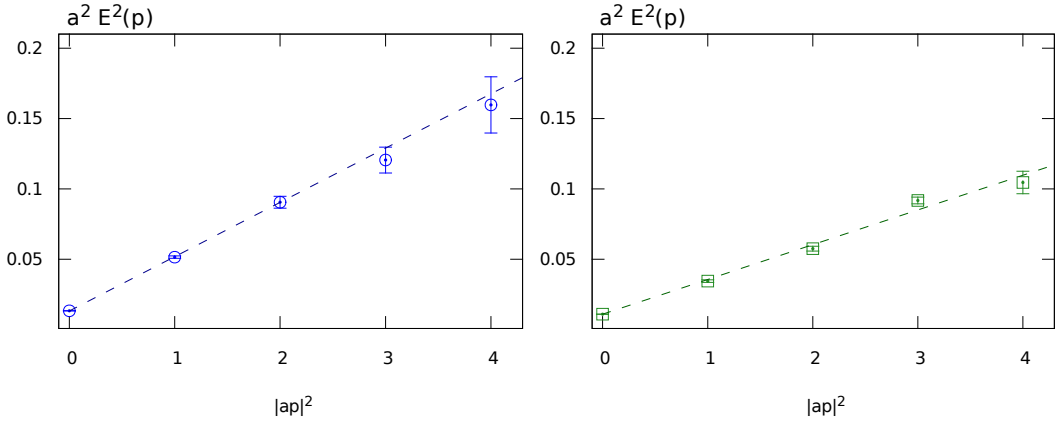

Figure 5.1.8: Pion energy squared in lattice unit $(aE)^2_\pi(p)$ for two different lattice spacing, left: $a = 0.0813\,[\mathrm{fm}]$, right: $a = 0.0714\,[\mathrm{fm}]$ against the momenta. Symbols are fitted values from effective masses and dashed line is energy from dispersion relation.

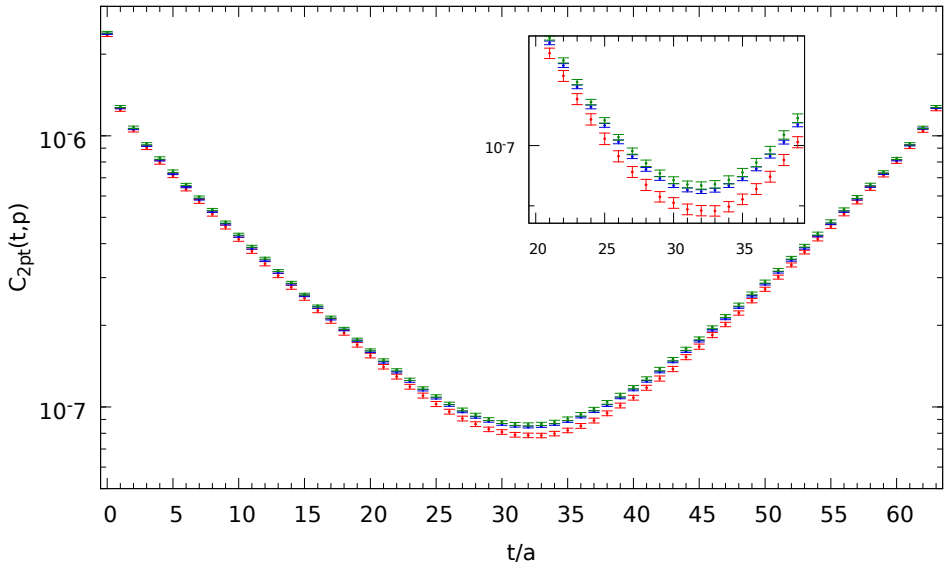

Figure 5.1.9: Pion $C_{2pt}(t)$ at $\vec{p}^2 = 0$ for 3 simulations with same hopping parameter $\kappa = 0.13632$ and lattice spacing $a = 0.0714$ ($\beta = 5.29$) but different volumes $32^3 \times 64$ (red), $40^3 \times 64$ (blue), $64^3 \times 64$ (green). Finite size effect close to the middle of lattice is obvious.

Fig. 5.1.10 shows the corresponding effective masses. By fitting the effective mass, one sees the smaller volume produces the larger slope and so the larger m_π. Volume dependence of the pion mass is shown in Fig. 5.1.11. One clearly sees that the spatial lattice volume has an impact for $L < 2.8$ fm.

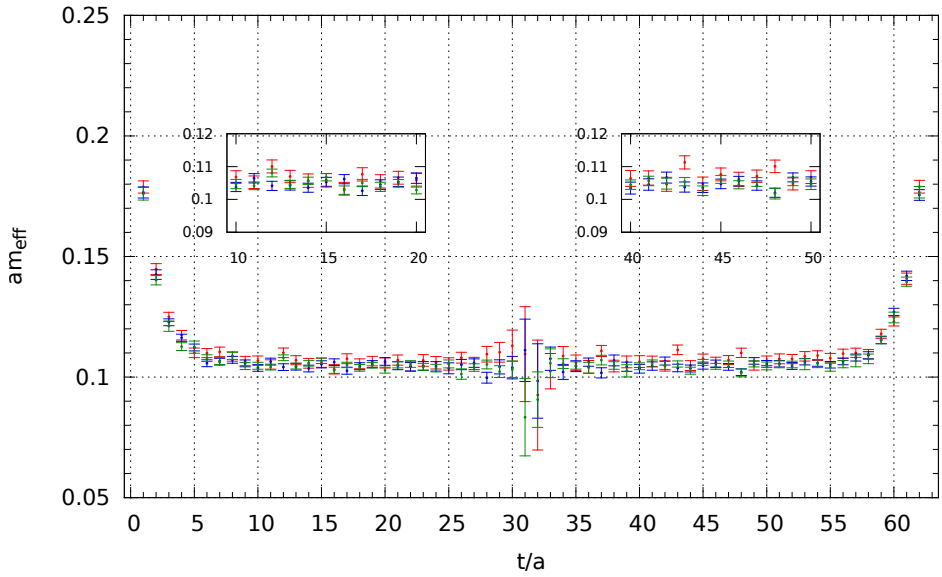

Figure 5.1.10: Effective masses for same ensembles as Fig. 5.1.9.

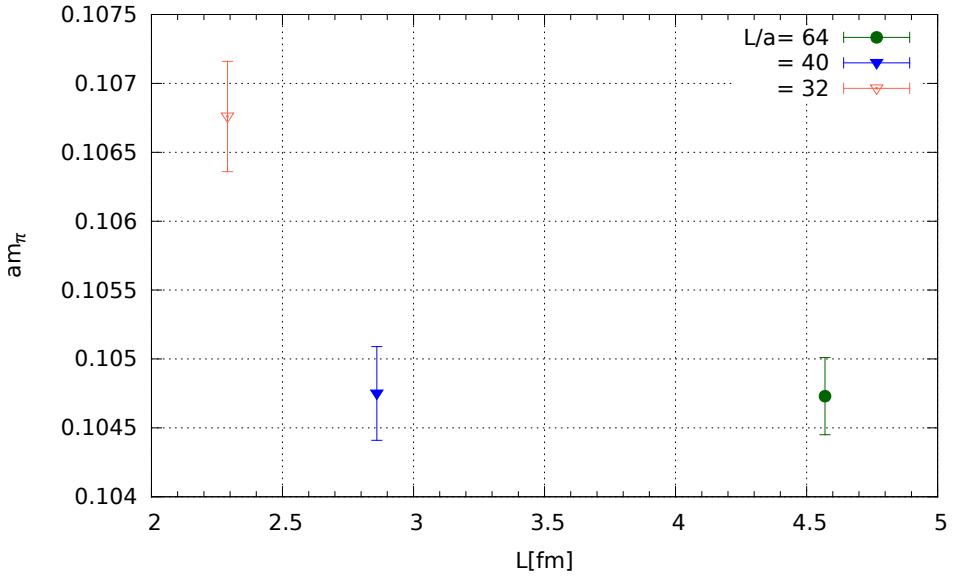

Figure 5.1.11: Pion masses in lattice units as a function of spatial lattice size L.

Chapter 6

Pion Parton Distribution Function

Generalized Parton Distributions are relatively new theoretical tools for the study of internal structure of hadrons. In the forward limit, i.e. vanishing momentum transfer, GPDs connect to the traditional parton distributions which encode the probability of finding a parton inside a hadron with the momentum fraction x of the target. The framework of lattice QCD allows us to calculate moments of parton distribution functions.

In this chapter, we first introduce the techniques needed to extract the forward $p = p'$ and off-forward $p \neq p'$ matrix elements on the lattice and show our results. We then give a brief overview on previous calculations of moments of PDFs in the quenched approximation and results derived from forward scattering employing model calculations. At the end our results will be compared to them.

6.1 Lattice calculations

In chapter 4 we discussed the lattice techniques to calculate two- and three-point functions. They are the main building blocks for the calculation of the matrix elements that relate to the desired moments of PDFs. In order to compute the matrix elements, one option is to fit the time dependence of the two-point function, Eq. (5.1.3) and three-point function, Eq. (4.3.4). From the two-point functions we extract the energies $E(\vec{p}), E(\vec{p}'), \ldots$ and amplitudes $Z(p), Z(p'), \ldots$. These values are then used in Eq. (4.3.12) to obtain the relevant matrix elements from a fit to the three-point functions data.

Another way is to construct ratios of the three- and two-point functions where those common factors relevant to normalization cancel each other and moreover, reduce statistical fluctuations. This is because the data for the two- and three-point functions are correlated and by performing the jackknife analysis this is taken care of. To this end, different type of ratios have been used (see e.g. [H$^+$07, W$^+$92, B$^+$07b]). We use

the ratio

$$R(t_{sink},\tau,p',p)=\frac{C^{\mathcal{O}}_{3pt}(\tau,\vec{p}',\vec{p})}{C_{2pt}(t_{sink},\vec{p})}\sqrt{\frac{C_{2pt}(t_{sink}-\tau,\vec{p})C_{2pt}(\tau,\vec{p}')C_{2pt}(t_{sink},\vec{p}')}{C_{2pt}(t_{sink}-\tau,\vec{p}')C_{2pt}(\tau,\vec{p})C_{2pt}(t_{sink},\vec{p})}}\,. \tag{6.1.1}$$

Here, $C^{\mathcal{O}}_{3pt}(\tau,\vec{p}',\vec{p})$ refers to a pion three-point function. The source is set at 0 and the current insertion $\mathcal{O}$ is set at τ, as explained in chapter 4. $C_{2pt}(t,\vec{p})$ denotes the pion two-point function with a pion creation operator at the Euclidean time $t_1=0$ and an annihilation operator at $t_2=t_1+t$, as explained in chapter 5. In Eq. (6.1.1) only the quark line connected part of the three-point functions is considered. Eq. (6.1.1) holds for all momenta $\vec{p}$ and $\vec{p}'$, but we will see that for large $|\vec{p}-\vec{p}'|$ the statistical noise increases. Therefore, for off-forward matrix elements, we limit the number of sink momenta $\vec{p}'$ to avoid additional inversions of the Dirac operator. To compute the connected contributions, with the conventional sequential source technique, t_{sink} is fixed and one adds the three point functions over the operator varying insertion time τ.

In the forward limit, $|p|=|p'|$, the momentum transfer $Q^2=(p-p')^2$ is zero. In Eq. (6.1.1) the square root therefore reduces to one and the ratio simplifies to

$$R(t_{sink},\tau,p,p)=\frac{C^{\mathcal{O}}_{3pt}(\tau,\vec{p},\vec{p})}{C_{2pt}(t_{sink},\vec{p})}. \tag{6.1.2}$$

Inserting the time dependence of two-point (5.1.3) and three-point function (4.3.12) into the ratio, Eq. (6.1.1) yields to

$$\begin{aligned}R(t_{sink},\tau,p,p)&=\frac{\sqrt{Z(p)Z(p)}e^{-(t_{sink}-\tau)E(p)-\tau E(p)}}{Z(p)\left(e^{-E(p)t_{sink}}+e^{-E(p)(T-t_{sink})}\right)}\langle\pi^+(p)|\mathcal{O}(\tau)|\pi^+(p)\rangle\\&=\frac{e^{-E(p)t_{sink}}}{e^{-E(p)t_{sink}}+e^{-E(p)(T-t_{sink})}}\langle\pi^+(p)|\mathcal{O}(\tau)|\pi^+(p)\rangle.\end{aligned} \tag{6.1.3}$$

Since for the pion we have a chance to go far away from the sink and still get a good signal, it is practicable to set the sink in the middle of the lattice, $t_{sink}=T/2$ (T is the lattice extend in time direction). Then, Eq. (6.1.2) simplifies to

$$R(t_{sink},\tau,p,p)=\frac{\langle\pi^+(p)|\mathcal{O}(\tau)|\pi^+(p)\rangle}{2}. \tag{6.1.4}$$

This has the further advantage that excited state contaminations, which are not take care of here, are maximally reduced.

6.2 Details of the Simulations

For the numerical evaluation we employ unquenched gauge configurations which were generated with the contribution of $N_f=2$ Sheikholeslami-Wohlert fermions by the Regensburg group and QCDSF Collaboration [B+13]. For each set of parameters, we have analyzed more than 1000 gauge configurations and on each configuration, data was taken for two, three or four sources per configuration. The way to choose source

positions is as follows; the first source per configuration is picked up at a random space-time position and the remaining ones are placed with maximal distance between them to reduce autocorrelations.

The parameters for our simulations are listed in Table 6.2.1. We use the Sommer parameter [Som94] with $r_0 = 0.50\,\text{fm}$ [B$^+$13] to give lattice data a physical scale (see section 3.5). We use the same smearing, Wuppertal smearing with APE smeared gauge links, in both two- and three-point functions. Multiple measurements of two- and three-point functions were performed on each configuration of each ensemble. The data sets cover a large range of quark masses with three lattice spacings. Since the inversion of the Dirac operators is numerically expensive for closer to the physical value, there is no data directly at the physical point, where the pion mass is roughly $m_\pi = 140\,\text{MeV}$. However, we were able to generate configurations for pion masses as low as $m_\pi = 151$ MeV and to accumulate there also sufficient data for the two- and three-point functions which allows us to extrapolate to $m_\pi = 140\,\text{MeV}$.

Errors are computed with the jackknife method (see Appendix C). Since the configurations are made in a sequence, the results on neighboring configurations in a sequence may be correlated. To figure out the correlations, one statistical technique is binning. In this method one averages neighboring results and then recalculate the statistical error. If the results are correlated, the statistical error grows with the bin size and so the binned results are used.

In our simulations, there are some ensembles which satisfy $m_\pi L \geq 4$, so the finite size effects can be expected to be small. This will be discussed in section 6.3.3.

The operators have to be renormalized. The relevant renormalization constants for Z^{RGI} and factors for converting Z^{RGI} to the $\overline{\text{MS}}$ scheme in scale $\mu^2 = 4\,\text{GeV}^2$ are listed in Table. 6.2.2.

Results of Ratio

In order to determine momentums of PDFs, the expectation values of the traceless operators with 2 indices

$$\hat{\mathcal{O}}_{\mu\nu} - \text{trace}, \quad 1 \leq \mu < \nu \leq 4 \tag{6.2.1}$$

are calculated. Due to the symmetrization the 16 components are reduces down to 9, and these 9 independent elements agree with the two representations $\hat{\mathcal{O}}_{v2b}$ and $\hat{\mathcal{O}}_{v2a}$ (see Table 4.4.1). Since in our simulations we set the sink momentum to zero, it is not possible to calculate the expectation value of $\hat{\mathcal{O}}_{v2a}$ in the forward limit. Therefore, $\hat{\mathcal{O}}_{v2a}$ has no contribution to the first moment of the pion PDF.

An example for the ratio of the operator $\hat{\mathcal{O}}_{v2b}$ in the forward limit is illustrated in Fig. 6.2.1. The upper frame of Fig. 6.2.1 shows that at large $t_{sink} \gg \tau$, ratios saturate to a constant which is determined by a fit over several τ. It is a fit to the central points on each side to get the best plateau. Note that the symbol colors are chosen according to the pion mass: red open circles are for data for the lightest pion mass ($m_\pi \approx 151\,\text{MeV}$), blue open squares and triangles for the second lightest mass ($m_\pi \approx 260 - 290\,\text{MeV}$) and green full squares for pion masses above 400 MeV.

Due to the symmetry of the pion two- and three-point functions, we can average over the ones from the forward half of the lattice, $0 < t < T/2$ with a suitable replacement

	κ	Volume	#cfg $\times$ M	m_π [MeV]	$m_\pi L$	t_{sink}/a
	$\beta = 5.20$, $a = 0.0813$ [fm], $a^{-1} = 2427$ [MeV]					
(a)	0.13596	$32^3 \times 64$	1999×4	280	3.69	32
	$\beta = 5.29$, $a = 0.0714$ [fm], $a^{-1} = 2764$ [MeV]					
(b)	0.13590	$24^3 \times 48$	1259×2	662	5.74	24
(c)	0.13620	$24^3 \times 48$	1170×2	428	3.71	24
(d)		$32^3 \times 64$	2000×2	423	4.89	32
(e)	0.13632	$32^3 \times 64$	2023×2	295	3.42	32
(e′)			1063×1			15
(f)		$40^3 \times 64$	2028×2	290	4.19	32
(g)		$64^3 \times 64$	1237×2	289	6.70	32
(h)	0.13640	$48^3 \times 64$	722×2	160	2.77	32
(i)		$64^3 \times 64$	1599×3	151	3.49	32
	$\beta = 5.40$, $a = 0.0604$ [fm], $a^{-1} = 3270$ [MeV]					
(j)	0.13640	$32^3 \times 64$	1124×2	491	4.8	32
(k)	0.13647	$32^3 \times 64$	2000×2	427	4.18	32
(l)	0.13660	$48^3 \times 64$	2178×2	261	3.82	32

Table 6.2.1: Parameters for our lattice calculations [B+14b]. M is the number of sources per configuration; the sink-source separation is $t_{sink} = T/2$. m_π lists the pion mass in MeV for given lattice.

Oper.	Z^{RGI}	$Z^{RGI \to \overline{MS}}$
$\mathcal{O}_V$	0.7364 (55)	1
$\mathcal{O}_{v2a}$	1.504 (12)	0.74027
$\mathcal{O}_{v2b}$	1.509 (23)	0.74027

Table 6.2.2: Renormalization factors for our lattice operators with $\beta = 5.29$. The renormalization scale for $Z^{RGI \to \overline{MS}}$ is $\mu = 2\,\text{GeV}$. Values are taken from [Göc13].

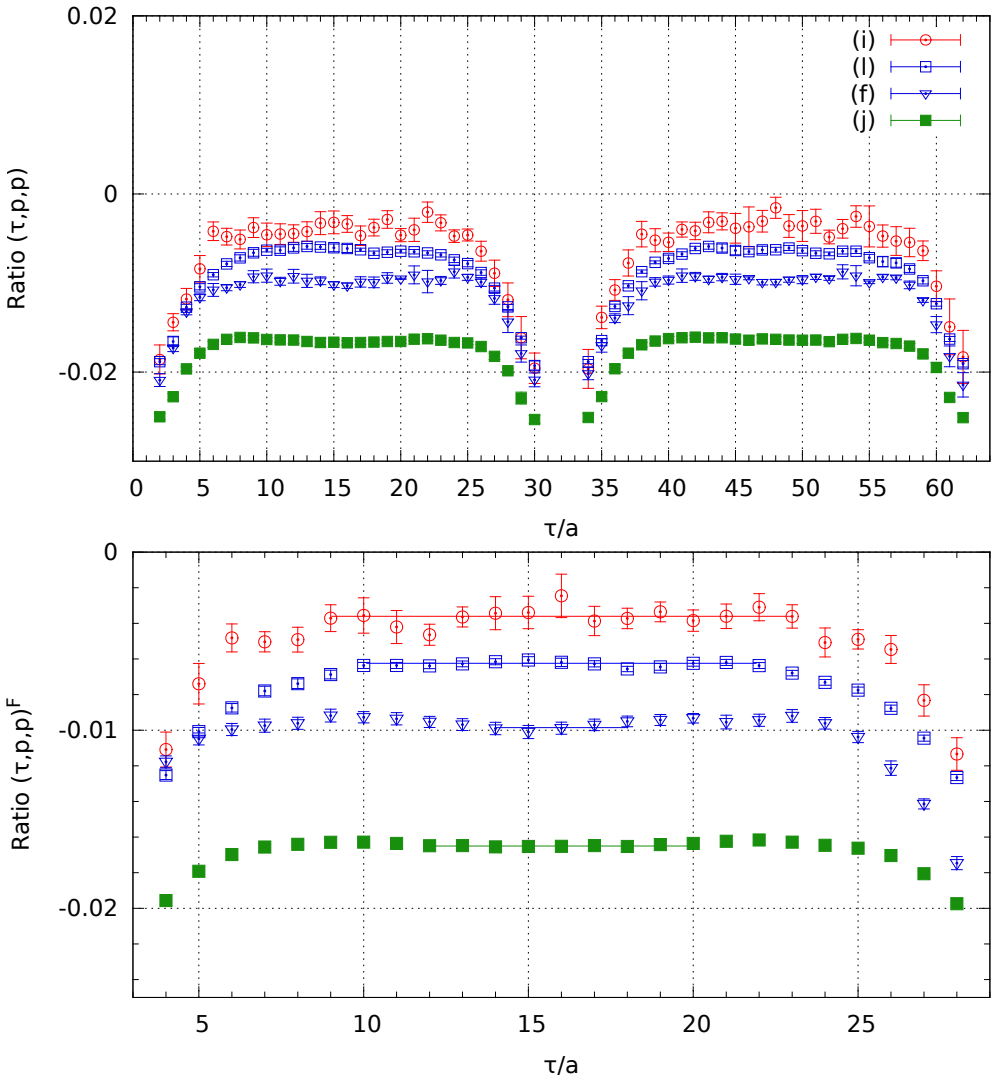

Figure 6.2.1: Top: the ratios $R(\tau, p, p)$ at sink-source separation $T/2$ for the operator $O^{(\vec{p}=0)}_{v_{2,b}}$ for different pion masses (red open circles $am_\pi = 0.05449$, blue open squares $am_\pi = 0.07968$, blue open triangles $am_\pi = 0.10475$, green full squares $am_\pi = 0.15027$) with different lattice spacing and lattice volumes (Table 6.2.1). Bottom: ratio after folding.

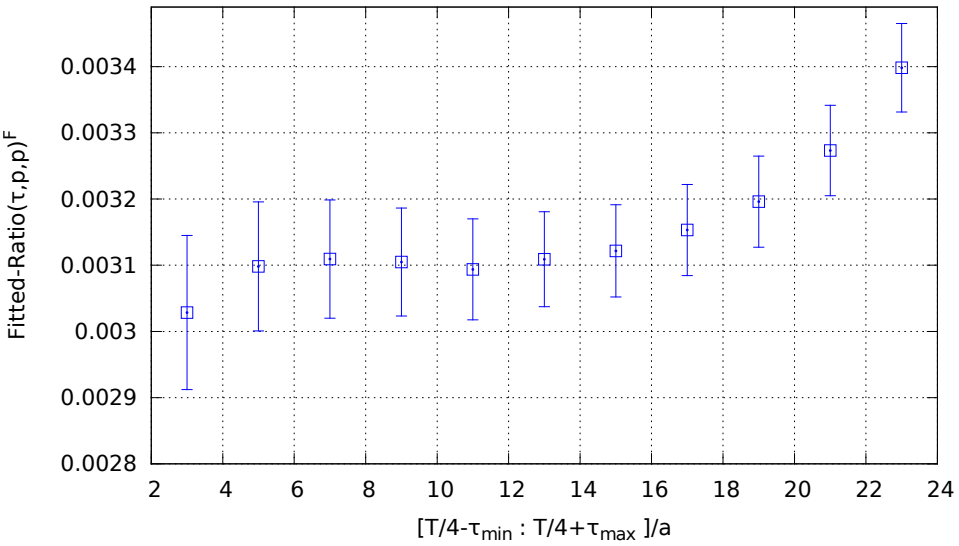

Figure 6.2.2: Results of fitting the folded ratio for ensemble (l) (Table .6.2.1) versus the different fitting intervals $[T/4 - \tau_{min} : T/4 + \tau_{max}]$. τ_{min} and τ_{max} are verified symmetric around $T/4$ ($5 \leq \tau_{min} \leq 15$ and $17 \leq \tau_{max} \leq 27$). The best choice of the fit interval is when the ratio gets stable.

of the backward half in the region $T/2 < t < T$ in order to reduces the statistical noise. The lower frame of Fig. 6.2.1 shows a zoom-in of such folded data to magnify the difference in obtaining the plateau before and after folding. We use the same color scheme as the upper frame of Fig. 6.2.1. As we see, a better signal can be gained if we first fold the two- and three-point function and then calculate the ratio.

Fitting Procedure

In order to extract the matrix elements, we fit Eq. (6.1.3) to the data where they exhibit a plateau in τ. The fitting process fits the data to a constant function. The results should be independent of the fitting window, if it is sufficiently small, but should depend if this window leaves the plateau. The range of the fitting windows are chosen symmetric around $T/4$ ($\Delta t = \delta t - T/4 + \delta t$). Hence, a curve with a minimal deviation from all data points is desired and the fitting curve is obtained by the method of least squares. The best fit is when the sum of squared residuals is minimal. A residual is the deviation between an observed data and the fitted value provided by a model.

Fig. 6.2.2 shows an example of fitted ratios of the three- and two-point functions at vanishing momentum versus different fitting windows. We used an ensemble with $\beta = 5.40$, $\kappa = 0.13660$, $48^3 \times 64$. We applied the folding method before fitting as explained above. The figure shows that results vary by the variation of the fit range and one has to adjust the window until the result does not change anymore.

Seeing a plateau for the ratio is expected only for $|p| = |p'|$. For higher momenta even far away from the source, the signal gets noisy. To underpin this fact, Fig. 6.2.3

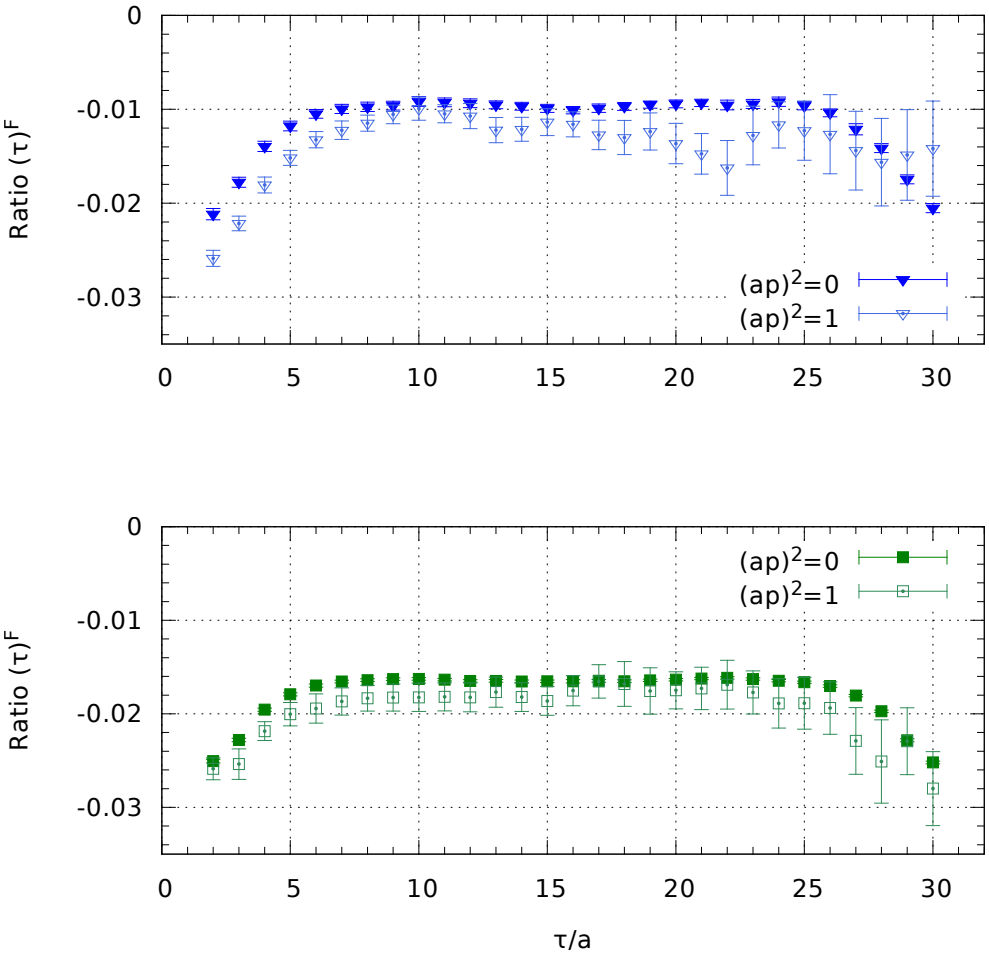

Figure 6.2.3: Ratio of current $\mathcal{O}_{v2b}$ at momentum $p^2 = 0$ and $(ap)^2 = 1$. Top: $\beta = 5.29$, $\kappa = 0.13632$ and volume $40^3 \times 64$ with lattice spacing $a = 0.0714$ fm and $m - \pi = 289$ MeV. Bottom: $\beta = 5.40$, $\kappa = 0.13640$ and volume $32^3 \times 64$ with lattice spacing $a = 0.0604$ fm and $m_\pi = 491$ MeV.

shows a comparison of the ratios from a calculation using a source at $(ap)^2 = 0$ and $(ap)^2 = 1$ for the operator $\hat{\mathcal{O}}_{v2b}$. Also, as it was illustrated in Fig. 5.1.7, for large non-vanishing momenta, due to the exponential decay of the pion two-point function, the signal close to t_{sink} is most noisy. Moreover, data points can be negative and the value of square root in Eq. (6.1.1) becomes impractical to calculate. Therefore, for these cases it is safer not to use the ratio but extract the pion energies and the coefficients by fitting the two-point functions and calculate matrix elements via Eq. (4.3.12). We should note that at higher momenta, fits become less stable due to an increased statistical noise.

At $\vec{p} > 0$ also the operator $\mathcal{O}_{v2a}$ gives non-zero expectation value and so can be used to extract (generalized) form factors. As an example for the lowest non-vanishing

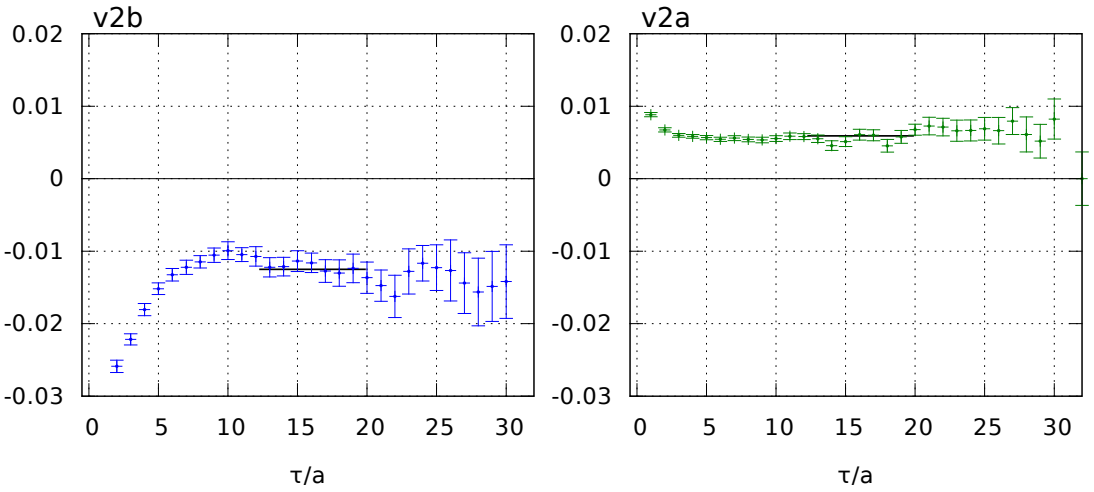

Figure 6.2.4: Folded ratio for operators $\hat{\mathcal{O}}_{v2a}$ and $\hat{\mathcal{O}}_{v2b}$ at $(ap)^2 = 1$ after doing symmetric folding for $\mathcal{O}_{v2b}$ and anti-symmetric for $\mathcal{O}_{v2a}$. The horizontal line is a fit to 8 data points around $T/4$.

momentum transfer $(ap)^2 = 1$, we have following operators

$$\begin{aligned}
\hat{\mathcal{O}}_{v2a}: \quad & \langle \hat{\mathcal{O}}_{14} \rangle = 2v_2 p^1 p^4, \\
& \langle \hat{\mathcal{O}}_{24} \rangle = 2v_2 p^2 p^4, \\
& \langle \hat{\mathcal{O}}_{34} \rangle = 2v_2 p^3 p^4, \\
& \langle \hat{\mathcal{O}}_{12} \rangle = 2v_2 p^1 p^2, \\
& \langle \hat{\mathcal{O}}_{13} \rangle = 2v_2 p^1 p^3, \\
& \langle \hat{\mathcal{O}}_{23} \rangle = 2v_2 p^2 p^3.
\end{aligned} \tag{6.2.2}$$

Fig. 6.2.4 shows the ratio at $(ap)^2 = 1$ as a function of the operator insertion time τ for $\mathcal{O}_{v2a}$ and $\mathcal{O}_{v2b}$ operators. When performing the folding method we have to keep in mind that $\mathcal{O}_{v2b}$ is symmetric around the $T/2$, while $\mathcal{O}_{v2a}$ is anti-symmetric. To solve the system of equations, we fit the ratio of each single operators in Eq. (6.2.2), and calculate the relevant prefactors. In order to calculate the ratio, we used the two- and three-point functions with the same momentum plugged into the ratio Eq. (6.1.1).

6.2.1 Excited State Contamination

In forward limit, contributions of excited state with energies $E'(p)$, $E''(p)$, ... are exponentially suppressed by factors of $e^{-(E'(p)-E(p))\tau}$ for forward propagators and $e^{-(E'(p)-E(p))(\tau - t_{sink})}$ for backward propagators. However, if τ as $(\tau - t_{sink})$ is not sufficiently large, excited states contribute.

In order to analyze excited state contamination to the ground state, for one ensemble $\beta = 5.29$ and $\kappa = 0.13632$ with $32^3 \times 64$, we set the source at zero and vary t_{sink}. We choose $t_{sink}/a = 32$ and $t_{sink}/a = 15$ and compute the matrix elements for $\mathcal{O}_{v2b}$ for both. The number of configurations for both cases is around 1000.

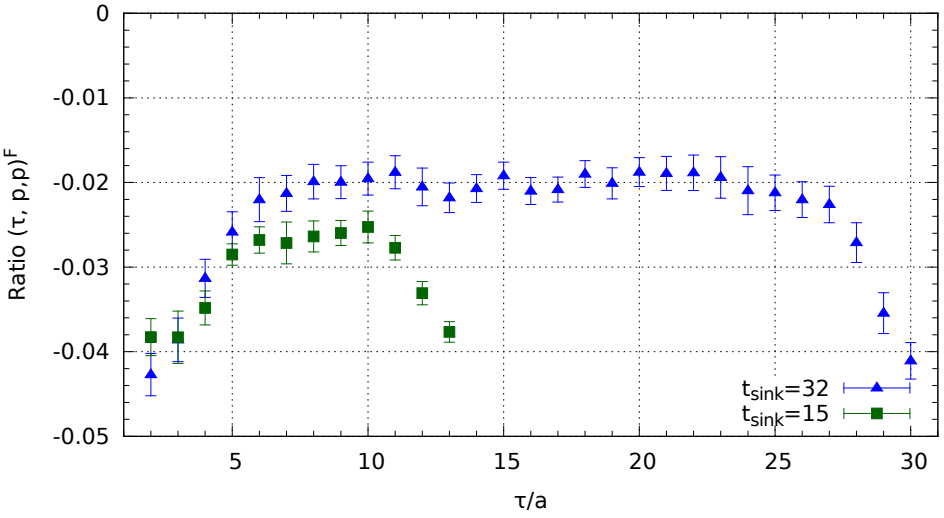

Figure 6.2.5: Folded ratio for O_{v2b} at $\vec{p}=0$ at 2 different sink positions ($\beta = 5.29, \kappa = 0.13632$ for $32^3 \times 64$ volume for one source per configurations.

Note that for $t_{sink} = 15$ the prefactor is not 1/2 (Eq. (6.1.4)) and we have to calculate the prefactor from the exponential part of Eq. (6.1.3). The ratios for both sinks are shown in Fig. 6.2.5. It shows a significant difference between the ratios ($R(T/4,\tau,p) - R(T/2,\tau,p) \sim 6\%$) which is due to the excited state contamination. Therefore, the separation between source and sink should be big enough to maximally suppress the effect of excited state and on the other hand small enough to have a good signal. For the nucleon, for example, the sink can not be set far away from the source due to the excited state contributions [B$^+$14a], while for pion t_{sink} can be set at $T/2$. This, in addition, allows us to apply folding. Also one should keep in mind that by decreasing the pion mass, the factor $e^{-E\tau}$ increases and gives a visible contribution.

In order to check the contamination of three-point function for $\vec{p} = \vec{p}'$ to next to leading order we have

$$\begin{aligned} C^{\mathcal{O}}_{3pt}(t,\tau,\vec{p}) &= Z_0(p)\langle\pi_0(\vec{p})|\mathcal{O}|\pi_0(\vec{p})\rangle e^{-m_0\Delta t} \\ &+ \sqrt{Z_1(p)Z_0(p)}\langle\pi_1(\vec{p})|\mathcal{O}|\pi_0(\vec{p})\rangle e^{-m_0\tau}e^{-m_1(\Delta t-\tau)} \\ &+ \sqrt{Z_0(p)Z_1(p)}\langle\pi_0(\vec{p})|\mathcal{O}|\pi_1(\vec{p})\rangle e^{-m_1\tau}e^{-m_0(\Delta t-\tau)} + \cdots . \end{aligned} \tag{6.2.3}$$

Here, $\Delta t = t_{sink} - t_{src}$ (in our calculations $t_{src} = 0$), and $|\pi_0(\vec{p})\rangle$ and $|\pi_1(\vec{p})\rangle$ represent the pion ground- and first-excited state of same momentum, respectively. By considering $\langle\pi_0|\mathcal{O}|\pi_1\rangle = \langle\pi_1|\mathcal{O}|\pi_0\rangle$ the fit function for the three-point function at next-to-leading order reads

$$Z_0 e^{-m_0 t_{sink}}\Big(B_0 + B_1[e^{-\Delta m(t_{sink}-\tau)} + e^{-\Delta m\tau}]\Big). \tag{6.2.4}$$

In order to calculate B_0 and B_1, we first use the combined fit for the two-point function to extract four factors, Z_0, m_0, Z_1 and m_1, and fit the three-point function then. Note

set (e)	fit-3pt	$\Delta t/a$	B_0	B_1
$t_{sink} = 15$	-2.5964	1	-2.8012	12.8724
		2	-2.7270	7.0132
		3	-2.5872	-2.7037
		4	-2.5317	-6.0668
$t_{sink} = 32$	-1.9391	4	-1.9920	303.7708
		6	-1.9700	139.4067
		8	-1.9368	4.1472
		10	-1.9278	-12.9536

Table 6.2.3: A selection of fitting three-point functions in vanishing momentum ($p = 0$).

that if excited state contributions are insignificant, B_0 reduces to the above mentioned ratio from Eq. (6.1.2).

Fig. (6.2.6) shows an uncorrelated fit to the pion three-point function for two different sink positions. For $t_{sink} = 32$ we first folded the data before fitting. The fit range is symmetrized around $t_{sink}/2$ and we checked different fitting windows $t_{sink}/2 \pm \Delta t$. For $t_{sink} = 15$ we can not choose Δt bigger than 4 due to the lattice artifacts close to the sink and source. The red line represents a fit to the three-point function neglecting excited state contributions and the blue dashed-line is fitting the three-point function to the ansatz in Eq. (6.2.4). The results are collected in Table 6.2.3.

We see that for $t_{sink} = 15$ the best fit we get is $\Delta t/a = 3$ for which B_1 has the smallest value. But the excited state contamination can still be seen, although the deviation of data-fit from B_0 is small. In contrast, for $t_{sink} = 32$ the best fit range is $\Delta t/a = 8$ which the fit to the data (-1.9391) is in good agreement with $B_0 = -1.9368$. It means the data is much less contaminated by excited state.

Therefore, we can conclude that our choice $t_{sink} = T/2$ plus an improved sink-source smearing is sufficient to suppress the excited state contaminations.

6.3 Forward Limit of GPDs

On the lattice by considering the renormalization and prefactors, the relation between local matrix elements and the second moment of the pion GPD can be written as

$$2\sqrt{E_{\vec{p}}E_{\vec{p}'}} \times Z^{\mathcal{O}} \times \underbrace{\langle \pi(\vec{p}')|\hat{\mathcal{O}}^{\mu\nu}(0)|\pi(\vec{p})\rangle}_{2\times R(t_{sink},\tau,\vec{p}',\vec{p})} = 2\bar{P}^{\mu}\bar{P}^{\nu}A^{\pi}_{2,0}(t) + 2\Delta^{\mu}\Delta^{\nu}C^{\pi}_{2,0}(t). \tag{6.3.1}$$

Here, $Z^{\mathcal{O}}$ is the renormalization factor and $E_{\vec{p}}$ and $E_{\vec{p}'}$ are the energy of initial and final pion respectively. In the forward limit, $\Delta \to 0$, the second moment of GPD reduces to the quark distribution functions and Eq. (2.4.9) can be written as

$$A^{\pi}_{2,0}(t=0) = \frac{2 \times Z^{\mathcal{O}} \times R(t_{sink},\tau,\vec{p},\vec{p})}{m_{\pi}} \tag{6.3.2}$$

where we used Eq. (5.1.4). Inserting the fitted ratio R, we calculate $A^{\pi}_{2,0}(0) = \langle x \rangle^{\pi}$.

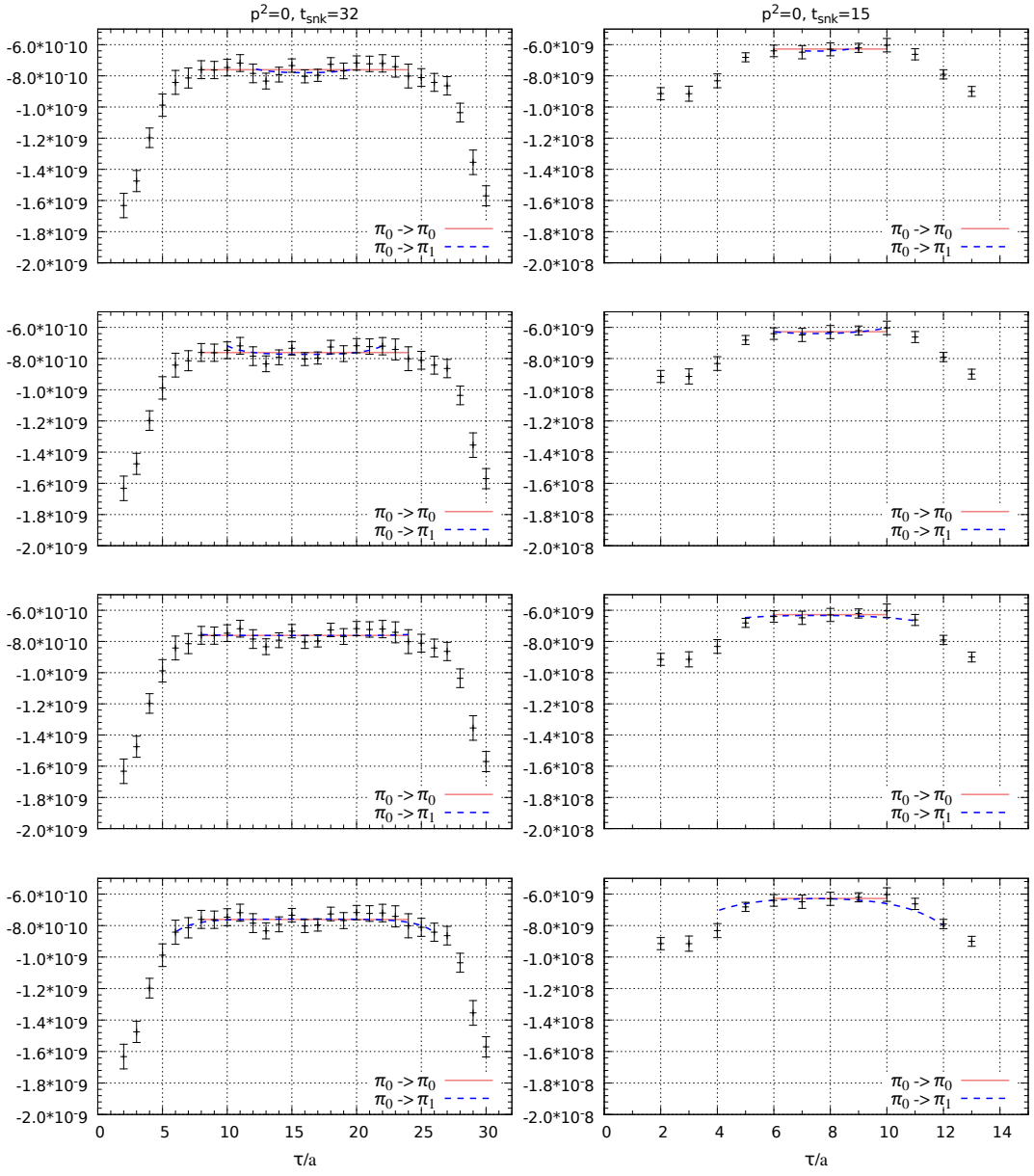

Figure 6.2.6: Comparison of fits for three-point functions at different fitting windows (from small to big), left: $t_{sink} = 32$, right: $t_{sink} = 15$.

μ^2[GeV]^2	$\langle x\rangle_{\mu^2}$	$\langle x\rangle_{\mu^2=4}$	Reference
4	0.20 ± 0.02		[S$^+$92]
4	0.24		[H$^+$01]
27	0.217 ± 0.011	0.2515	[Wo05]
4	0.231		[Aic10]
27	0.184	0.213	[Nam12]
	0.214	0.248	
	0.230	0.267	

Table 6.3.1: Moments of the pion PDF, evaluated from Drell-Yan experiments and modeling. First column shows the scale which analysis was performed at. The second column shows the corresponding data. In th third column we convert the $\langle x\rangle$ value to $\mu^2 = 4$. We need this value for our comparison.

There exists data from several experiments and also different lattice groups which we will compare to.

6.3.1 Moments of PDF (Experiments and Modeling)

P. J. Sutton and his colleagues performed a next-to-leading order analysis of the Drell-Yan $\pi^- N \to \mu^+\mu^- X$ data obtained by the NA10 [B$^+$87] and E615 [C$^+$89] collaborations to calculate the valence quark ($u = d$) distributions of the pion (xv^π) in 1992. The quark distributions were given in the $\overline{\text{MS}}$ scheme at $Q^2 = Q_0^2 = 4$ GeV^2. In order to compare with the lattice results they calculated the moment of the pion PDF ($\int_0^1 dx\, xv^\pi$) [S$^+$92].
The calculation for pion's valence quark distribution function using a Dyson-Schwinger equation[1] was done in 2000[H$^+$01].

A re-analysis of the moments of parton distribution function of the pion in the valence region at next-to-leading order was done by Fermilab E-615 pionic Drell-Yan data in 2005[Wo05].

Later, in 2010, moments of pion PDFs were calculated by performing a new NLO analysis of the experimental data for a Drell-Yan process [Aic10]. There, different fits were performed for several different values of its total momentum fraction $\langle xv^\pi\rangle = \int_0^1 xv^\pi(x, Q_0^2)$ with the initial scale $Q_0 = 0.63$ GeV. In Table 6.3.1 their result for fit 3 is shown [Aic10].

In 2012, the investigation of the π^+ PDFs was performed employing a gauge-invariant effective chiral action from the non-local chiral quark model [Nam12]. In this model all parameters are determined phenomenologically.
These data are summarized in Table 6.3.1. We have to converted the data, which were calculated in different scale μ^2, to $\mu^2 = 4\,\text{GeV}^2$ to be able to compare with our data.

[1] Dyson-Schwinger equations (DSE) constitute a set of interconnected equations of Green functions (n-point functions) in quantum field theories (QFTs). They thus form an infinite set of coupled integral equations.

6.3.2 Moments of PDFs (Lattice Results)

In section 3.4 we mentioned that due to the numerical costs, most of lattice studies have been performed in the quenched approximation in the past. That is, all quark loops were neglected.

So, for example, in the late 1980's, Martinelli and Sachrajda calculated the first and second moments of the pion distribution function, $\langle x \rangle_\pi$ and $\langle x^2 \rangle_\pi$ in the quenched truncation [MS87].

Further quenched data, also for the next higher moment $\langle x^3 \rangle_\pi$, became available in 1997 from the QCDSF collaboration, by using Wilson fermions and with three current-quark masses $m_\pi \approx 480, 650, 780$ MeV [B+97].

In 2003 lattice data for moments of pion PDFs were analyzed in the framework of chiral perturbation theory and unquenched data has become available from 2003 [D+03].

In 2003 the ZeRo collaboration studied the pion matrix elements of the twist-two operator utilizing the standard Wilson gauge action and a non-perturbatively improved clover action [W+04], and in 2005 they reported the momentum fraction of quarks in the pion in the chiral limit [G+05].

In 2006 the lowest moment of the valence quark parton distribution function in the pion was presented by the χLF collaboration using Wilson twisted mass fermions and the Wilson plaquette gauge action for pion mass of approximately 270 MeV for up to five different lattice spacing [C+06b].

Unquenched but unrenormalized lattice data was also obtained by the European Twisted Mass collaboration in 2007 [B+07a].

Around the same time, a detailed study of the lowest moments of the pion parton distribution functions in unquenched lattice QCD has been presented by the QCDSF collaboration. They employed $\mathcal{O}(a)$-improved Clover-Wilson fermions with two dynamical quarks with the pion masses $430, 600, 800$ MeV. The data was shown in the chiral limit [Brö07]. These data are listed in Table 6.3.2.

6.3.3 Finite Size Effect on moments of PDF

Any numerical lattice QCD calculations imply discretization and finite volume artifacts. These need to be analyzed carefully. An important parameter to reduce finite size effect is the boundary condition taken for quark fields. Using periodic boundary in the spatial direction helps to reduce this effect asymptotically [A+94] and these finite size effects are exponentially suppressed ($\sim \exp(-m_\pi L)$) where m_π is the pion mass and L is the spatial extent. Therefore, in order to suppress finite size effects, we need $m_\pi L$ to be sufficiently large. However, one is typically limited by memory size and computational power. Note that when the pion mass is much higher than the physical value, finite size effect at the same physical lattice size and lattice spacing is easier to control. A rule of thumb says that finite size effects are typically small if $m_\pi L > 4$.

Studies of the boundary condition in quenched approximation and full lattice QCD with the same lattice size and lattice spacing shows that, there is a partial cancellation of the finite size effects, if the $Z(3)$[2] symmetry of the quenched action is intact. Dynamical fermions break the $Z(3)$ symmetry and hence, in full QCD such a cancellation does not

[2] $Z(3)$ is described as a group with three elements x^0, x^1, x^2.

μ^2[GeV]^2	$\langle x \rangle_{\mu^2}$	Renor. scheme	Reference
49	0.23 ± 0.07	$\overline{MS}$	[MS87]
5.7	0.273 ± 0.012	$\overline{MS}$	[B$^+$97]
5.7	0.21 ± 0.02	$\overline{MS}$	[D$^+$03]
4	0.265 ± 0.015	$\overline{MS}$	[W$^+$04]
4	0.246 ± 0.015	$\overline{MS}$	[G$^+$05]
4	0.243 ± 0.021	$\overline{MS}$	[C$^+$06b]
?	0.295 ± 0.003	bare	[B$^+$07a]
	0.279 ± 0.004		
	0.268 ± 0.008		
	0.251 ± 0.008		
4	0.271 ± 0.002	$\overline{MS}$	[Brö07]
4	0.4046 ± 0.0028	RGI	
	0.397 ± 0.011		
	0.386 ± 0.018		

Table 6.3.2: Overview of the first moments for the pion $\langle x \rangle$. The first column lists the renormalization scale.

take place. Therefore, finite size effects for quenched QCD are smaller than those for full QCD [A$^+$94].

Now we discuss the effect of finite lattice size for similar pion masses ($m_\pi \approx 290\,\mathrm{MeV}$) at $\beta = 5.29$ with lattice spacing $a = 0.0714$ fm for volumes $L/a^3 \times 64$ with $L/a = 32$, 40, 64 corresponding to the lattice extents $L = 2.28$, 2.85 and 4.57 fm respectively.

In the infinite volume limit, one expects the same mass when β and κ are the same. In Fig. 5.1.11, the effect of finite size in the masses for the same κ and β is illustrated. Fig. 6.3.1 displays the finite size effect of the ratio. The left frame of Fig. 6.3.1 shows zoomed ratio for different volumes, the right frame corresponding $\langle x \rangle$ versus L. We see the finite size effect is significant and by increasing the volume, the effect of finite size decrease.

6.4 Results of PDFs

Fig. 6.4.1 shows our results for the available pion mass range (full triangles up at lattice spacing $a \approx 0.06$ fm, full triangle down at $a \approx 0.07$ fm and full diamond at $a \approx 0.08$ fm). Our data are listed in Table 6.3.3.

To underpin the effect of our improved sink-source smearing we compare them with results from [Brö07] (gray crosses). Those results were partly obtained on the same gauge ensembles but for a different type of smearing. Here we should note that the data from [Brö07] in Fig. 6.4.1 (gray crosses) are multiplied by the factors from Table C.4 in [Brö07] to convert RGI to $\overline{\mathsf{MS}}$ scheme at the scale $\mu^2 = 4\,\mathrm{GeV}^2$. A comparison shows a systematic deviation between those old and our new data. Our results lie

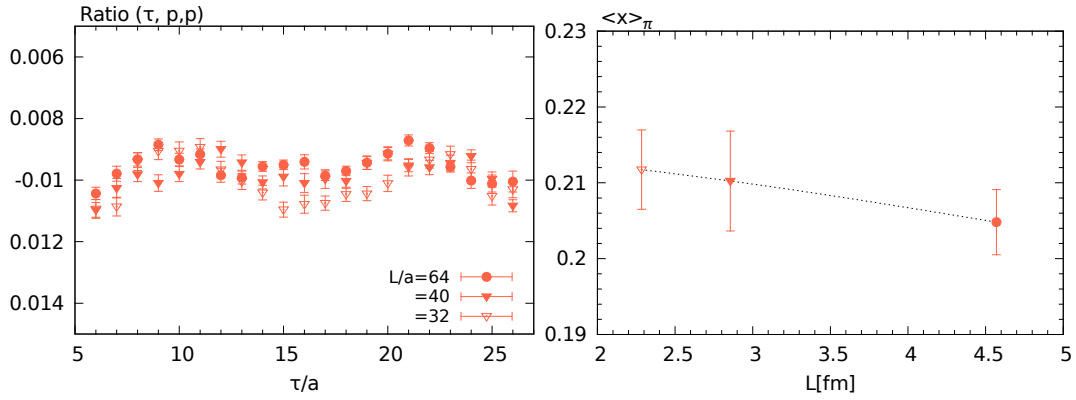

Figure 6.3.1: Left: ratios for 3 different set of simulations with the same κ and β but for different pion masses to show the finite volume size effect. The analysis are done based on the smallest m_π. The result is after doing folding. Right: size dependence of $\langle x \rangle_\pi$.

	a [fm]	$m_\pi^2 [MeV]$	$\langle x \rangle_\pi^{\mathcal{O}_{v2b}}$
(a)	0.0813	0.0784	0.20108 (799)
(b)	0.0714	0.439	0.27078 (326)
(c)		0.1832	0.22984 (369)
(d)		0.1789	0.24068 (135)
(e)		0.0870	0.21173 (512)
(f)		0.0841	0.21023 (658)
(g)		0.0835	0.20481 (429)
(i)		0.0228	0.14721 (1492)
(j)	0.0604	0.2410	0.25058 (187)
(k)		0.1823	0.23582 (213)
(l)		0.0681	0.18055 (270)

Table 6.3.3: Moments of the pion PDF $\langle x \rangle_\pi^{cont}$ in $\overline{\text{MS}}$ scheme at $\mu = 2$ [GeV] for ensembles listed in Table 6.2.1.

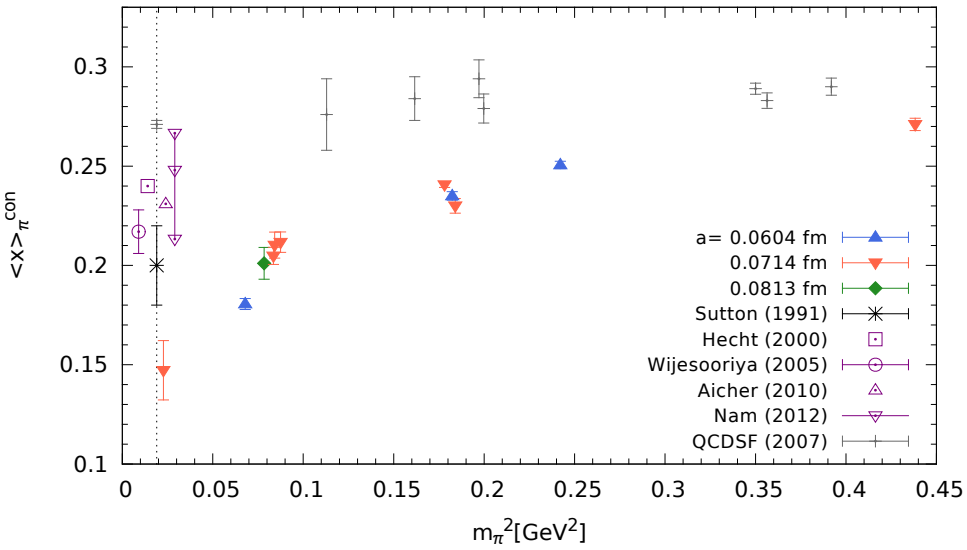

Figure 6.4.1: Connected part of the first moment of the pion PDF $\langle x\rangle_\pi^{con}$, in the $\overline{\text{MS}}$ scheme, versus the pion mass in physical units. Full symbols are used for our data. We chose the same symbol and color for the same lattice spacing. Open symbols are for different phenomenological analyses and a star denotes the experimental value which all are listed in Table 6.3.1. Open circle, squares, triangle up and down are shifted by -0.01, -0.005, 0.005 and 0.01 respectively. Gray crosses show the unquenched lattice data presented by QCDSF from [Brö07]. The vertical dashed line marks the position of the physical pion mass.

systematically below those of [Brö07] and this deviation increases with decreasing m_π due to $e^{-E\tau}$. The utilized improved sink-source smearing technique was optimized to minimize the excited state contributions to the two-point function and obviously seems to smooth out most of the excited state contaminations. Therefore, we have a much better control over excited state contributions [B$^+$14a].

Our data is also smaller than those from phenomenology. This might be due to the fact that our data only contains contributions from connected diagrams. Also, due to the absence of deep-inelastic scattering for the pion, the phenomenological values are less accurate than for example the nucleon [S$^+$92]. For a better visibility in Fig. 6.4.2 the data of [Wo05] and [H$^+$01] are shifted by -0.01 and -0.005 and [Aic10] and [Nam12] by $+0.005$ and $+0.01$ respectively. Note that in Fig. 6.4.1, the data from [Nam12] and [Wo05] are rescaled to $\mu^2 = 4\,\text{GeV}^2$. In Fig. 6.4.2 we specify our data for different $m_\pi L$. The open symbols denote the data with $3.4 < m_\pi L < 4$ and full ones denote $m_\pi L > 4$. The blue and red lines mean nothing but connect the data points with lattice spacing $a \approx 0.06\,\text{fm}$ and $a \approx 0.07\,\text{fm}$ respectively to guide the eyes. It can be clearly seen that $\langle x\rangle_\pi$ shows the shift regarding the lattice spacing.

Since our outcome on almost physical pion mass is lower that those form phenomenology (black star), it indicates that for the pion contributions from disconnected diagrams seems to be non-negligible.

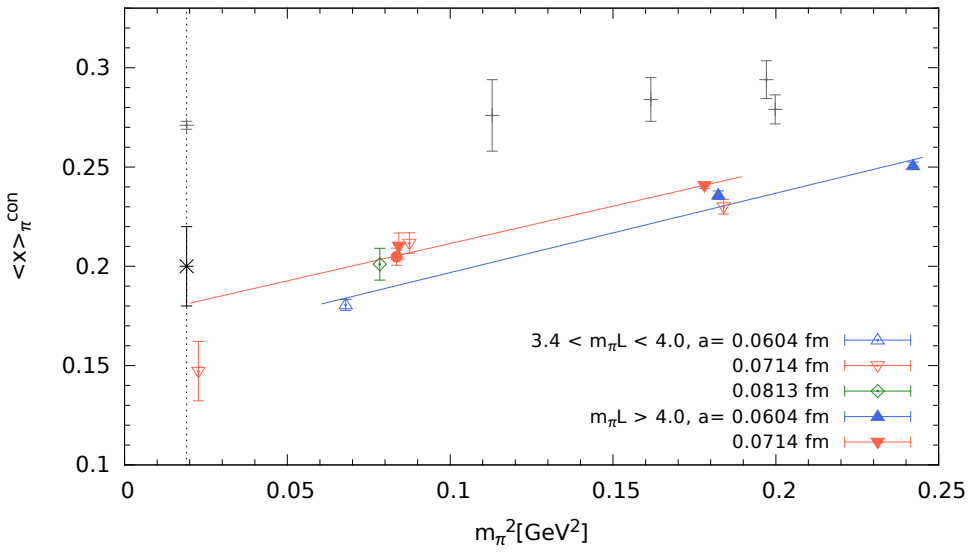

Figure 6.4.2: $\langle x \rangle_\pi^{con}$. Open symbols are data for $3.4 < m_\pi L < 4.0$ and solid symbols for $4.0 < m_\pi L$. Solid circle denotes $\langle x \rangle$ with $m_\pi L \approx 6.7$. Different colors are for different lattice spacing. Lines are to better visualize the shift in the data for different lattice spacing.

Chapter 7

Pion Form Factors and Generalized Form Factors

In modern language, hadron structure is expressed in terms of generalized parton distribution functions. GPDs contain the electromagnetic form factor and the parton distribution functions as limiting cases. In chapter 6 we have presented our results for the first moment of the pion PDFs using lattice techniques. It has been the main topic of our project toward a better understanding of the pion inner structure. PDFs are functions of the longitudinal momentum fraction and generalized parton distributions depend on longitudinal momentum fraction and the total momentum transfer as well.

Since a pion is made up from a pair of quark and anti-quark, its form factor is an important quantity for the hadronic structure. In this chapter we discuss how to extract its form factor via matrix elements and then look at its momentum dependence. We will present our results for the pion electromagnetic and also generalized form factor at several momentum transfers.

7.1 Form Factor - Experiments and Lattice

In section 2.2.1 we summarized the properties of form factors and showed that $f_{\pi\pi}(Q^2)$ is given by a matrix element of local operators at a particular squared momentum transfer $Q^2 = -t = -q^2 = -(p-p')^2$. In the quark model, the pion electromagnetic form factor is given in terms of the local vector current $\mathcal{O}_V^\mu$, which for $N_f = 2$ sea quarks is defined as

$$\mathcal{O}_V^\mu = \frac{2}{3}\bar{u}\gamma_\mu u - \frac{1}{3}\bar{d}\gamma_\mu d. \tag{7.1.1}$$

Factoring out the prefactors, Eq. (2.4.1) can be written as

$$2\sqrt{E_{\vec{p}}E_{\vec{p}'}} \times Z_V \times \underbrace{\langle \pi(\vec{p}')|\mathcal{O}_V^\mu(0)|\pi(\vec{p})\rangle}_{2\times R(t_{sink},\tau,\vec{p}',\vec{p})} = 2\bar{p}^\mu f_{\pi\pi}(t) \tag{7.1.2}$$

with $\bar{p} = (p_f + p_i)/2$. The detailed calculation is given in Appendix B.2. In case the sink is placed at $T/2$, the matrix element simplifies to the ratio (Eq. (6.1.4)) multiplied by factor 2.

Eq. (7.1.2) shows that the form factors depend on the momentum transfer Q^2. At the small space-like momentum transfer regime, the NA7 collaborations have measured the pion form factor from the pion-electron scattering experiment [A$^+$86]. At large Q^2, measurements have been performed via the electroproduction of single charged pions (see, e.g., [B$^+$78, A$^+$78, B$^+$79]). A re-analysis of the data was done by the JLAB-F$_\pi$ collaborations from the high-energy electroproduction of pions (see. e.g., [V$^+$01, H$^+$06, H$^+$08a, T$^+$07, H$^+$08b]).

At the intermediate Q^2 regime, some initial calculations were performed using lattice QCD in the quenched approximation (see, e.g., [vdH$^+$03, B$^+$05, C$^+$06a]). It was followed by lattice simulations with dynamical fermions (see, e.g., [B$^+$08, B$^+$07c, A$^+$09, F$^+$09, N$^+$11]).

Lattice results were in agreement with experiments (Fig. 7.1.1). There, the black stars represents the outcome for form factors measured experimentally by NA7 collaborations [A$^+$86]. Blue open triangles up display the data computed with $m_\pi = 330\,\text{MeV}$ using an ensemble of the RBG/UKQCD collaboration's gauge configurations [B$^+$08]. Violet full and open circles are electromagnetic form factors calculated on the $N_f = 2+1$ PACS-CS gauge field configurations with $m_\pi = 296\,\text{MeV}$ and 411 MeV respectively [N$^+$11]. Two violet lines illustrate the shift of electromagnetic form factor with respect to the pion mass. Green full squares show the lattice calculation of ETMC with $m_\pi = 260$ MeV utilized twisted boundary conditions [F$^+$09]. Full and open red diamonds show the data used partially twisted boundary conditions for different pion masses in the range (254-455) MeV [Bra12]. Also data form [Bra12] shows the shift relevant to the pion mass.

In lattice QCD, the momenta are restricted by the volume and the lattice spacing. Therefore, calculating the form factors at the very small Q^2 becomes difficult. When periodic boundary conditions in spatial direction are used, the lattice momenta are $(2\pi a p_i)/(L)$, with $i = x, y, z$. The momentum transfer is then

$$Q^2 = (E - E')^2 + \sum_{i=1}^{3} \left(\frac{2\pi a}{L}(p_i - p_i')\right)^2. \tag{7.1.3}$$

For example, for a common lattice with $L/a = 32$ and $a^{-1} = 2764\,\text{MeV}$ with $m_\pi = 295\,\text{MeV}$ the minimum virtuality is $Q^2_{min} = 0.197\,\text{GeV}^2$. This means that with conventional periodic boundary conditions there exists no data for momentum transfer bellow Q^2_{min}.

In order to improve the momentum resolution for lattice studies, different boundary conditions named *twisted* boundary conditions should be used (see, e.g., [SV05, GMS06]). When one uses gauge configurations generated with sea quarks with periodic boundary conditions and valence quarks with twisted boundary conditions, it is called *partially twisted* boundary conditions [B$^+$07b].

This is in particular important for $f_{\pi\pi}(Q^2)$, because at small Q^2 the form factor defines the charge radius $\langle r^2 \rangle$, Eq. (2.5.9)

$$f_{\pi\pi}(Q^2) = 1 - \frac{\langle r_\pi^2 \rangle}{6} Q^2 + \cdots \Rightarrow \langle r_\pi^2 \rangle = -6 \frac{df_{\pi\pi}(Q^2)}{dQ^2}\Big|_{Q^2=0}. \tag{7.1.4}$$

The major task of our project was to calculate the moments of pion PDFs where periodic boundary conditions were utilized. We also calculated the electromagnetic

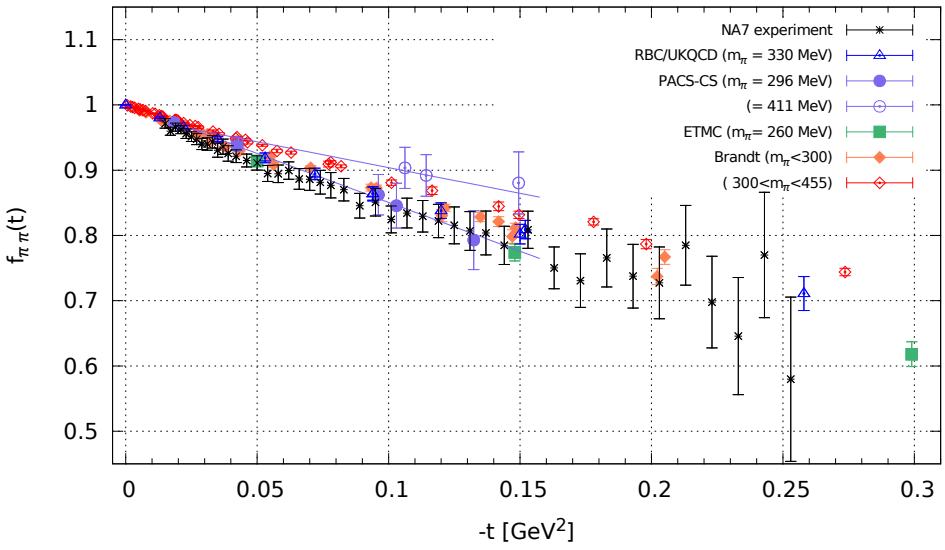

Figure 7.1.1: Pion electromagnetic form factor versus momentum transfer in physical units. Selection of lattice results (Violet full and open circles [N$^+$11], blue open triangles up [B$^+$08], green full squares [F$^+$09], red full and open diamonds [Bra12]) compared to experiment (black stars [A$^+$86]).

form factor with the same boundary conditions. We thus can not reach such low values of Q^2_{min} using partially twisted boundary conditions.

7.2 Results for Electromagnetic Form Factor

In chapter 6.1 we explained how to calculate matrix elements of a local operator. For calculating the electromagnetic form factor, Eq. (7.1.2) and the rank 1 operators from Table 4.4.1 are used.

In our calculations, we place t_{sink} at $T/2$ and set the sink momentum to zero. The reason for this was the calculation of the moments of pion PDFs. In order to calculate the form factor for higher momentum transfer Q^2, the maximum momentum for two- and three-point functions is set to $|ap|^2 = 6$, Eq. (5.1.9). Since the two-point function at high momentum becomes noisy, (see the left frame of Fig. 5.1.7), the uncertainties of the electromagnetic form factor become large by increasing the momentum. This is an artifact of solving the system of equations.

Fig. 7.2.1 illustrates our result for the electromagnetic form factor for the vector operators $\mathcal{O}_4^V$ on all ensembles (except (b) and (h)) listed in Table 6.2.1. The results are classified based on the pion mass in three colors; red for light pion $m_\pi \approx 151\,\text{MeV}$, blue for $m_\pi \approx (260 - 295)\,\text{MeV}$, and green for heavy ones $m_\pi \approx (423 - 491)\,\text{MeV}$. We see the expected shift of the electromagnetic form factors with respect to the pion mass.

Fig. 7.2.1 shows that at high momentum transfer $f_{\pi\pi}(t)$ trends to be zero fast. Also there exists a dilemma for data with pion mass close to the physical value (red triangles

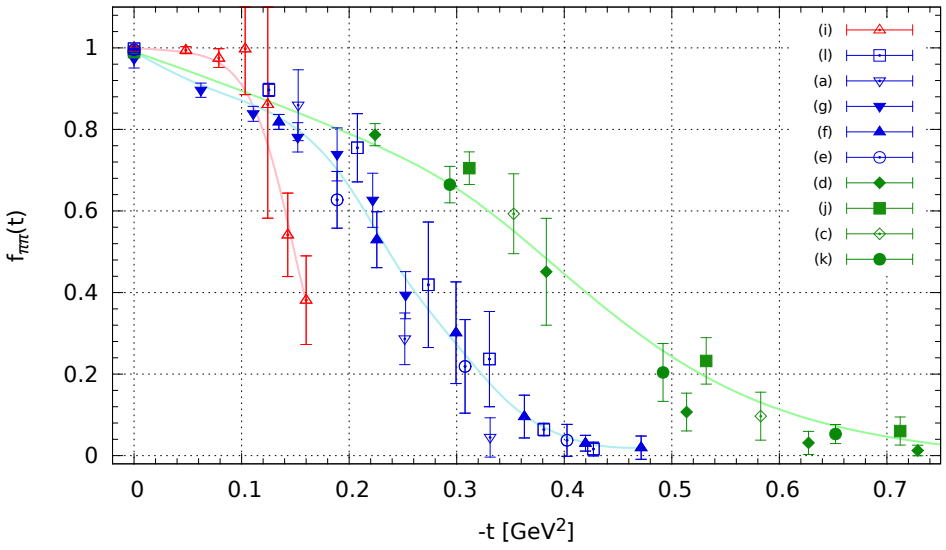

Figure 7.2.1: Pion electromagnetic form factors for ensembles listed in Table 6.2.1. Open symbols indicate $m_\pi L < 4$ and full ones $m_\pi L > 4$. Different colors specify different pion mass ranges (red $m_\pi \approx 151\,\text{MeV}$, blue $m_\pi \approx (260 - 295)\,\text{MeV}$, green $m_\pi \approx (423 - 491)\,\text{MeV}$). Splines are to guide the eyes.

up). Therefore, we examine two different methods to improve these results. Because of a lack of computing time, we could not use the ensemble with small m_π and large L. Therefore, we chose an ensemble with a common pion mass; ensemble (e). We used the following:

First method We set the sink momentum to zero and choose two sink positions, $t_{sink} = 15$ and 32 (see the left frame of Fig. 7.2.2). It displays that for $t_{sink} = 15$ there is a gradual slope for smaller momentum transfer, but for higher Q^2, results for both sink positions, 15 and 32, return to zero again. Hence, this method alone can not be the solution for our puzzle. The related charge radius from Eq. (7.1.4) is $\langle r_\pi^2 \rangle_{ts=15} = 0.281\,(10)\,\text{fm}^2$ and $\langle r_\pi^2 \rangle_{ts=32} = 0.445\,(14)\,\text{fm}^2$. Although, we are not able to calculate the charge radius properly because there is no existing data on very small Q^2. Placing the sink in the middle of the lattice $t_{sink} = T/2$ results in the pion charge radius closer to that known from phenomenology 0.452(11) fm^2 [E$^+$04] than for $t_{sink} = T/4$.

Second method We set the sink at position $t_{sink} = 15$ and compare data for zero and non-zero sink momentum. In chapter 5 we saw that by increasing the momentum, uncertainties of the two-point function also increase. So, for the case sink at non-zero momentum, we set the maximum momentum for the two-point function to $|ap|^2 = 2$. As a consequence, the uncertainties become smaller due to the cut-off of the bad signal for two-point function at higher momenta. The right frame of Fig. 7.2.2 shows the result. The results for sink at non-zero momentum (red points) are less noisy at higher momentum transfer. Also the slope is considerably

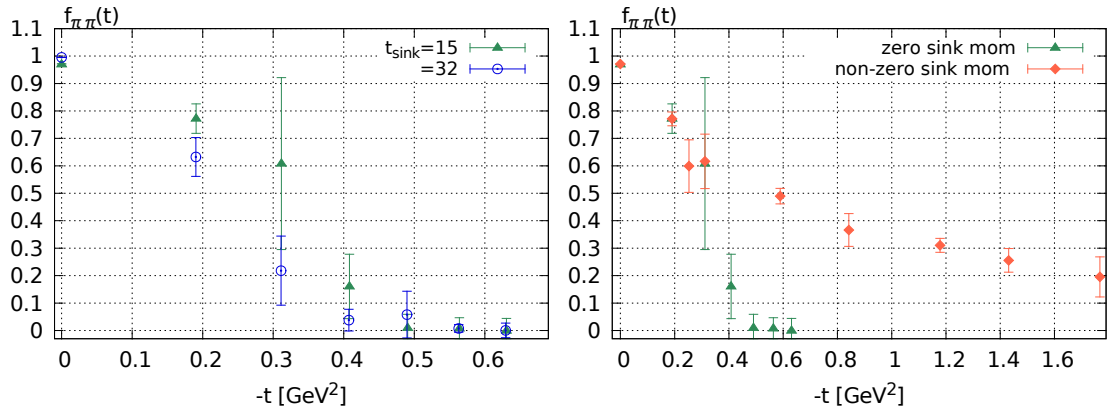

Figure 7.2.2: Left: comparison between $f_{\pi\pi}(t)$ for $t_{sink} = 15$ (green triangle up) and $t_{sink} = 32$ (blue circle) both for sink momentum at zero. Right: $f_{\pi\pi}(t)$ for zero sink momentum (green triangle up) and non-zero sink momentum (red diamond) both at $t_{sink} = 15$.

less sharp and we can obtain a signal even for higher Q^2. So, we can conclude that the second method can solve our puzzle.

We should remark that the results shown in the left frame of Fig. 7.2.2 represent only for a subset of configurations to save computing time. So one has to examine this method with the whole set of configurations.

Despite the lack of data for sink position in the middle of the lattice $T/2$ with non-zero sink momentum, Fig. 7.2.2 encourages us to conclude that putting the sink at zero momentum is not very practical to calculate the electromagnetic form factor for higher momentum transfer.

Fig. 7.2.3 displays the comparison between our outcome and previous results (experiment and lattice) for pion masses smaller than 300 MeV for low momentum transfers. This figure shows we are in agreement with foregoing data for low momentum transfer with the non-physical pion masses. For the lightest pion, $m_\pi \approx 151\,\text{MeV}$, there exists a discrepancy, though. This fact can be interpreted due to excited state contaminations which become larger at smaller masses, $e^{-\Delta m \tau}$. Although, we used smearing to remove excited state effects. Also one should keep in mind that this simulation can be affected by finite volume effects since $m_\pi L < 4$. This needs to be further investigated in future studies. Fig. 7.2.4 shows the comparison for higher pion masses up to 500 MeV. Because of using periodic boundary condition, we have no access to the small momentum transfer. Though, at high momentum we are in good agreement with foregoing outcomes.

Fig. 7.2.5 illustrates some results for the pion charge radius. The full triangle down is our data for ensemble (g) with pion mass 290 MeV using periodic boundary condition which forces us to have the smallest momentum transfer equal to $2\pi a/L$ to extract pion charge radius. Open triangles are data obtained form PACS-CS [N$^+$11], open squares from ETMC [F$^+$09], open diamonds from [Bra12] and open triangles up from [B$^+$08]. All data are collected in Table 7.2.1. The star symbol presents result reported by NA7 experiments [A$^+$86]. The figure displays that our result using periodic boundary

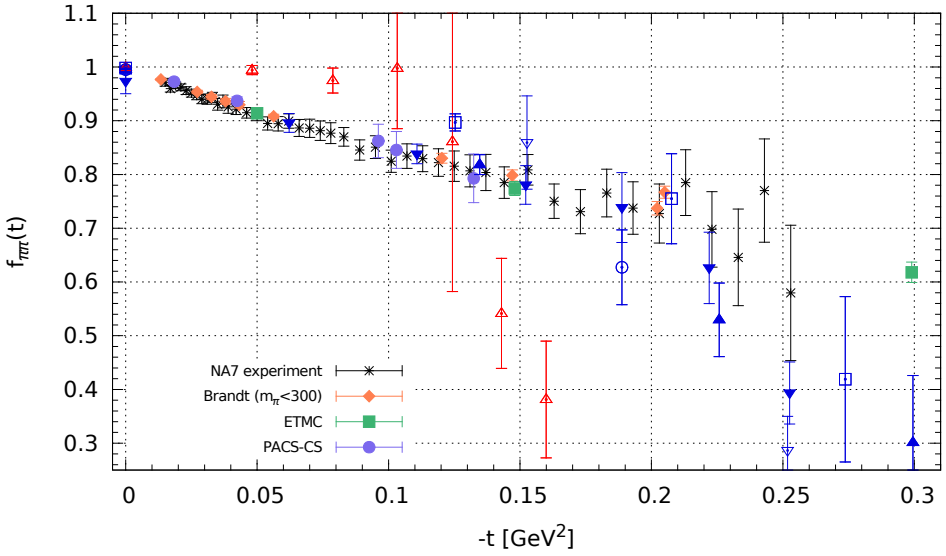

Figure 7.2.3: Comparison between our calculations (open and full symbols) and foregoing results at small virtualities for pion masses smaller than 300 MeV. Colors and symbols are the same for Fig. 7.1.1 and 7.2.1.

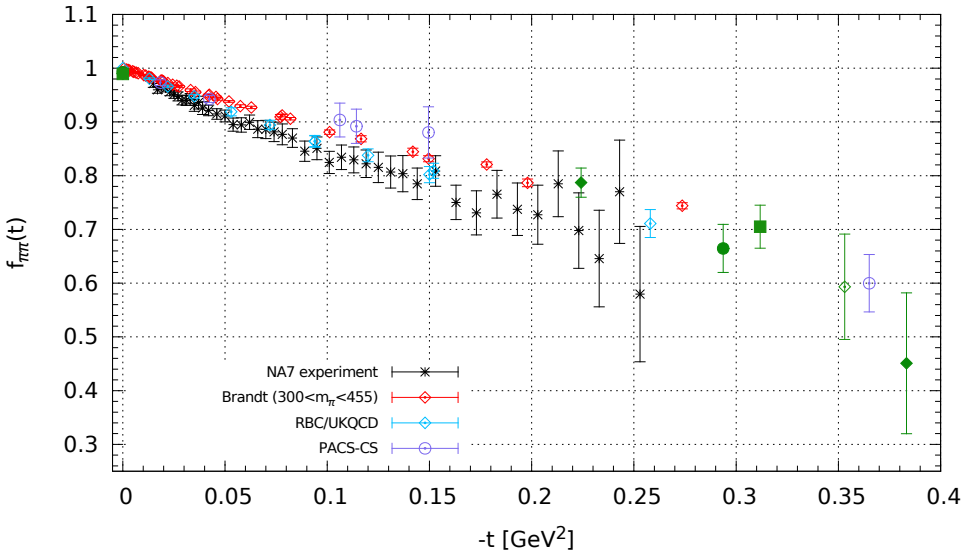

Figure 7.2.4: Electromagnetic form factor results for pion masses larger than 300 MeV up to 500 MeV. The colors and symbols are the same as shown in Fig. 7.1.1 and 7.2.1.

M_π [MeV]	$\langle r_\pi^2 \rangle$ [fm^2]	Reference
289	0.290 (18)	This work (Ens. g)
139.57	0.451 (8)	PDG [O$^+$14]
Physical mass	0.439 (8)	NA7 experiment [A$^+$86]
330	0.354 (31)	RBC/UKQCD [B$^+$08]
265	0.352 (30)	ETMC [F$^+$09]
304	0.345 (21)	
383	0.285 (19)	
296	0.3352 (160)	PACS-CS [N$^+$11]
411	0.3129 (84)	
351 (Ens. A4)	0.291 (21)	[Bra12]
299 (Ens. A5)	0.349 (21)	
296 (Ens. F6)	0.339 (19)	
254 (Ens. F7)	0.409 (29)	

Table 7.2.1: A collection of lattice results for the pion charge radius in comparison to experimental estimates.

condition is in reasonable agreement with data using twisted boundary condition.

7.3 Generalized Form Factor

In the context of GPDs, there are more form factors than just the electromagnetic. Those which parametrize moments of GPDs are called generalized form factors (GFFs). GPDs are off-forward distributions which are relevant for the description of DVCS experiments and hard exclusive electroproduction of mesons. The GPDs can not calculated on the lattice, their moments however can.

In section 2.2.1 it was explained how to extract the pion generalized form factors from matrix elements. Similar to the electromagnetic form factor, factoring out the prefactors, Eq. (2.4.5) can be defined as

$$2\sqrt{E_{\vec{p}}E_{\vec{p}'}} \times Z_V \times \underbrace{\langle \pi(\vec{p}')|\mathcal{O}_V^{\mu\nu}|\pi(\vec{p})\rangle}_{2\times R(t_{sink},\tau,\vec{p}',\vec{p})} = 2\bar{p}^\mu \bar{p}^\nu A_{2,0}^\pi(t) + 2\Delta^\mu\Delta^\nu C_{2,0}^\pi(t) \tag{7.3.1}$$

with $\Delta = p - p'$ and $\bar{p}^\mu = (p' + p)/2$. $\mathcal{O}_V^{\mu\nu}$ is the twist-two operator from Table 4.4.1. The detailed calculations are described in Appendix B.4.

Fig. 7.3.1 shows data for generalized pion form factors, $A_{2,0}^\pi$ (top frame) and $C_{2,0}^\pi$ (bottom frame). These come with even larger statistical uncertainties than we saw for the electromagnetic form factor. A pion mass dependence for $A_{2,0}^\pi$ and $C_{2,0}^\pi$ is seen nonetheless. At $Q^2 = 0$ this dependence is, of course, the same as we see it for moments of PDFs, Fig. 6.4.1. This dependency persists also for larger Q^2.

In Fig. 7.3.1 we see a similar fall off at higher momentum transfer as for the electromagnetic form factors. Therefore, we examine those methods which were checked for the electromagnetic form factor for simulation (e) with $\beta = 5.29$ and $\kappa = 0.13632$ and volume $32^3 \times 64$. The left frames of Fig. 7.3.2 illustrate the results of the first

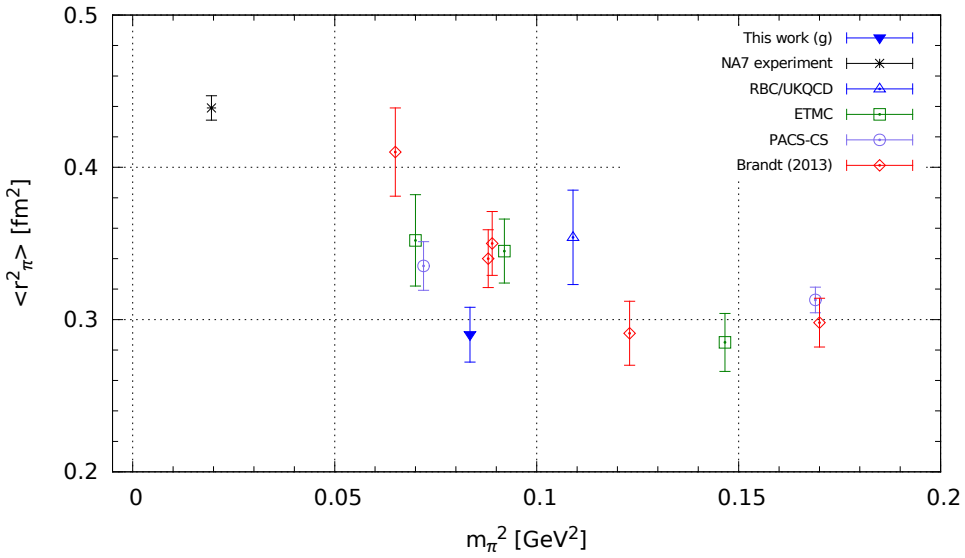

Figure 7.2.5: Compilation of results for the charge radius versus the squared pion mass. Full triangle down is our outcome for ensemble (g). Open symbols stands for foregoing results, diamonds [Bra12], squares [F$^+$09] and triangles down [N$^+$11]. Star represents the phenomenological value from the NA7 experiment [A$^+$86].

method (verifying the sink position at $T/2$ (open circle) and $T/4$ (full triangles up) with zero sink momentum) for vector GFFs. Top and bottom frames show $A^\pi_{2,0}$ and $C^\pi_{2,0}$, respectively. At $Q^2 = 0$ we see a discrepancy which is due to the excited state contamination which was examined in section 6.2.1. By changing the sink position from 32 to 15, far from the gradually descending slopes at smaller momentum transfer, for higher Q^2 we win nothing. Therefore, we can conclude that for the pion, placing the sink at $t_{sink} = T/2$ is the best choice to have minimal excited state contamination.

The right frames compare vector GFFs, $A^\pi_{2,0}$ and $C^\pi_{2,0}$, for sink position $t_{sink} = 15$ with zero (full triangles up) and non-zero sink momentum (open diamond). The comparison indicates that for a sink at $T/4$ we have a more gradual falling slope and again a non-zero sink momentum is the preferred choice. It would be interesting to examine $t_{sink} = T/2$ with non-zero sink momentum in a future study, which was not possible here due to computing time resources. Despite having no data on it, we can conclude that setting sink momentum at zero is not adequate for vector GFFs.

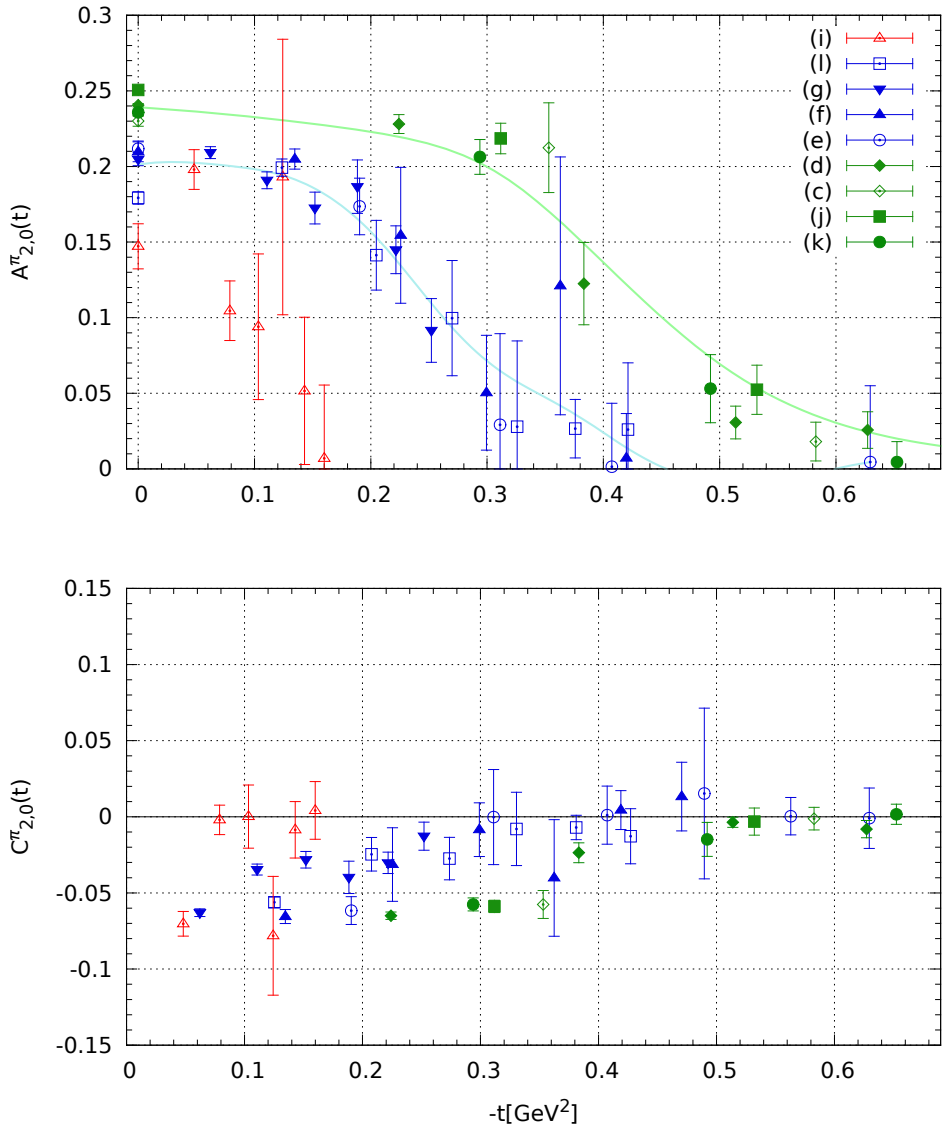

Figure 7.3.1: Connected contributions for the GFFs, top: $A^{\pi}_{2,0}$, bottom: $C^{\pi}_{2,0}$, for simulations listed in Table 6.2.1. Different colors are used to illustrate the pion mass dependence. Open symbols are for simulations with $m_\pi L < 4$ and full ones for $m_\pi L > 4$. The lines in top frame are to guide the eyes and to underpin the pion mass dependence.

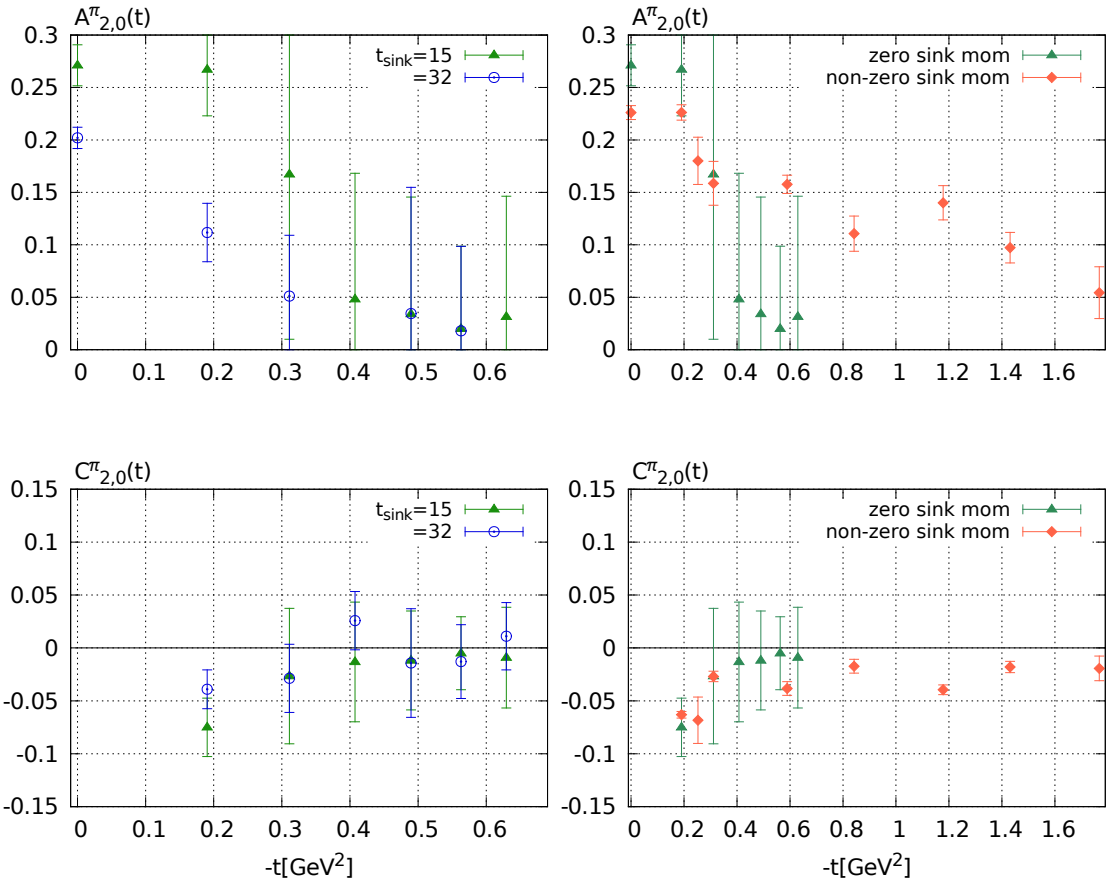

Figure 7.3.2: Left: effect of the sink position $t_{sink} = 15$ (full triangles up) and 32 (open circles) for GFFs ($A^{\pi}_{2,0}$ and $C^{\pi}_{2,0}$, top and bottom frames respectively) when sink momentum is set to zero. Right: GFFs for zero sink momentum (green triangle up) compare with non-zero sink momentum (red diamond) both at $t_{sink} = 15$.

Chapter 8

Summary

The main subject of this project was the calculation of pion parton distribution functions and besides generalized form factors in order to investigate pion structure functions.

In chapter 2 we presented the quantities of our interest, naming the parton distribution functions which provide the probability for finding a parton with a certain longitudinal momentum fraction of the pion and electromagnetic form factors which connect to the charge radius. These quantities are embedded in the framework of generalized parton distributions. Moments of GPDs are parametrized in generalized form factors which are calculable in lattice QCD.

After mentioning the motivations for this work, in chapter 3 we gave a brief introduction to continuum formulations of Quantum Chromodynamics which guided us to four dimensional lattice QCD. The implementation of lattice QCD was briefly explained after that.

The lattice techniques to calculate the matrix elements are summarized in chapter 4. It was shown how to construct and calculate two- and three- point functions on the lattice.

For our calculations we were able to analyze a large set of gauge configurations with several lattice spacings and different values of hopping parameters to cover a large range of pion masses down to 151 MeV.

We organized our numerical results in three separate chapters. In chapter 5 we discussed our results of pion two-point functions from which the pion energy and dispersion relation were extracted. In order to suppress excited state contaminations, we utilized smearing techniques in sink, source and gauge links. The different total momenta to calculate pion two-point functions are up to $(2,1,1) \times 2\pi/L$ in different directions. However, higher momenta have quite large errors and energies must be extracted from dispersion relation. Also we saw the pion mass dependence on the volume.

We presented our method to compute the matrix elements of local operators in chapter 6. The matrix elements for the various local operators can be extracted using a ratio of three- and two-point functions. We checked two different sink positions, $T/4$ and $T/2$, which changes the influence of excited states on the final results. As it was expected, $t_{sink} = T/2$ with sufficient smearing is a good choice to suppress excited state contributions. We reported our data for the connected contributions to the lowest moment of the pion parton distribution functions, $\langle x \rangle^{\pi}$. We saw the existence of a lattice

spacing dependence in $\langle x \rangle^\pi$. Also our data for $\langle x \rangle^\pi$ obtained with improved smearing lies well below the older data from lattice QCD in the quenched approximations, and for simulations with dynamical sea quarks but without smearing. This deviation from old lattice data suggests that with our improved sink-source smearing technique, we have a much better control over excited state contributions. Since our data close to the physical pion mass is smaller than those from phenomenology, it motivates the calculation of disconnected contributions for the pion in a future study. We also saw a non-linear m_π^2-dependence for $\langle x \rangle^\pi$ which raises the question up to what pion masses leading order chiral perturbation theory is applicable.

We would like to point out that the numerical calculations of the row data was tailored to get the precise values for $\langle x \rangle^\pi$. These calculations provide also data for the form factors, though the numerical set up is not optimal for those. We nonetheless used the opportunity to analyze the data for the form factors, in particular as we had access to data almost at the physical point. In chapter 7 we reported our results for the electromagnetic form factor, $f_{\pi\pi}(t)$, and the generalized form factors, $A^\pi_{2,0}(t)$ and $C^\pi_{2,0}(t)$, which parametrize the second lattice moment of the pion GPDs. We saw a clear pion mass dependence for $f_{\pi\pi}(t)$ and also for GFFs. Our data for $f_{\pi\pi}(t)$ is quite noisy in comparison to $\langle x \rangle^\pi$. At lower momentum transfer our outcome is in good agreement with previous results. However, at higher Q^2 our data trends to be zero fast. Also there exists a shift for the ensemble with smallest pion mass. To investigate that feature, we checked two methods for an ensemble with $m_\pi = 295$ MeV and $L/a = 32$. We examined the effect of changing the sink position and saw that for sink position at $T/4$ at smaller Q^2 the descending slope becomes flatter in comparison to $T/2$. For higher Q^2, though a smaller t_{sink} can not solve the problem (see left frame of Fig. 7.2.2). We therefore also checked the sink momentum value for non-zero sink momentum and obtained a much better signal for higher Q^2 (see right frame of Fig. 7.2.2). The same behavior is seen for GFFs and for finite momentum transfer which are affected by the same problem. This suggest to use non-zero sink momentum for any future calculations of pion form factors. Whereas, in chapter 6 it was shown that by placing the sink at $t_{sink} = T/2$ we have a good control over excited states for $\langle x \rangle^\pi$. In order to save computing time we could not examine the sink at $T/2$ with non-zero momentum. As a result, we do not have an accurate answer to explain the behavior of $f_{\pi\pi}(t)$ in the region close to the physical point. Since we used periodic boundary condition, our resolution at small Q^2 is not as optimal as the results with twisted boundary conditions. However, for an ensemble with $m_\pi L = 6.7$ we are in good agreement with forgoing data.

Computer Resources

Generating a large number of $SU(3)$ lattice configurations demands high computational power and advanced computer parallel constructions. In this work, our simulations and calculations have been performed on the SuperMUC system at the Leibniz Computing Center (LRZ) (Munich, Germany), the iDataCool clusters and the Linux cluster computers of the theoretical physics department in Regensburg University. To generate our two- and three-point functions, we have made use of the CHROMA software package [EJ05] adapted for our needs.

"People are always asking for the latest developments in the unification of this theory with that theory, and they don't give us a chance to tell them anything about what we know pretty well. They always want to know the things we don't know."

— Richard Feynman

Appendix A

Notations and conventions

Through the whole thesis we will use units which are commonly done in particle physics and set

$$\hbar = 1, \quad c = 1. \tag{A.0.1}$$

A.1 Parity Transformation

On the lattice QCD, a parity transformation acts on quark and gauge fields as

$$\psi(\vec{x},t) \xrightarrow{\mathcal{P}} \psi(\vec{x},t)^{\mathcal{P}} = \gamma_4\psi(-\vec{x},t), \tag{A.1.1}$$

$$\bar{\psi}(\vec{x},t) \xrightarrow{\mathcal{P}} \bar{\psi}(\vec{x},t)^{\mathcal{P}} = \bar{\psi}(-\vec{x},t)\gamma_4, \tag{A.1.2}$$

$$U_\mu(\vec{x},t) \xrightarrow{\mathcal{P}} U_\mu(\vec{x},t)^{\mathcal{P}} = U_\mu(-\vec{x}-a\hat{\mu},t)^\dagger, \quad \mu = 1,2,3, \tag{A.1.3}$$

$$U_4(\vec{x},t) \xrightarrow{\mathcal{P}} U_4(\vec{x},t)^{\mathcal{P}} = U_4(-\vec{x},t). \tag{A.1.4}$$

A.2 Charge Conjugation

Charge conjugation transforms a particle to an anti-particle. It is defines as

$$\mathcal{C}\gamma_\mu\mathcal{C}^{-1} = -\gamma_\mu^T, \quad \mu \in [1,2,3,4]. \tag{A.2.1}$$

It obeys

$$\psi(x) \xrightarrow{\mathcal{C}} \psi(x)^{\mathcal{C}} = C^{-1}\bar{\psi}(x)^T, \tag{A.2.2}$$

$$\bar{\psi}(x) \xrightarrow{\mathcal{C}} \bar{\psi}(x)^{\mathcal{C}} = -\psi(x)^T C, \tag{A.2.3}$$

$$U_\mu(x) \xrightarrow{\mathcal{C}} U_\mu(x)^{\mathcal{C}} = U_\mu(x)^* = \left(U_\mu(x)^\dagger\right)^T. \tag{A.2.4}$$

$$\tag{A.2.5}$$

A.3 Conventions in Gamma Matrices

In this section we follow the notation of textbooks [PS95, GL10]. Gamma matrices in Euclidean space-time are constructed from the Minkowski gamma matrices

$$\gamma_M^\mu, \quad \mu = 0, 1, 2, 3 \tag{A.3.1}$$
$$\gamma_{E\mu}, \quad \mu = 1, 2, 3, 4. \tag{A.3.2}$$

In Minkowski space, they are converted to Euclidean space-time as

$$\gamma_M^j = i\gamma_j, \quad j = 1, 2, 3 \tag{A.3.3}$$
$$\gamma_M^0 = \gamma_4 \tag{A.3.4}$$

In Minkowski and Euclidean space they obey

$$\{\gamma_M^\mu, \gamma_M^\nu\} = 2g_M^{\mu\nu}\mathbb{1} \qquad \mu, \nu \in [1, 2, 3, 4], \tag{A.3.5}$$
$$\{\gamma_\mu, \gamma_\nu\} = 2\delta_{\mu\nu}\mathbb{1} \qquad \mu, \nu \in [1, 2, 3, 4], \tag{A.3.6}$$

which $\mathbb{1}$ is the unit 4×4 matrix and $g_M^{\mu\nu}$ is the metric tensor for flat Minkowski space and is defined as

$$g_M^{\mu\nu} = \begin{pmatrix} 1 & 0 & 0 & 0 \\ 0 & -1 & 0 & 0 \\ 0 & 0 & -1 & 0 \\ 0 & 0 & 0 & -1 \end{pmatrix} \tag{A.3.7}$$

which in Euclidean space simplifies to the identity matrix, $g_{\mu\nu} = \delta_{\mu\nu}$. Therefore, we do not distinguish between covariant (lower) and contravariant (upper) indices in Euclidean space.

By using the wick rotation, the metric in Euclidean becomes $(-i, +1, +1, +1)$. Also the Euclidean gamma matrices have the following properties

$$\gamma_\mu = \gamma_\mu^\dagger = \gamma_\mu^{-1}, \qquad \mu \in [1, 2, 3, 4, 5] \tag{A.3.8}$$

where γ_5 is the product matrices

$$\gamma_M^5 = i\gamma_M^0\gamma_M^1\gamma_M^2\gamma_M^3 = \gamma_M^{5\dagger} \tag{A.3.9}$$

which anti-commutes with all other gamma matrices. It converts to Euclidean space by changing its sign

$$\gamma^5 = \gamma^1\gamma^2\gamma^3\gamma^4 = -\gamma_M^5. \tag{A.3.10}$$

Appendix B

Conventions for Our Calculations

The coordinates and derivatives are changed from Minkowski space-time to Euclidean space-time as

$$x_M^j = -x_j^M = x_j, \qquad x_M^0 = x_0^M = -ix_4, \tag{B.0.1}$$

$$D_M^j = -D_j^M = -D_j, \qquad D_M^0 = D_0^M = iD_4. \tag{B.0.2}$$

The tensor current in Minkowski space-time is defined as

$$\sigma_M^{\mu\nu} = \frac{i}{2}(\gamma_M^\mu \gamma_M^\nu - \gamma_M^\nu \gamma_M^\mu) = \frac{i}{2}[\gamma_M^\mu, \gamma_M^\nu] \tag{B.0.3}$$

and we use definition in Euclidean space as

$$\sigma^{\mu\nu} = \frac{i}{2}[\gamma_\mu, \gamma_\nu]. \tag{B.0.4}$$

Its conversion to Euclidean space is performed according to its temporal or special direction of indices μ and ν ($\mu \neq \nu$)

$\mu = 0$, $\nu = j$:

$$\sigma_M^{0j} = \frac{i}{2}[\gamma_M^0, \gamma_M^j] = \frac{i}{2}[\gamma_4, i\gamma_j] = i\sigma_{4j} \tag{B.0.5}$$

$\mu = j$, $\nu = k$:

$$\sigma_M^{jk} = \frac{i}{2}\gamma_M^j, \gamma_M^k] = \frac{i}{2}[i\gamma_j, i\gamma_k] = -\sigma_{jk}. \tag{B.0.6}$$

The momentum transfer in Minkowski space $\Delta_M^\mu = p_M'^\mu - p_M^\mu$ is transmuted to Euclidean one like

$\mu = 0$:

$$\Delta_M^0 = p_M'^0 p_M^0 = -i(p_4' - p_4) = -i(E(\vec{p}') - E(\vec{p})) = -i\Delta_4, \tag{B.0.7}$$

$\mu = j$:

$$\Delta_M^j = p_M'^j - p_M^j = \vec{p}'^j - \vec{p}^j = \Delta_j. \tag{B.0.8}$$

In our calculates also we use $\bar{p}^{\mu}_{M} = (p'^{\mu}_{M} + p^{\mu}_{M})/2$ which is transformed as

$$\mu = 0 :$$
$$\bar{p}^{0}_{M} = \frac{p'^{0}_{M} + p^{0}_{M}}{2} = -i\frac{p'_{4} + p_{4}}{2} = -i\bar{p}_{4}, \tag{B.0.9}$$
$$\mu = j :$$
$$\bar{p}^{j}_{M} = \frac{p'^{j}_{M} + p^{j}_{M}}{2} = \frac{p'_{j} + p_{j}}{2} = \bar{p}_{j}. \tag{B.0.10}$$

B.1 Operators

To calculate moments of GPDs on the lattice QCD, we need to apply the tower of twist-two operators. In Minkowski space-time they are defined as

$$\mathcal{O}^{\{\mu_1\cdots\mu_n\}}_{Mq} = i^{n-1}\bar{\psi}^{(f)}\gamma^{\{\mu_1}_{M}\overleftrightarrow{D}^{\mu_2}_{M}\cdots\overleftrightarrow{D}^{\mu_n\}}_{M}\psi^{(f')}, \tag{B.1.1}$$
$$\mathcal{O}^{[\mu_1\{\nu]\cdots\mu_n\}}_{M\sigma q} = i^{n-1}\bar{\psi}^{(f)}i\sigma^{\nu\{\mu_1}_{M}\overleftrightarrow{D}^{\mu_2}_{M}\cdots\overleftrightarrow{D}^{\mu_n\}}_{M}\psi^{(f')} \tag{B.1.2}$$

which $\{\cdots\}$ indicates the symmetrization over indices and $[\cdots]$ anti-symmetrization. With the above definitions they are written in Euclidean space-time as

$$\mathcal{O}^{\{\mu_1\cdots\mu_n\}}_{q} = \bar{\psi}^{(f)}\gamma^{\{\mu_1}\overleftrightarrow{D}^{\mu_2}\cdots\overleftrightarrow{D}^{\mu_n\}}\psi^{(f')}, \tag{B.1.3}$$
$$\mathcal{O}^{[\mu_1\{\nu]\cdots\mu_n\}}_{\sigma q} = \bar{\psi}^{(f)}\sigma^{\nu\{\mu_1}\overleftrightarrow{D}^{\mu_2}\cdots\overleftrightarrow{D}^{\mu_n\}}\psi^{(f')} \tag{B.1.4}$$

To calculate GFFs, considering the above conventions for gamma matrices, operators and momentum transfers to convert space-time from Minkowski to Euclidean, one has to take care of prefactors.

B.2 Pion Electromagnetic Form Factors

Pion elemctromagnetic form factor in Minkowski space-time is written as

$$\langle\pi(\vec{p}')|\bar{q}\gamma^{\mu}_{M}q|\pi(\vec{p})\rangle = 2\bar{p}^{\mu}_{M}f_{\pi\pi}(t) \tag{B.2.1}$$

which corresponding temporal ($\mu = 0$) and special ($\mu = j$) directions in Euclidean space are

$$\mu = 0 :$$
$$\langle\pi(\vec{p}')|\bar{q}\gamma^{0}_{M}q|\pi(\vec{p})\rangle = 2\bar{p}^{0}_{M}f_{\pi\pi}(t)$$
$$\langle\pi(\vec{p}')|\bar{q}\gamma_{4}q|\pi(\vec{p})\rangle = (-i)2\frac{E(\vec{p}) + E(\vec{p}')}{2}f_{\pi\pi}(t) = (-i)2\bar{p}_{4}f_{\pi\pi}(t), \tag{B.2.2}$$
$$\mu = j :$$
$$\langle\pi(\vec{p}')|\bar{q}\gamma^{j}_{M}q|\pi(\vec{p})\rangle = 2\bar{p}^{j}_{M}f_{\pi\pi}(t)$$
$$\langle\pi(\vec{p}')|\bar{q}i\gamma_{j}q|\pi(\vec{p})\rangle = 2\bar{p}_{j}f_{\pi\pi}(t) = 2\frac{\frac{2\pi}{l}p' + \frac{2\pi}{l}p}{2}f_{\pi\pi}(t)$$
$$\langle\pi(\vec{p}')|\bar{q}\gamma_{j}q|\pi(\vec{p})\rangle = (-i)2\frac{\frac{2\pi}{l}p' + \frac{2\pi}{l}p}{2}f_{\pi\pi}(t) = (-i)2\bar{p}_{j}f_{\pi\pi}(t). \tag{B.2.3}$$

B.3 Pion Tensor Form Factors

Tensor form factors in the Minkowski space is defined as

$$\langle\pi(\vec{p}')|\bar{\psi}_q(0)i\sigma_M^{\mu\nu}\psi_q(0)|\pi(\vec{p})\rangle = \frac{\bar{p}_M^{[\mu}\Delta_M^{\nu]}}{m_\pi}\ B_{T\,1,0}^{\pi}(t). \tag{B.3.1}$$

Their definitions in temporal and special directions are as follows

$$\begin{aligned}
&\mu=0,\nu=j:\\
&\qquad\langle\pi(\vec{p}')|\bar{\psi}_q(0)i\sigma_M^{0j}\psi_q(0)|\pi(\vec{p})\rangle = \frac{\bar{p}_M^{[0}\Delta_M^{j]}}{m_\pi}\ B_{T\,1,0}^{\pi}(t)\\
&\qquad\langle\pi(\vec{p}')|\bar{\psi}_q(0)ii\sigma_{4j}\psi_q(0)|\pi(\vec{p})\rangle = -i\frac{\bar{p}^{[4}\Delta^{j]}}{m_\pi}\ B_{T\,1,0}^{\pi}(t)\\
&\qquad\langle\pi(\vec{p}')|\bar{\psi}_q(0)i\sigma_{4j}\psi_q(0)|\pi(\vec{p})\rangle = -\frac{\bar{p}^{[4}\Delta^{j]}}{m_\pi}\ B_{T\,1,0}^{\pi}(t),
\end{aligned} \tag{B.3.2}$$

$$\begin{aligned}
&\mu=j,\nu=k:\\
&\qquad\langle\pi(\vec{p}')|\bar{\psi}_q(0)i\sigma_M^{jk}\psi_q(0)|\pi(\vec{p})\rangle = \frac{\bar{p}_M^{[j}\Delta_M^{k]}}{m_\pi}\ B_{T\,1,0}^{\pi}(t)\\
&\qquad\langle\pi(\vec{p}')|\bar{\psi}_q(0)i(-1)\sigma_{jk}\psi_q(0)|\pi(\vec{p})\rangle = \frac{\bar{p}^{[j}\Delta^{k]}}{m_\pi}\ B_{T\,1,0}^{\pi}(t)\\
&\qquad\langle\pi(\vec{p}')|\bar{\psi}_q(0)i\sigma_{jk}\psi_q(0)|\pi(\vec{p})\rangle = -\frac{\bar{p}^{[j}\Delta^{k]}}{m_\pi}\ B_{T\,1,0}^{\pi}(t).
\end{aligned} \tag{B.3.3}$$

B.4 Moments of GPDs

The first moment of GPDs with vector operator in Minkowski space

$$\mathcal{O}_M^{\mu\nu}(0) = \bar{q}(0)\gamma_M^{\mu}i\overleftrightarrow{D}{}_M^{\nu}q(0) \tag{B.4.1}$$

are defined by

$$\begin{aligned}
&\mu=0,\nu=0:\\
&\qquad\langle\pi(\vec{p})|\bar{q}(0)\gamma_M^0 i\overleftrightarrow{D}{}_M^0 q(0)|\pi(\vec{p}')\rangle &&= 2\bar{p}_M^0\bar{p}_M^0 A_{2,0}^{\pi}(t) + 2\Delta_M^0\Delta_M^0 C_{2,0}^{\pi}(t)\\
&\qquad\langle\pi(\vec{p})|\bar{q}(0)\gamma_4 ii\overleftrightarrow{D}{}_4 q(0)|\pi(\vec{p}')\rangle &&= (-i)(-i)2\bar{p}_4\bar{p}_4 A_{2,0}^{\pi}(t) + (-i)(-i)2\Delta_4\Delta_4 C_{2,0}^{\pi}(t)\\
&\qquad\langle\pi(\vec{p})|\bar{q}(0)\gamma^4 i\overleftrightarrow{D}{}_4 q(0)|\pi(\vec{p}')\rangle &&= i\big(2\bar{p}_4\bar{p}_4 A_{2,0}^{\pi}(t) + 2\Delta_4\Delta_4 C_{2,0}^{\pi}(t)\big),
\end{aligned} \tag{B.4.2}$$

$\mu = 0, \nu = j$:

$$\begin{aligned}
\langle \pi(\vec{p})|\bar{q}(0)\gamma_M^0 i \overleftrightarrow{D}{}_M^j q(0)|\pi(\vec{p}')\rangle &= 2\bar{p}_M^0 \bar{p}_M^j A_{2,0}^\pi(t) + 2\Delta_M^0 \Delta_M^j C_{2,0}^\pi(t) \\
\langle \pi(\vec{p})|\bar{q}(0)\gamma_4 i(-1)\overleftrightarrow{D}{}_j q(0)|\pi(\vec{p}')\rangle &= (-i)2\bar{p}_4 \bar{p}_j A_{2,0}^\pi(t) + (-i)2\Delta_4 \Delta_j C_{2,0}^\pi(t) \\
\langle \pi(\vec{p})|\bar{q}(0)\gamma_4 i \overleftrightarrow{D}{}_j q(0)|\pi(\vec{p}')\rangle &= i\big(2\bar{p}_4 \bar{p}_4 A_{2,0}^\pi(t) + 2\Delta_4 \Delta_4 C_{2,0}^\pi(t)\big), \quad \text{(B.4.3)}
\end{aligned}$$

$\mu = j, \nu = k$:

$$\begin{aligned}
\langle \pi(\vec{p})|\bar{q}(0)\gamma_M^j i \overleftrightarrow{D}{}_M^k q(0)|\pi(\vec{p}')\rangle &= 2\bar{p}_M^j \bar{p}_M^k A_{2,0}^\pi(t) + 2\Delta_M^j \Delta_M^k C_{2,0}^\pi(t) \\
\langle \pi(\vec{p})|\bar{q}(0) i\gamma_j i(-1)\overleftrightarrow{D}{}_k q(0)|\pi(\vec{p}')\rangle &= 2\bar{p}_j \bar{p}_k A_{2,0}^\pi(t) + 2\Delta_j \Delta_k C_{2,0}^\pi(t) \\
\langle \pi(\vec{p})|\bar{q}(0)\gamma_j i \overleftrightarrow{D}{}_k q(0)|\pi(\vec{p}')\rangle &= i\big(2\bar{p}_j \bar{p}_k A_{2,0}^\pi(t) + 2\Delta_j \Delta_k C_{2,0}^\pi(t)\big). \quad \text{(B.4.4)}
\end{aligned}$$

Appendix C

Jackknife Error Estimates

Estimation of the uncertainties is one of the main tasks of data analysis. There are different methods to investigate these errors and Jackknife method is a useful one for large samples. We assume that we want to extract an observable y from N measurement which each measurement is done for different time slices t, like meson correlators

$$\{y_i(0), y_i(1), \ldots, y_i(t)\}, \quad i = 1, \ldots, N. \tag{C.0.1}$$

The jackknife method focuses on subsamples which removing $n-$th measurement to calculate an estimate. It means that we leave out the first value and do the estimation for the rest $N-1$ data sets, it gives us jackknife sample f_1. We then throws out the second value and analysis is done for the rest of $N-1$ sets to get jackknife sample f_2 and so on for all measurements until N-th value

$$\begin{aligned} f_1 &= \frac{1}{N-1} \sum_{\substack{i=1 \\ i\neq 1}}^{N=n} y_i, \\ f_2 &= \frac{1}{N-1} \sum_{\substack{i=1 \\ i\neq 2}}^{N=n} y_i, \\ &\ldots, \\ f_n &= \frac{1}{N-1} \sum_{\substack{i=1 \\ i\neq n}}^{N=n} y_i \end{aligned} \tag{C.0.2}$$

where $f_1 \cdots f_N$ stand for the set of subsample. The uncertainty is then given by

$$\sigma_y^2 = \frac{N-1}{N} \sum_{n=1}^{N} \left(f_n - \bar{y}\right)^2 \tag{C.0.3}$$

where $\bar{y}$ is the average of the complete data sets $\bar{y} = \frac{1}{N}\sum_{i=1}^{N} y_i$. The final result is

$$\langle y \rangle = \bar{y} \pm \sigma_y. \tag{C.0.4}$$

Bibliography

[A+78] H. Ackermann et al. Determination of the Longitudinal and the Transverse Part in pi+ Electroproduction. *Nucl.Phys.*, B137:294, 1978.

[A+86] S. R. Amendolia et al. A measurement of the space - like pion electromagnetic form-factor. *Nucl.Phys.*, B277:168, 1986.

[A+87] M. Albanese et al. Glueball Masses and String Tension in Lattice QCD. *Phys.Lett.*, B192:163–169, 1987.

[A+93] C. R. Allton et al. Gauge invariant smearing and matrix correlators using Wilson fermions at Beta = 6.2. *Phys.Rev.*, D47:5128–5137, 1993.

[A+94] S. Aoki et al. Finite size effects of hadron masses in lattice QCD: A Comparative study for quenched and full QCD simulations. *Phys.Rev.*, D50:486–494, 1994.

[A+01] A. Airapetian et al. Measurement of the beam spin azimuthal asymmetry associated with deeply virtual Compton scattering. *Phys.Rev.Lett.*, 87:182001, 2001.

[A+05] A. Aktas et al. Measurement of deeply virtual compton scattering at HERA. *Eur.Phys.J.*, C44:1–11, 2005.

[A+09] S. Aoki et al. Pion form factors from two-flavor lattice QCD with exact chiral symmetry. *Phys.Rev.*, D80:034508, 2009.

[Aic10] M. Aicher. Final results for pion parton distribution functions. private communication, 2010.

[B+69] M. Breidenbach et al. Observed Behavior of Highly Inelastic electron-Proton Scattering. *Phys.Rev.Lett.*, 23:935–939, 1969.

[B+78] C. J. Bebek et al. Electroproduction of single pions at low epsilon and a measurement of the pion form-factor up to q^2 = 10-gev^2. *Phys.Rev.*, D17:1693, 1978.

[B+79] P. Brauel et al. Electroproduction of $\pi^+ n$, $\pi^- p$ and $K^+\Lambda$, $K^+\Sigma^0$ Final States Above the Resonance Region. *Z.Phys.*, C3:101, 1979.

[B+83] J. Badier et al. Experimental determination of the pi meson structure functions by the drell-yan mechanism. *Z.Phys.*, C18:281, 1983.

[B+86] B. Bunk et al. *Lattice Gauge Theory: A Challenge in Large-Scale Computing (NATO Science Series B: Physics*. Plenum Press, 1986.

[B+87] P. Bordalo et al. Observation of a Nuclear Dependence of the Transverse Momentum Distribution of Massive Muon Pairs Produced in Hadronic Collisions. *Phys.Lett.*, B193:373, 1987.

[B+96] T. Bhattacharya et al. Hadron spectrum with Wilson fermions. *Phys.Rev.*, D53:6486–6508, 1996.

[B+97] C. Best et al. Pion and rho structure functions from lattice qcd. *Phys.Rev.*, D56:2743–2754, 1997.

[B+05] F. D. R. Bonnet et al. Lattice computations of the pion form-factor. *Phys.Rev.*, D72:054506, 2005.

[B+07a] R. Baron et al. Moments of meson distribution functions with dynamical twisted mass fermions. *PoS*, LAT2007:153, 2007.

[B+07b] P. A. Boyle et al. Hadronic form factors in lattice qcd at small and vanishing momentum transfer. *JHEP*, 0705:016, 2007.

[B+07c] D. Brömmel et al. The Pion form-factor from lattice QCD with two dynamical flavours. *Eur.Phys.J.*, C51:335–345, 2007.

[B+08] P. A. Boyle et al. The Pion's electromagnetic form-factor at small momentum transfer in full lattice QCD. *JHEP*, 0807:112, 2008.

[B+12] J. Beringer et al. Review of Particle Physics (RPP). *Phys.Rev.*, D86:010001, 2012.

[B+13] G. S. Bali et al. Nucleon mass and sigma term from lattice QCD with two light fermion flavors. *Nucl.Phys.*, B866:1–25, 2013.

[B+14a] G. S. Bali et al. Moments of structure functions for $N_f = 2$ near the physical point. *PoS*, LATTICE2013:290, 2014.

[B+14b] V. M. Braun et al. Light-cone Distribution Amplitudes of the Nucleon and Negative Parity Nucleon Resonances from Lattice QCD. 2014.

[Bas07] S. D. Bass. The Spin structure of the proton. 2007.

[BP69] J. D. Bjorken and E. A. Paschos. Inelastic electron-proton and gamma-proton scattering and the structure of the nucleon. *Phys. Rev.*, 185:1975–1982, Sep 1969.

[BP07] S. Boffi and B. Pasquini. Generalized parton distributions and the structure of the nucleon. *Riv.Nuovo Cim.*, 30:387, 2007.

[BR05] A. V. Belitsky and A.V. Radyushkin. Unraveling hadron structure with generalized parton distributions. *Phys.Rept.*, 418:1–387, 2005.

[Bra12] B. B. Brandt. *Chiral properties of two-flavour QCD at zero and non-zero temperature*. PhD thesis, Johannes Gutenberg-Universität, 2012.

[Brö07] D. Brömmel. Pion structure from the lattice. 2007.

[Bru52] K. A. Brueckner. Meson-Nucleon Scattering and Nucleon Isobars. *Phys.Rev.*, 86:106–109, 1952.

[C+72] N. H. Christ et al. Light cone behavior of perturbation theory. *Phys.Rev.*, D6:3543, 1972.

[C+79] M. Creutz et al. Monte Carlo Study of Abelian Lattice Gauge Theories. *Phys.Rev.*, D20:1915, 1979.

[C+89] J. S. Conway et al. Experimental Study of Muon Pairs Produced by 252-GeV Pions on Tungsten. *Phys.Rev.*, D39:92–122, 1989.

[C+03] S. Chekanov et al. Measurement of deeply virtual Compton scattering at HERA. *Phys.Lett.*, B573:46–62, 2003.

[C+06a] S. Capitani et al. A Lattice calculation of the pion form-factor with Ginsparg-Wilson-type fermions. *Phys.Rev.*, D73:034505, 2006.

[C+06b] S. Capitani et al. Parton distribution functions with twisted mass fermions. *Physics Letters B*, 639:520–526, 2006.

[CG69] Jr. Callan, C. G. and D. J. Gross. High-energy electroproduction and the constitution of the electric current. *Phys.Rev.Lett.*, 22:156–159, 1969.

[Col97] J. C. Collins. Light cone variables, rapidity and all that. 1997.

[Cos] Guido Cossu. Getting to the heart of matter. http://www.jicfus.jp/en/promotion/pr/mj/guido-cossu/.

[Cou10] Aurore Courtoy. Generalized Parton Distributions of Pions. Spin Structure of Hadrons. 2010.

[D+67] T. Das et al. Electromagnetic mass difference of pions. *Phys.Rev.Lett.*, 18:759–761, 1967.

[D+89] T. Draper et al. The Pion Form-factor in Lattice QCD. *Nucl.Phys.*, B318:319, 1989.

[D+03] W. Detmold et al. Parton distribution functions in the pion from lattice QCD. *Phys.Rev.*, D68:034025, 2003.

[Die03] M. Diehl. Generalized parton distributions. *Phys.Rept.*, 388:41–277, 2003.

[Dur07] S. Durr. The art of smearing: Can one reach M(pi) = 140-MeV in quenched QCD with clover quarks? *PoS*, LAT2007:072, 2007.

[E+04] S. Eidelman et al. Review of particle physics. Particle Data Group. *Phys.Lett.*, B592:1–1109, 2004.

[EJ05] Robert G. Edwards and Balint Joó. The Chroma software system for lattice QCD. *Nucl.Phys.Proc.Suppl.*, 140:832, 2005.

[F+09] R. Frezzotti et al. Electromagnetic form factor of the pion from twisted-mass lattice QCD at N(f) = 2. *Phys.Rev.*, D79:074506, 2009.

[F+12] A. Frommer et al. Deflation and Flexible SAP-Preconditioning of GMRES in Lattice QCD Simulation. 2012.

[Fey85] R. P. Feynman. *QED: The Strange Theory of Light and Matter*. Princeton University Press, 1985.

[Fey88] R. P. Feynman. *Special Relativity and Quantum Theory*. Springer Netherlands, 1988.

[Fle88] R. Fletcher. *Conjugate gradient methods for indefinite systems*. Springer Berlin / Heidelberg, 1988.

[Fra02] P. Franzini. Elementary Particle Physics Lecture notes. http://www.lnf.infn.it/~paolo/, 2002.

[G+96a] M. Göckeler et al. Lattice operators for moments of the structure functions and their transformation under the hypercubic group. *Phys.Rev.*, D54:5705–5714, 1996.

[G+96b] M. Göckeler et al. Perturbative renormalization of lattice bilinear quark operators. *Nucl.Phys.*, B472:309–333, 1996.

[G+99a] B. Geyer et al. Decomposition of nonlocal light cone operators into harmonic operators of definite twist. *Nucl.Phys.*, B559:339–377, 1999.

[G+99b] M. Göckeler et al. Nonperturbative renormalization of composite operators in lattice QCD. *Nucl.Phys.*, B544:699–733, 1999.

[G+05] M. Guagnelli et al. Non-perturbative pion matrix element of a twist-2 operator from the lattice. *Eur. Phys. J.*, C40:69–80, 2005.

[G+10] M. Göckeler et al. Perturbative and nonperturbative renormalization in lattice qcd. *Phys.Rev.*, D82:114511, 2010.

[G+13] M. Guidal et al. Generalized Parton Distributions in the valence region from Deeply Virtual Compton Scattering. *Rept.Prog.Phys.*, 76:066202, 2013.

[Geo99] H. Georgi. Lie algebras in particle physics. 1999.

[GL10] C. Gattringer and C. B. Lang. *Quantum Chromodynamics on the Lattice: An introductory presentation*. Springer, Berlin Heidelberg, 2010.

[GM64] Murray Gell-Mann. A Schematic Model of Baryons and Mesons. *Phys.Lett.*, 8:214–215, 1964.

[GMS06] D. Guadagnoli, F. Mescia, and S. Simula. Lattice study of semileptonic form-factors with twisted boundary conditions. *Phys.Rev.*, D73:114504, 2006.

[Göc13] M. Göckeler. Renormalization factors for lattice operators. private communication, 2013.

[Gre64] O. W. Greenberg. Spin and Unitary Spin Independence in a Paraquark Model of Baryons and Mesons. *Phys.Rev.Lett.*, 13:598–602, 1964.

[Gri08] D. Griffiths. Introduction to elementary particles. 2008.

[GT71] D. J. Gross and S. B. Treiman. Light cone structure of current commutators in the gluon quark model. *Phys.Rev.*, D4:1059–1072, 1971.

[Gup97] R. Gupta. Introduction to lattice QCD: Course. pages 83–219, 1997.

[Gus90] S. Gusken. A Study of smearing techniques for hadron correlation functions. *Nucl.Phys.Proc.Suppl.*, 17:361–364, 1990.

[Gut12] S. Gutzwiller. Scattering phase shift for elastic two pion scattering and the rho resonance in lattice qcd, Oktober 2012.

[GW73a] D. J. Gross and F. Wilczek. Asymptotically Free Gauge Theories. 1. *Phys.Rev.*, D8:3633–3652, 1973.

[GW73b] D. J. Gross and F. Wilczek. Ultraviolet Behavior of Nonabelian Gauge Theories. *Phys.Rev.Lett.*, 30:1343–1346, 1973.

[H+01] M. B. Hecht et al. Valence quark distributions in the pion. *Phys.Rev.*, C63:025213, 2001.

[H+06] T. Horn et al. Determination of the charged pion form factor at q**2 = 1.60 and 2.45-(gev/c)**2. *Phys.Rev.Lett.*, 97:192001, 2006.

[H+07] J. N. Hedditch et al. Pseudoscalar and vector meson form-factors from lattice qcd. *Phys.Rev.*, D75:094504, 2007.

[H+08a] T. Horn et al. Scaling study of the pion electroproduction cross sections and the pion form factor. *Phys.Rev.*, C78:058201, 2008.

[H+08b] G. M. Huber et al. Charged pion form-factor between q**2 = 0.60-gev**2 and 2.45-gev**2. ii. determination of, and results for, the pion form-factor. *Phys.Rev.*, C78:045203, 2008.

[Hag10] Ph. Hagler. Hadron structure from lattice quantum chromodynamics. *Phys.Rept.*, 490:49–175, 2010.

[Het12] M. Hetzenegger. A lattice qcd determination of potentials between pairs of static-light mesons, September 2012.

[HH85] A. Hasenfratz and P. Hasenfratz. LATTICE GAUGE THEORIES. *Ann.Rev.Nucl.Part.Sci.*, 35:559–604, 1985.

[HK01] A. Hasenfratz and F. Knechtli. Flavor symmetry and the static potential with hypercubic blocking. *Phys.Rev.*, D64:034504, 2001.

[HM84] F. Halzen and A. D. Martin. *Quarks and Leptons: An Introductory Course in Modern Particle Physics*. Wiley, New York, USA, 1984.

[Hof56] R. Hofstadter. Electron scattering and nuclear structure. *Rev.Mod.Phys.*, 28:214–254, 1956.

[Hor00] R. Horsley. The hadronic structure of matter-a lattice approach. *Habilitations-schrift*, 2000.

[Jaf75] R. L. Jaffe. Deep Inelastic Structure Functions in an Approximation to the Bag Theory. *Phys.Rev.*, D11:1953, 1975.

[Ji97] Xiang-Dong Ji. Deeply virtual Compton scattering. *Phys.Rev.*, D55:7114–7125, 1997.

[Ji98] X. D. Ji. Off forward parton distributions. *J.Phys.*, G24:1181–1205, 1998.

[JO98] X. D. Ji and J. Osborne. One loop corrections and all order factorization in deeply virtual Compton scattering. *Phys.Rev.*, D58:094018, 1998.

[KS81] L. H. Karsten and Jan Smit. Lattice Fermions: Species Doubling, Chiral Invariance, and the Triangle Anomaly. *Nucl.Phys.*, B183:103, 1981.

[KSF01] H. Kleinert and V. Schulte-Frohlinde. Critical properties of phi**4-theories. 2001.

[L$^+$92] M. Luscher et al. The Schrodinger functional: A Renormalizable probe for nonAbelian gauge theories. *Nucl.Phys.*, B384:168–228, 1992.

[L$^+$11] L. Lellouch et al. Modern perspectives in lattice qcd: Quantum field theory and high performance computing. proceedings, international school, 93rd session, les houches, france, august 3-28, 2009. 2011.

[Lau14] T. Lautenschlager. Towards a global estimate for generalized parton distributions, Juni 2014.

[Leh54] H. Lehmann. On the Properties of propagation functions and renormalization contants of quantized fields. *Nuovo Cim.*, 11:342–357, 1954.

[LM93] G. P. Lepage and P. B. Mackenzie. On the viability of lattice perturbation theory. *Phys.Rev.*, D48:2250–2264, 1993.

[LS11] M. Luscher and S. Schaefer. Lattice QCD without topology barriers. *JHEP*, 1107:036, 2011.

[Lus07] M. Luscher. Local coherence and deflation of the low quark modes in lattice QCD. *JHEP*, 0707:081, 2007.

[Lus10] M. Luscher. Computational Strategies in Lattice QCD. pages 331–399, 2010.

[M+95] G. Martinelli et al. A General method for nonperturbative renormalization of lattice operators. *Nucl.Phys.*, B445:81–108, 1995.

[Man92] A. V. Manohar. An Introduction to spin dependent deep inelastic scattering. 1992.

[MB47] R. E. Marshak and H. A. Bethe. On the two-meson hypothesis. *Phys. Rev.*, 72:506–509, Sep 1947.

[MP04] C. Morningstar and M. J. Peardon. Analytic smearing of SU(3) link variables in lattice QCD. *Phys.Rev.*, D69:054501, 2004.

[MS87] G. Martinelli and C. T. Sachrajda. PION STRUCTURE FUNCTIONS FROM LATTICE QCD. *Phys.Lett.*, B196:184, 1987.

[MV00] S. Moch and J. A. M. Vermaseren. Deep inelastic structure functions: Reconstruction from Mellin moments. *Nucl.Phys.Proc.Suppl.*, 89:137–142, 2000.

[N+11] O. H. Nguyen et al. Electromagnetic form factor of pion from $N_f = 2 + 1$ dynamical flavor QCD. *JHEP*, 1104:122, 2011.

[Nam12] Seung-il Nam. Parton-distribution functions for the pion and kaon in the gauge-invariant nonlocal chiral-quark model. *Phys.Rev.*, D86:074005, 2012.

[NN81] H. B. Nielsen and M. Ninomiya. A no-go theorem for regularizing chiral fermions. *Phys. Lett.*, B105:219, 1981.

[O+14] K. A. Olive et al. Review of Particle Physics. *Chin.Phys.*, C38:090001, 2014.

[Per82] D. H. Perkins. Introduction to high energy physics. 1982.

[Pic95] A. Pich. Quantum chromodynamics. 1995.

[pn55] Les prix nobel. The nobel foundation, stokholm. http://www.nobelprize.org/nobel_prizes/physics/laureates/1955/lamb-lecture.pdf, 1955.

[Pol73] H. D. Politzer. Reliable perturbative results for strong interactions? *Phys. Rev. Lett.*, 30:1346–1349, Jun 1973.

[PS95] M. E. Peskin and D. V. Schroeder. An introduction to quantum field theory. 1995.

[Rad96] A. V. Radyushkin. Scaling limit of deeply virtual Compton scattering. *Phys.Lett.*, B380:417–425, 1996.

[Rad97] A. V. Radyushkin. Nonforward parton distributions. *Phys.Rev.*, D56:5524–5557, 1997.

[Ros81] J. L. Rosner. New Particles. Selected Reprints. 1981.

[Rut11] E. Rutherford. The scattering of alpha and beta particles by matter and the structure of the atom. *Phil.Mag.*, 21:669–688, 1911.

[S+92] P. J. Sutton et al. Parton distributions for the pion extracted from Drell-Yan and prompt photon experiments. *Phys.Rev.*, D45:2349–2359, 1992.

[S+01] S. Stepanyan et al. Observation of exclusive deeply virtual Compton scattering in polarized electron beam asymmetry measurements. *Phys.Rev.Lett.*, 87:182002, 2001.

[Saa] *Iterative Methods for Sparse Linear Systems*. SIAM.

[Sch98] A. Schiller. Introductory lectures on the structure of the hadrons from the lattice. page 90, 1998.

[Sin94] S. Sint. On the Schrödinger functional in QCD. *Nucl.Phys.*, B421:135–158, 1994.

[Som94] R. Sommer. A New way to set the energy scale in lattice gauge theories and its applications to the static force and alpha-s in SU(2) Yang-Mills theory. *Nucl.Phys.*, B411:839–854, 1994.

[SV05] C. T. Sachrajda and G. Villadoro. Twisted boundary conditions in lattice simulations. *Phys.Lett.*, B609:73–85, 2005.

[SW85] B. Sheikholeslami and R. Wohlert. Improved continuum limit lattice action for qcd with wilson fermions. *Nucl.Phys.*, B259:572, 1985.

[Sym83] K. Symanzik. Continuum limit and improved action in lattice theories. 1. principles and phi**4 theory. *Nucl.Phys.*, B226:187, 1983.

[T+07] V. Tadevosyan et al. Determination of the pion charge form-factor for Q**2 = 0.60-GeV**2 - 1.60-GeV**2. *Phys.Rev.*, C75:055205, 2007.

[TC06] DeGrand T. and DeTar C. *Lattice Methods for Quantum Chromodynamics*. World Scientific, 2006.

[V+01] J. Volmer et al. Measurement of the Charged Pion Electromagnetic Form-Factor. *Phys.Rev.Lett.*, 86:1713–1716, 2001.

[vdH+03] J. van der Heide et al. The Pion form-factor in improved lattice QCD. *Phys.Lett.*, B566:131–136, 2003.

[vdV92] H. A. van der Vorst. Bi-cgstab: A fast and smoothly converging variant of bi-cg for the solution of nonsymmetric linear systems. *SIAM J. Sci. and Stat. Comput., 13(2)*, page 631–64, 1992.

[W+92] W. Wilcox et al. Chiral limit of nucleon lattice electromagnetic form-factors. *Phys.Rev.*, D46:1109–1122, 1992.

[W+04] I. Wetzorke et al. Pion parton distribution functions from lattice QCD. *Nucl.Phys.Proc.Suppl.*, 129:281–283, 2004.

[Wei00] S. Weinzierl. Introduction to Monte Carlo methods. 2000.

[Wil74] K. G. Wilson. Confinement of quarks. *Phys. Rev. D*, 10:2445–2459, Oct 1974.

[Wil75] K. G. Wilson. Quarks and strings on a lattice. 1975.

[Wo05] K. Wijesooriya and others. The pion parton distribution function in the valence region. *Phys.Rev.*, C72:065203, 2005.

[WZ72] K. G. Wilson and W. Zimmermann. Operator product expansions and composite field operators in the general framework of quantum field theory. *Commun.Math.Phys.*, 24:87–106, 1972.

[Zwe64] G. Zweig. An SU(3) model for strong interaction symmetry and its breaking. pages 22–101, 1964.

Acknowledgements

There are many people whom I should acknowledge for all hardship they endured in helping me during my research period to make this thesis possible.

First of all, I owe my gratitude to my parents who always have stood by me and pulled me through in tough tasks. It is hard to thank them enough for their love, care and unconditional support through all these years. I think they already know what they mean to me and how appreciated I am for their ongoing encouragements as I work towards my academic dreams.

It is difficult for me to sum up an acknowledge of my official advisor, Prof. Dr. Gunnar Bali in giving me the opportunity to work on this thesis. He was patient, helpful and supportive in many different ways. Although I oftentimes felt timid to talk with him, it was an honor and a great pleasure for me to work with and learn from him.

I would like to extend my great appreciation to my direct advisor, Dr. Andre Sternbeck. Despite his extremely busy schedule, he would always make himself available for help and advice. Without his ideas, computational expertise and motivations, this work would still, to this day, be far from finished. I am also greatly indebted to the use of his invaluable time for proofreading the manuscript.

In particular, I would like to thank PD Dr. Meinulf Göckeler who answered my questions patiently and Dr. Sara Collins for helping me to understand CHROMA software. I thank Dr. Johannes Najjar and Benjamin Gläßle who allowed me to use their code named Woiperdinger which helped me to recheck my results and saved a lot of work and also Dr. Paula Pérez Rubio to help me for MATLAB code. A particular thanks goes to Monika Maschek and Heidi Decock for assistance in arranging a number of things and providing helpful information over the years. Also I greatly appreciate Dr. Stefan Solbrig's friendship and technical help.

I am totally grateful to my sister and her family, especially my niece. Although the Regensburg sky was gray, every smile from her via Skype brought a little extra sunshine into my day. I should emphasize my special thank to Dr. Simone Gutzwiller who was my officemate. I appreciate her for all funny times that we shared, for all my moody moments that she endured and all motivation that she gave me to keep continuing. I am also grateful to her for proofreading my manuscript and helping in computer dilemmas. I would also like to thank my friends' support from all over the world, in particular Dr. Mehdi Abedi, Dr. Alireza Keykhosravi and Maryam Bagheri for their company, especially during those difficult first days of moving to Regensburg.

Last but not least, my appreciation is to Alireza for his support during these years. Thank you for every thing you have done to help along this traveling the ups and downs of life, which put us in the border of insanity.

This work was supported in parts by the European Reintegration Grant (FP7-PEOPLE-2009-RG, No.256594), the EU under grant 238353 (ITN STRONGnet) and the DFG (SFB/TR55, Hadron Physics from Lattice QCD).